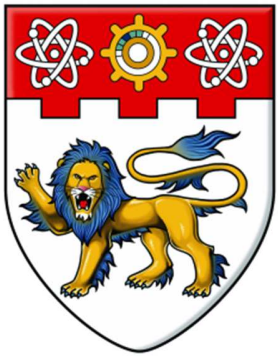

NANYANG TECHNOLOGICAL UNIVERSITY

METAL SULFIDES AND THEIR LITHIUM STORAGE PROPERTIES

LIU WEILING

SCHOOL OF MATERIALS SCIENCE AND ENGINEERING

2017

METAL SULFIDES AND THEIR LITHIUM STORAGE PROPERTIES

LIU WEILING

SCHOOL OF MATERIALS SCIENCE AND ENGINEERING

A thesis submitted to the Nanyang Technological University in partial fulfilment of the requirement for the degree of Doctor of Philosophy

2017

Statement of Originality

I hereby certify that the work embodied in this thesis is the result of original research and has not been submitted for a higher degree to any other University or Institution.

11 Aug 2016

. . . . . .

Date

. . . . . .

Liu Weiling

Abstract

Lithium ion battery (LIB) is currently one of the most widely used forms of rechargeable energy storage system in portable electronics. To achieve LIB with enhanced lithium storage properties, better safety aspects and lower cost, extensive research has been conducted on the various components of a LIB for the past few decades. Although graphite is currently used as the anode material in most commercial LIB, its limited capacity and the safety issues related to its low electrochemical potential (*vs.* Li/Li^+) have prompted scientists to search for alternative materials. Amongst the various conversion-typed materials, metal sulfides are particularly interesting as sulfur (S) has a rich and versatile chemistry, thus providing the possibility of altering the lithium storage properties of the materials by simply varying the stoichiometric ratio between the metal and sulfide ion in the compound. However, as with all sulfur and sulfide electrodes, polysulfides will be formed during their partial reduction, resulting in poor capacity retention and cycling performance in lithium and lithium ion batteries. In view of this, more study needs to be carried out to find approaches that can be undertaken to improve the lithium storage performance of metal sulfide electrodes. Hence, this thesis aims to gain an insight into how the amount of sulfide ion in the stoichiometry of a metal sulfide compound affects its lithium storage properties, with the focus placed on two metal sulfide systems, namely, iron sulfides (intercalation-conversion material) and tin sulfides (conversion-alloying material).

To investigate the effect of how the amount of sulfide ion in the stoichiometry of an iron sulfide compound affects its lithium storage properties, pyrrhotite $Fe_{1-x}S$ and pyrite FeS_2 with good purity have been successfully synthesized via a solution-based chemical synthesis method and their electrochemical properties were characterized. It was found that pyrite FeS_2 exhibits better lithium storage capability than pyrrhotite $Fe_{1-x}S$ because of: (1) the lower polarization, better electron and Li^+ ion transport at the interface between the active material and electrolyte at the pyrite FeS_2 electrode and (2) the reversible lithiation and delithiation of iron sulfide (FeS_y) during the galvanostatic cycling of the pyrite FeS_2 electrode.

SnS and SnS_2 with good purity have also been successfully prepared via a solution-based chemical synthesis method to investigate the effect of how the amount of sulfide ion in the stoichiometry of a tin sulfide compound affects its lithium storage properties and the electrochemical properties of these compounds were characterized. It was found that SnS_2 displayed a higher capacity and better cycling stability than SnS after prolonged cycling particularly at higher current densities. Since the SnS_2 electrode was found to have a poorer electronic and ionic conductivity than the SnS electrode, its superior lithium storage performance is attributed to its chemical and structural properties. As evidenced by the higher discharge capacity attained from the intercalation and conversion reaction throughout the 100 cycles, more Li_2S is formed during the lithiation of SnS_2, thus providing a thicker layer to buffer the large volume change during the lithiation and delithiation of Sn. This can result in a reduction in the pulverization and better capacity retention of the electrode after prolonged cycling, as verified by the slower alloying capacity fading rate observed in the SnS_2 electrode compared to the SnS electrode.

It is found in this dissertation that for both iron and tin sulfides, the compound with a higher sulfide ion content in its stoichiometry i.e. FeS_2 and SnS_2 exhibits better lithium storage performance than its counterpart with lower sulfide ion content i.e. $Fe_{1-x}S$ and SnS when cycled in a voltage window of 0.001 – 3 V. For the pyrite FeS_2 electrode, which undergoes intercalation and conversion reaction during cycling, the superior lithium storage performance is attributed to its better conductivity and reversibility of the lithiation and delithiation of FeS_y. On the other hand, the SnS_2 electrode, which undergoes conversion and alloying reaction during cycling, displayed a better lithium storage performance due to its ability to form a thicker Li_2S layer which provides better buffering for the large volume change in the Sn particles during their alloying reaction, thus maintaining structural integrity of the electrode and result in slower capacity fading.

Acknowledgements

The author would like to express her sincerest gratitude to her PhD supervisor, Associate Professor Hng Huey Hoon for her patient guidance for the past years. Thank you for always being there to provide valuable advices, help and inspiration, prompting me to think deeper but never ever limiting me from trying out new ideas.

Research would have been a lonely journey without all my endearing labmates like Dr Tan Hui Teng, Dr Xu Chen, Dr Rui Xianhong and many more, in particular, "The Three Musketeers" – Dr Tan Li Ping and Dr Fan Shufen. The completion of this thesis would not be possible without your constant assistance and encouragement. You are all deeply loved and appreciated!

To all the technical staffs in MSE especially Patrick, Wilson, Yee Yan, Dr Zvaid, Poh Tin and Swee Kuan, thank you for all the help and assistance rendered to me in one way or another throughout the pursue of my PhD.

A big thank you also goes to the little "farm" in IMRE which includes Dr Lim Siew Lay, Ms Ivy Wong, Mr Goh Wei Peng, Dr Tan Mein Jin, Dr Ho Jian Wei and Dr Kam Zhiming for their support, be it technically, physically or emotionally. A balance needs to be strike between work and life. Thank you to my dearest friends – Hami, ZL, Xiuhui, Amanda and Poon for taking good care of my social life, listening to all my ranting when things are not going smoothly for me and for sharing my joy when I have things to be happy about.

Last, but definitely not the least, the author would also like to express her deepest gratitude to her family. I know that some of the decisions that I had made can be quite wilful, but all these were done with the faith that you will always be there for me to fall back on if anything goes wrong. Thank you, Mummy, Daddy, my "stupid" Bro, Grandma and my beloved late Grandaunt for all the love and support! I am who I am because I have you around me.

Carpe Diem – Seize the day, live your day to the fullest and make your life extraordinary!

Table of Contents

Table Captions

Figure Captions

List of Publications

Publications

Yu, H.; Fan, H.; Yadian, B.; Tan, H.; **Liu, W.**; Hng, H. H.; Huang, Y.; Yan, Q. General Approach for MOF-Derived Porous Spinel AFe_2O_4 Hollow Structures and Their Superior Lithium Storage Properties. ACS Applied Materials & Interfaces **2015**, 7, 26751-26757.

Liu, W. L.; Rui, X. H.; Tan, H. T.; Xu, C.; Yan, Q. Y.; Hng, H. H. Solvothermal synthesis of pyrite FeS_2 nanocubes and their superior high rate lithium storage properties. *RSC Advances* **2014**, *4*, 48770-48776.

Tan, H. T.; Rui, X.; Lu, Z.; Xu, C.; **Liu, W.**; Hng, H. H.; Yan, Q. Integrated Charge Transfer in Colloidal Cu-MnO Heterostructures for High-Performance Lithium Ion Batteries. *Journal of Physical Chemistry C* **2014**, *118*, 17452-17460.

Tan, H. T.; Rui, X.; Yu, H.; **Liu, W.**; Xu, C.; Xu, Z.; Hng, H. H.; Yan, Q. Aqueous-Based Chemical Route toward Ambient Preparation of Multicomponent Core–Shell Nanotubes. *ACS Nano* **2014**, *8*, 4004-4014.

Zhang, W.; Zhu, J.; Ang, H.; Zeng, Y.; Xiao, N.; Gao, Y.; **Liu, W.**; Hng, H. H.; Yan, Q. Binder-free graphene foams for O-2 electrodes of Li-O-2 batteries. *Nanoscale* **2013**, *5*, 9651-9658.

Yu, H.; Rui, X.; Tan, H.; Chen, J.; Huang, X.; Xu, C.; **Liu, W.**; Yu, D. Y. W.; Hng, H. H.; Hoster, H. E.; Yan, Q. Cu doped V_2O_5 flowers as cathode material for high-performance lithium ion batteries. *Nanoscale* **2013**, *5*, 4937-4943.

Rui, X.; Tan, H.; Sim, D.; **Liu, W.**; Xu, C.; Hng, H. H.; Yazami, R.; Lim, T. M.; Yan, Q. Template-free synthesis of urchin-like Co_3O_4 hollow spheres with good lithium storage properties. *Journal of Power Sources* **2013**, *222*, 97-102.

Zhang, W.; Zeng, Y.; Xu, C.; Tan, H.; **Liu, W.**; Zhu, J.; Xiao, N.; Hng, H. H.; Ma, J.; Hoster, H. E.; Yazami, R.; Yan, Q. Fe_2O_3 nanocluster-decorated graphene as O-2 electrode for high energy Li-O-2 batteries. *Rsc Advances* **2012**, *2*, 8508-8514.

Xu, C.; Zeng, Y.; Rui, X.; Xiao, N.; Zhu, J.; Zhang, W.; Chen, J.; **Liu, W.**; Tan, H.; Hng, H. H.; Yan, Q. Controlled Soft-Template Synthesis of Ultrathin C@FeS Nanosheets with High-Li-Storage Performance. *Acs Nano* **2012**, *6*, 4713-4721.

Rui, X.; Sim, D.; Wong, K.; Zhu, J.; **Liu, W.**; Xu, C.; Tan, H.; Xiao, N.; Hng, H. H.; Lim, T. M.; Yan, Q. $Li_3V_2(PO_4)_3$ nanocrystals embedded in a nanoporous carbon matrix supported on reduced graphene oxide sheets: Binder-free and high rate cathode material for lithium-ion batteries. *Journal of Power Sources* **2012**, *214*, 171-177.

Rui, X.; Sim, D.; Xu, C.; **Liu, W.**; Tan, H.; Wong, K.; Hng, H. H.; Lim, T. M.; Yan, Q. One-pot synthesis of carbon-coated VO_2(B) nanobelts for high-rate lithium storage. *Rsc Advances* **2012**, *2*, 1174-1180.

Rui, X.; Zhu, J.; **Liu, W.**; Tan, H.; Sim, D.; Xu, C.; Zhang, H.; Ma, J.; Hng, H. H.; Lim, T. M.; Yan, Q. Facile preparation of hydrated vanadium pentoxide nanobelts based bulky paper as flexible binder-free cathodes for high-performance lithium ion batteries. *Rsc Advances* **2011**, *1*, 117-122.

Oral Presentation

Liu, W.; Rui, X.; Tan, H. T.; Xu, C.; Yan, Q.; Hng, H. H. Investigation On Lithium Storage Properties of Solvothermal-Synthesized Pyrite FeS_2 Nanocubes. 224th ECS Meeting **2013** , San Francisco, United States

Chapter 1

Introduction

This chapter provides a short background to the topic of lithium ion battery (LIB), highlighting the problems faced in this area of research. Based on the stated challenges, it was found that there is a need to explore possible methods of improving the lithium storage properties of metal sulfide electrodes so as to enhance the performance of LIB. Hence, this dissertation aims to understand the effect of the number of sulfide ions in a metal sulfide compound on its lithium storage performance and why the metal sulfide compound with one stoichiometry performs better than the same metal sulfide compound with another stoichiometry. In this thesis, it was found that for both iron sulfides (intercalation-conversion anodic material) and tin sulfides (conversion-alloying anodic material), the compound with a higher sulfide ion content in its stoichiometry i.e. FeS_2 and SnS_2 exhibits better lithium storage performance than its counterpart with lower sulfide ion content i.e. $Fe_{1-x}S$ and SnS when cycled in a voltage window of 0.001 – 3 V. Through this understanding, possible ways of improving the lithium storage properties of metal sulfide electrodes can be proposed. The flow and organization of this thesis, together with its main findings and outcomes, are also detailed in this chapter.

1.1 Problem Statement

Lithium ion battery (LIB) is currently one of the most widely used forms of rechargeable energy storage system in portable electronics. They are being produced in billions of units each year to be used in cellular phones, notebook computers and many other electronic products (Figure 1.1). [1] Besides portable consumer products, LIB is also a potential candidate in various emerging applications such as electric vehicles, electric grids and energy storage system for renewable resources which are intermittent in nature like wind and solar energy. [2-5] With the increasing demand for LIB by current and prospective applications, it was predicted in 2011 that the global revenue for LIB will increase from USD9.4 billion in 2011 to USD18.6 billion by 2017. [6]

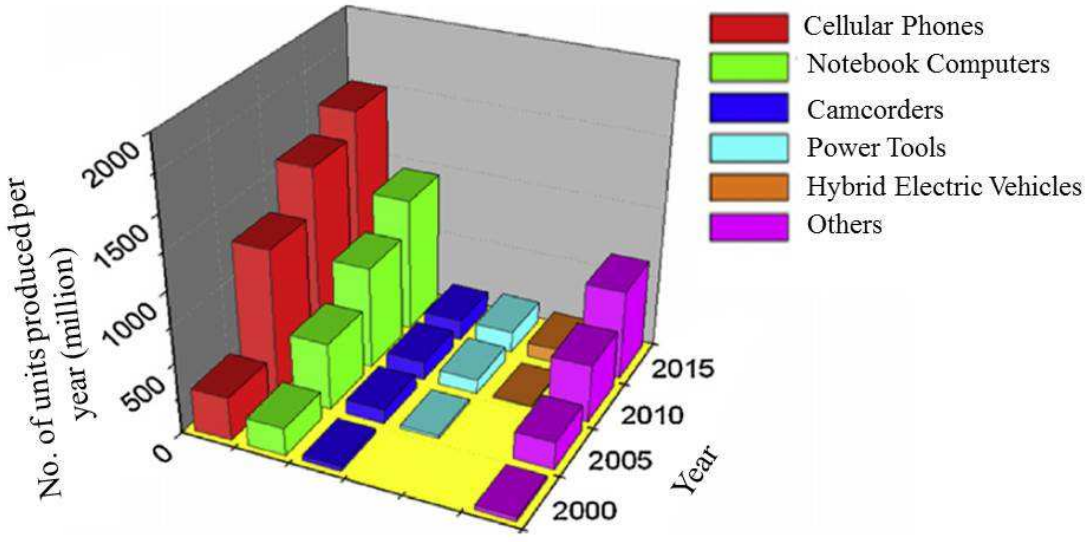

Figure 1.1: Current and forecast of lithium ion battery sales in consumer electronics and hybrid electric vehicle market. (*Reprinted from [1], © 2010, with permission from Elsevier)*

Despite the existence of various mature battery technologies like lead-acid battery and nickel-cadmium rechargeable battery in the commercial market, LIB emerged as the preferred choice of energy storage system for portable consumer electronics. The main

reasons would have to be its high gravimetric and volumetric energy densities (Figure 1.2), outstanding cycling performance and design versatility, allowing the fabrication of light (high gravimetric energy density) and compact (high volumetric energy density) batteries with different designs i.e. prismatic, coin and cylindrical (Figure 1.3) to meet the requirements for various applications.

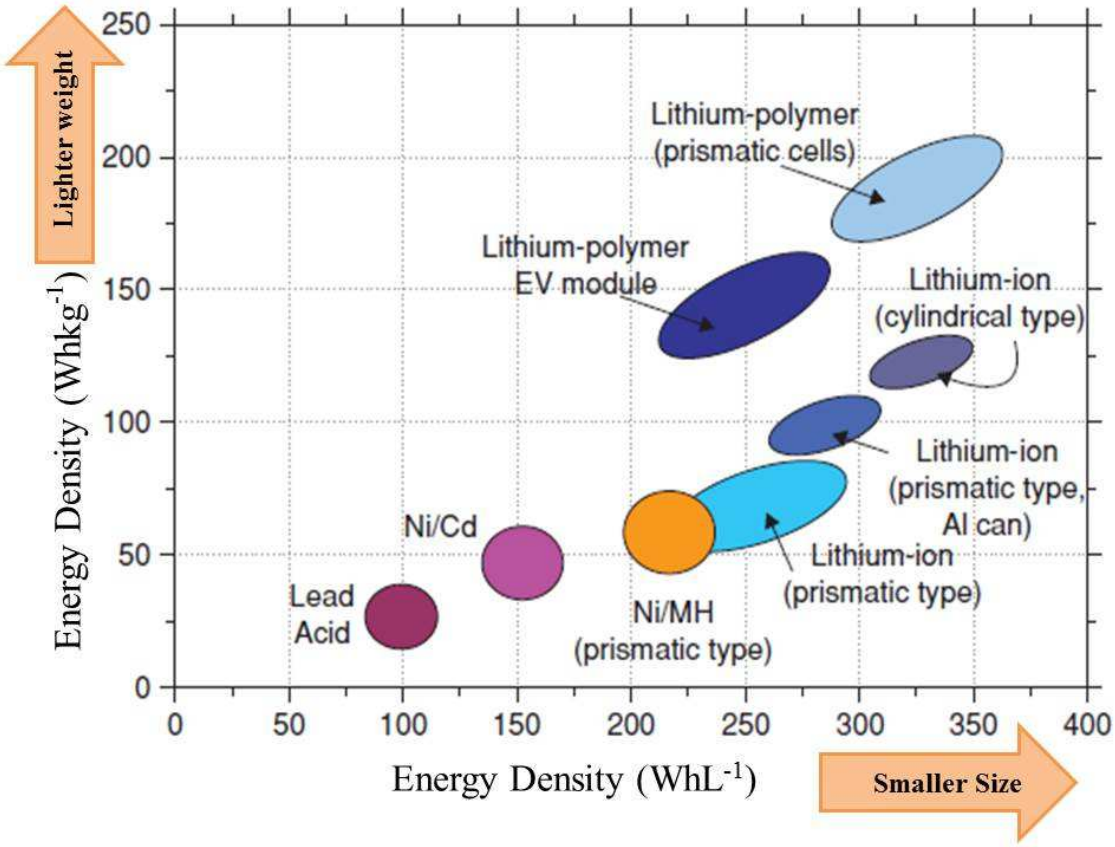

Figure 1.2: Comparison of various battery systems in terms of gravimetric and volumetric energy densities. *(Reprinted from [7], © 2013, with permission from John Wiley & Sons, Inc)*

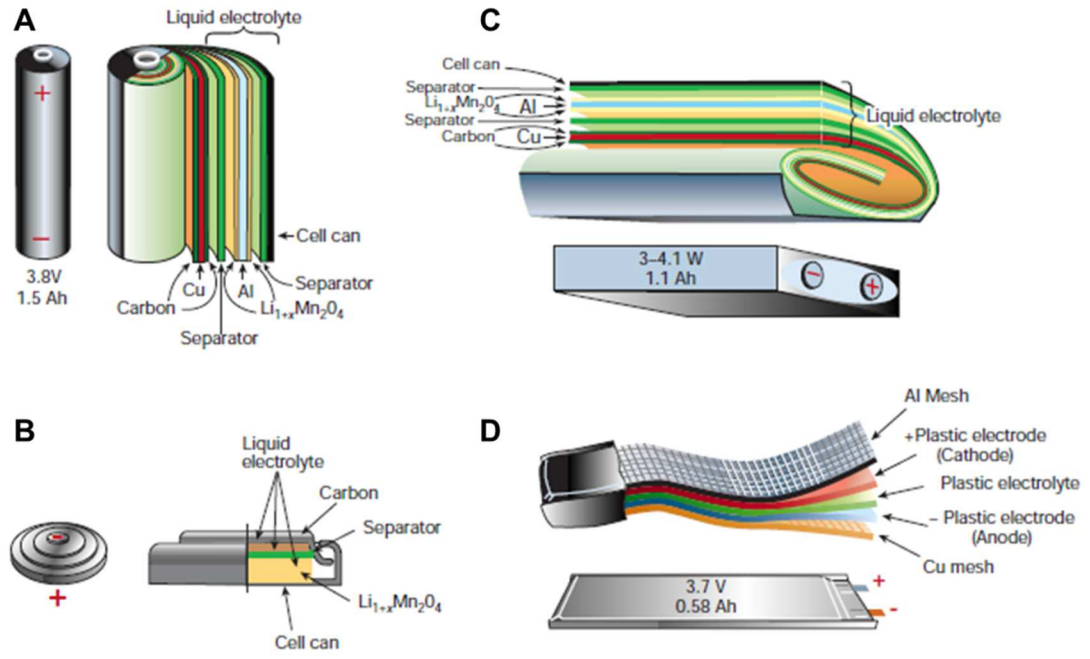

Figure 1.3: Schematic diagram of a (A) cylindrical, (B) coin, (C) prismatic and (D) thin and flat-type lithium ion battery cell configuration. *(Reprinted by permission from Macmillan Publishers Ltd: [8], © 2001)*

Typical lithium ion battery delivers a voltage of around 3.7 V and has a gravimetric and volumetric energy density of about 120 W h kg^{-1} and 320 W h L^{-1} respectively. [8, 9] These high voltage and specific energy densities made LIB a system of choice for powering up many current portable consumer devices. However, the performance of the LIB presently available in the commercial market is not sufficient to meet that required for various emerging technologies and there is still plenty of room for improvement. Hence, to perform better for existing and to match the requirements needed for potential applications, a lot of efforts have been put into the research and development of battery materials that are safe, cheap, environmentally-friendly and, at the same time, can provide higher power and energy densities. [10, 11]

1.2 Motivation

To achieve LIB with enhanced lithium storage properties, better safety aspects and lower cost, extensive research has been conducted on the various components i.e. anode, cathode and electrolyte of a LIB for the past few decades. In particular, a number of review papers on LIB have highlighted the concern for the anode materials and many works has been focused on improving its lithium storage performance. [1, 8, 12-16] Currently, graphite is the anode material used in most commercial LIB and comprehensive studies on the various forms of carbonaceous materials such as soft carbon, hard carbon and mesocarbon microbeads have also been conducted since the 1990s. Their corresponding reaction mechanisms with lithium ions, surface reactions during electrochemical cycling and so forth are constantly visible in the literatures. [17-22] Nevertheless, the limited capacity of graphitic carbons and the safety issues related to their low electrochemical potential (*vs.* Li/Li^+) have prompted scientists to search for alternative anode materials. As it is difficult to find a good replacement for graphite due to its high availability on Earth, low cost, non-toxicity and possibilities for modification, more effort is needed to explore novel concepts that can lead to the discovery of potential anode materials for advanced LIB applications.

In 2000, Poizot et al. reported on the reaction of lithium ions with various transition metal oxide (NiO, FeO, Cu_2O, CoO and Co_3O_4) nanoparticles. [23] Through his findings, he proposed a new lithium storage mechanism known as “conversion reaction” where lithium ions are released and stored through the decomposition and formation of lithium oxide (Li_2O) respectively. Since then, lithium ion has also been found to react reversibly with numerous transition metal sulfides such as iron sulfides (FeS, Fe_3S_4, FeS_2), copper sulfides (Cu_2S, CuS) and cobalt sulfides (CoS, Co_9S_8, CoS_2) through conversion reaction. [24-36] Anode materials that store lithium ions via conversion reaction are very attractive to the LIB research community as they exhibit high theoretical capacities ($\approx$ 400 – 1000 mA h g^{-1}) that can be more than 2 times that of graphite (372 mA h g^{-1}). [15, 37, 38] However, during conversion reaction, the anode material is subjected to structural reorganization and large volume change, thereby resulting in pulverization and, hence, capacity fading of the anode. Furthermore, conversion-typed electrode materials have high operating voltage typically in the range

of 1.2 – 2.5 V (*vs.* Li/Li^+), which compromises the overall voltage of the LIB i.e. reduces the overall voltage of the LIB. [37, 39, 40] All these drawbacks need to be resolved before conversion-typed electrode materials can be realised as the anode for next-generation advanced LIB.

Amongst the various conversion-typed materials, metal sulfides are particularly interesting as sulfur (S) is in the third period in the periodic table. This implies that S can exploit its 3d orbitals during bonding to attain a maximum coordination number that is greater than 4 and to adopt oxidation states in the range of -2 to +6. [41] Furthermore, S, like carbon, has a high tendency to catenate i.e. to link together atoms of the same element to form a longer chain, enabling it to form more than 30 solid allotropes like cyclohexa-S (S_6) and cycloocta-S (S_8) and various polysulfide ions like S_n^{2-} where n = 2 – 8. [41, 42] These allow S to have a rich and versatile chemistry where it can form a vast variety of binary metal sulfides. If the metal ion in the binary compound can adopt more than one oxidation states, several metal sulfide compounds with different metal to sulfur stoichiometry can be formed, providing the possibility of altering the lithium storage properties of the materials by simply varying the stoichiometric ratio between the metal and sulfide ion in the compound. However, as with all sulfur and sulfide electrodes, polysulfides will be formed during their partial reduction. [43] Although elemental sulfur is not very soluble in many organic solvents, polysulfides, on the other hand, readily dissolve in these solvents, thus increasing the viscosity and reducing the ionic conductivity of the electrolyte. [44] Furthermore, polysulfides can react with lithium metal and corrode it. All these will result in poor capacity retention and cycling performance in lithium and lithium ion batteries which employ sulfur or metal sulfide compounds as electrode materials. [44-46]

1.3 Research Scope and Objectives

In view of the poor capacity retention and cycling performance resulting from the dissolution of polysulfides into the organic electrolyte, more study needs to be carried out to find approaches that can be undertaken to improve the lithium storage performance of metal sulfide electrodes. Amongst others, it is interesting to study how

the number of sulfide ion in the stoichiometry of a metal sulfide compound i.e. Fe:S = 1:1 (FeS), 3:4 (Fe_3S_4) or 1:2 (FeS_2) affects its lithium storage properties. This dissertation aims to address the following hypothesis:

Since polysulfides can readily dissolve in organic solvents, resulting in an increase in the viscosity and reduction in the ionic conductivity of the organic electrolyte, together with the fact that polysulfides can corrode lithium metal, it is postulated that a metal sulfide compound with fewer number of sulfide ion in its stoichiometry should have better lithium storage performance due to fewer polysulfides formation.

Results from this study hope to provide an understanding as to whether having more sulfide ions in the metal sulfide compound is more beneficial or detrimental to its lithium storage performance and why the metal sulfide compound with one stoichiometry performs better than the same metal sulfide compound with another stoichiometry i.e. why FeS_2 performs better or worse than FeS. Through this understanding, possible ways of improving the lithium storage properties of the metal sulfide electrodes can be proposed.

Figure 1.4 shows the abundance of selected elements in the Earth's crust. It can be seen from this figure that iron and tin are two Earth-abundant elements that makes up 6.20×10^{-2} and 2.10×10^{-6} fraction of the Earth's crust respectively. Also, depicted in Figure 1.4 is the approximate price of selected metals which shows that one pound of iron and tin costs about USD0.10 – 0.25 and USD5 – 15 correspondingly. Due to their abundance and low cost, together with the fact that both iron and tin can adopt more than one oxidation states and, hence, can form a variety of binary phases with sulfide ions, these two elements are chosen as the cation to be studied in this thesis. In addition, iron sulfide and tin sulfide are known to store lithium ions via two different mechanisms, with the former undergoing a mixture of intercalation and conversion reaction with lithium ions, while the latter reacts with lithium ions through conversion and alloying reactions. Therefore, the study on iron sulfide and tin sulfide in this thesis also allow the evaluation of how the number of sulfide ion in the stoichiometry of these two type of metal sulfide affects their lithium storage properties.

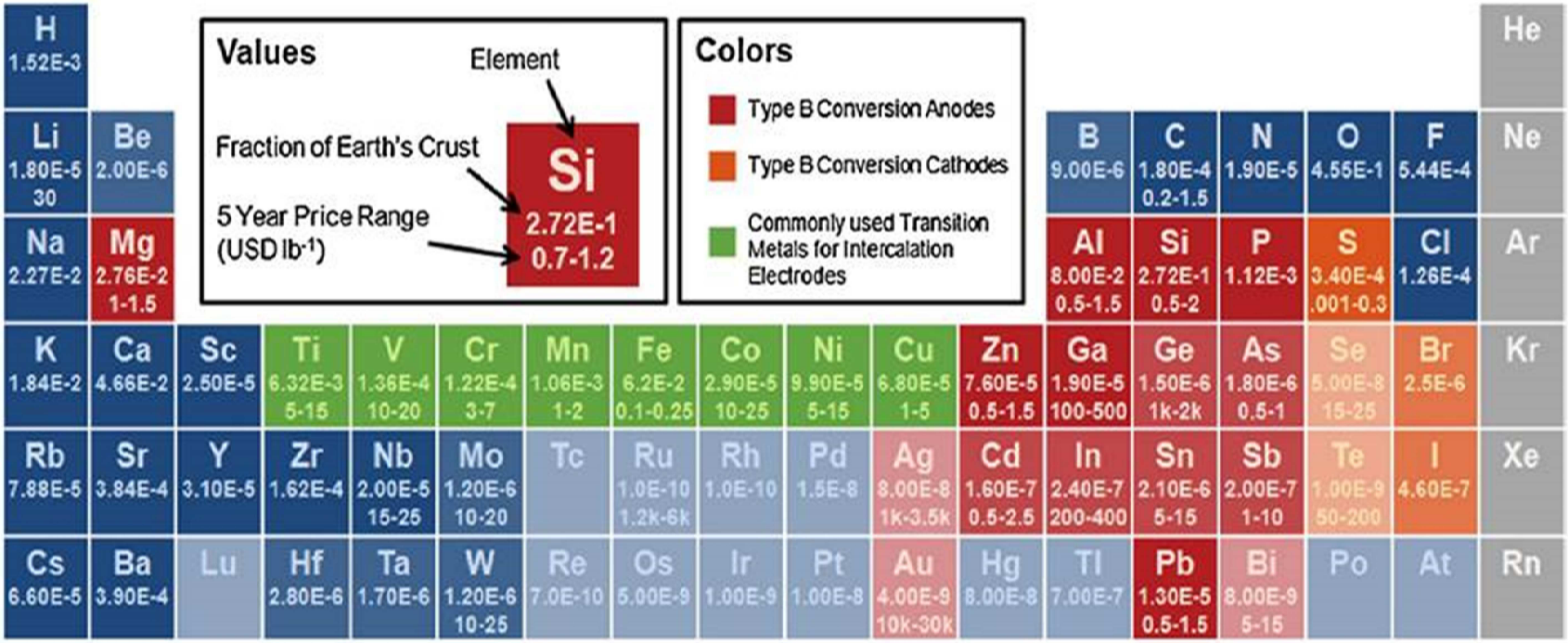

Figure 1.4: Abundance and price of selected elements that can host lithium and function as electrode material in lithium ion battery. The price range for the different elements is estimated based on their cost in a 5-year period, with the exception of germanium (Ge) which is approximated based on a 3-year range. The price range stated for carbon is based on that for 80-100 mesh natural graphite while that for sulfur is based on the Vancouver/USGS. *(Reprinted from [47], © 2015, with permission from Elsevier)*

In this dissertation, Chapter 4 focuses on the metal sulfides obtained when using iron as the cation, while Chapter 5 concentrates on that obtained when using tin as the cation. The objectives for both chapters are:

(1) To synthesize pure phases of iron sulfide and tin sulfide compounds with different stoichiometries i.e. $Fe_{1-x}S$ and FeS_2 or SnS and SnS_2 via a solution-based chemical synthesis method using the same precursors, solvents and surfactants.

(2) To characterize the as-synthesized iron sulfides and tin sulfides for their phase, purity, size and morphology.

(3) To study the effect of the molar ratio between the iron and sulfur (Fe:S) precursors on the phase and morphology of the as-synthesized iron sulfides.

(4) To study the effect of reaction time on the phase and morphology of the as-synthesized tin sulfides.

(5) To study the effect of the metal to sulfur stoichiometric ratio i.e. Fe:S or Sn:S of the as-synthesized iron sulfides or tin sulfides on their lithium storage properties and cycling performance.

Since the main objective of this thesis is to understand how by changing the number of sulfide ion in the stoichiometry of a metal sulfide compound affects its lithium storage properties, focus will only be placed on the study of pure metal sulfide phases with different metal:sulfur ratio and does not include any study on mixed phases. It should be highlighted that the iron sulfide and tin sulfide samples studied in this dissertation does not have any fanciful morphology. This is to keep the effect of particle morphology on the lithium storage properties of these samples to a minimal since it is well-known that the morphology of a sample can have great impact on its lithium storage capability. Also worth mentioning is that the iron sulfide samples, as with the tin sulfide samples, are synthesized via a solution-based chemical synthesis method using the same precursors, solvents and surfactants. Hence, any remaining surfactants

on the surface of the particles should be the same and will have similar effect on the lithium storage properties of both the iron sulfide samples. This is to prevent any difference in lithium storage performance of the two samples due to the different properties of the surfactants i.e. a surfactant with better electronic conductivity can result in enhanced charge transfer rate at the surface of the active material and better lithium storage properties for these samples.

1.4 Thesis Flow and Organization

The thesis aims to address how the amount of sulfide ion in the stoichiometry of a metal sulfide compound affects its lithium storage properties, with the focus placed on two metal sulfide systems, namely, iron sulfides (intercalation-conversion anodic material) and tin sulfides (conversion-alloying anodic material).

Chapter 1 provides a short background to the topic of lithium ion battery, highlighting the problems faced in this area of research. Based on the stated challenges, the rationale, objectives and scope for this dissertation is chosen. The flow and organization of this thesis, together with its main findings and outcomes, are also detailed in this chapter.

Chapter 2 provides a brief history on the development of various battery technologies, highlighting the numerous milestones that were achieved with emphasis placed on lithium ion battery technology. The general working principles of a lithium ion battery and the different lithium storage mechanism employed by its anode materials were also explained in this chapter. Past works that have been carried out on metal sulfides, in particular iron sulfides and tin sulfides, for lithium ion battery applications were also reviewed in this chapter.

Chapter 3 summarizes the various methodologies employed in the synthesis and characterization i.e. XRD, Raman, FESEM and TEM of the metal sulfides studied in this dissertation. The procedures used to fabricate the lithium ion cells and the experimental parameters used for measuring the electrochemical properties of the assembled battery cells were also stated in this chapter.

Chapter 4 presents the results on the synthesis of iron sulfides via a solution-based chemical synthesis method. The as-synthesized powders were characterized using XRD, FESEM, TEM and Raman spectroscopy. The effect of the molar ratio between the iron and sulfur (Fe:S) precursors on the phase and morphology of the as-synthesized products is investigated and discussed in this chapter. The effect of the iron to sulfur stoichiometric ratio of the as-synthesized iron sulfides on their lithium storage properties is also studied and presented in this chapter.

Chapter 5 presents the results on the synthesis of tin sulfides via a solution-based chemical synthesis method. The as-synthesized powders were characterized using XRD and FESEM to determine their phase, purity, and morphology and particle size. Time-dependent reaction was carried out to understand the formation mechanism of the two tin sulfide phases. The effect of the tin to sulfur stoichiometric ratio of the as-synthesized tin sulfides on their lithium storage properties is also investigated and presented in this chapter.

Chapter 6 summarizes the main findings of this dissertation and highlighted the conclusions obtained. Based on these findings and conclusions, possible future work has been recommended.

1.5 Findings and Outcomes/Originality

With the exception of a study by Cho and co-workers which compared the lithium storage performance of germanium monosulfide (GeS) and germanium disulfide (GeS_2), there is no other reports in the literature which compares the lithium storage properties of a metal sulfide with different metal:sulfur stoichiometry. [48] In addition, although Cho et al. showed that GeS performs better than GeS_2 when cycled in the voltage range of 0.01 – 1.5 V at a current density of 160 mA g^{-1}, no explanation was provided for this observation. Hence, this study is a first attempt to provide an understanding as to whether having more sulfide ions in a metal sulfide compound is more beneficial or detrimental to its lithium storage performance and why the metal

sulfide compound with one stoichiometry performs better than the same metal sulfide compound with another stoichiometry.

In this thesis, it was found that:

(1) For both iron sulfides (intercalation-conversion anodic material) and tin sulfides (conversion-alloying anodic material), the compound with a higher sulfide ion content in its stoichiometry i.e. FeS_2 and SnS_2 exhibits better lithium storage performance than its counterpart with lower sulfide ion content i.e. $Fe_{1-x}S$ and SnS when cycled in a voltage window of 0.001 – 3 V.

(2) For the iron sulfide electrodes, which undergo intercalation and conversion reaction during cycling, the superior lithium storage performance of pyrite FeS_2 is attributed to its better conductivity and reversibility of the lithiation and delithiation of FeS_y.

(3) For the tin sulfide electrodes, which undergo conversion and alloying reaction during cycling, the enhanced lithium storage capability of SnS_2 is accredited to its ability to form a thicker Li_2S layer which can provide better buffering to accommodate the large volume change in the Sn particles during their alloying and de-alloying reaction, thus maintaining the structural integrity of the electrode and result in slower capacity fading.

References:

1. Scrosati, B. and Garche, J., *Lithium batteries: status, prospects and future.* Journal of Power Sources, 2010. **195**(9): p. 2419.
2. Yang, Z., Zhang, J., Kintner-Meyer, M.C.W., Lu, X., Choi, D., Lemmon, J.P., and Liu, J., *Electrochemical energy storage for green grid.* Chemical Reviews, 2011. **111**(5): p. 3577.
3. Dunn, B., Kamath, H., and Tarascon, J.M., *Electrical energy storage for the grid: a battery of choices.* Science, 2011. **334**(6058): p. 928.

4. Thackeray, M.M., Wolverton, C., and Isaacs, E.D., *Electrical energy storage for transportation-approaching the limits of, and going beyond, lithium-ion batteries.* Energy & Environmental Science, 2012. **5**(7): p. 7854.
5. Rugolo, J. and Aziz, M.J., *Electricity storage for intermittent renewable sources.* Energy & Environmental Science, 2012. **5**(5): p. 7151.
6. Curtiss, E.T. and Eustis, S., *Lithium-Ion Battery Market Shares, Strategies, and Forecasts, Worldwide, 2011 to 2017*. 2011, WinterGreen Research, Inc.: Lexington, Massachusetts.
7. Scrosati, B., *Lithium batteries: from early stages to the future*, in *Lithium batteries*. 2013, John Wiley & Sons, Inc. p. 21-38.
8. Tarascon, J.M. and Armand, M., *Issues and challenges facing rechargeable lithium batteries.* Nature, 2001. **414**(6861): p. 359.
9. Scrosati, B., Hassoun, J., and Sun, Y.K., *Lithium-ion batteries. A look into the future.* Energy & Environmental Science, 2011. **4**(9): p. 3287.
10. Armand, M. and Tarascon, J.M., *Building better batteries.* Nature, 2008. **451**(7179): p. 652.
11. Chiang, Y.M., *Building a better battery.* Science, 2010. **330**: p. 1485
12. Winter, M., Besenhard, J.O., Spahr, M.E., and Novák, P., *Insertion electrode materials for rechargeable lithium batteries.* Advanced Materials, 1998. **10**(10): p. 725.
13. Tirado, J.L., *Inorganic materials for the negative electrode of lithium-ion batteries: state-of-the-art and future prospects.* Materials Science & Engineering R-Reports, 2003. **40**(3): p. 103.
14. Bruce, P.G., *Energy storage beyond the horizon: rechargeable lithium batteries.* Solid State Ionics, 2008. **179**(21-26): p. 752.
15. Li, H., Wang, Z., Chen, L., and Huang, X., *Research on advanced materials for Li-ion batteries.* Advanced Materials, 2009. **21**(45): p. 4593.
16. Goodenough, J.B. and Kim, Y., *Challenges for rechargeable Li batteries.* Chemistry of Materials, 2010. **22**(3): p. 587.
17. Dahn, J.R., Zheng, T., Liu, Y.H., and Xue, J.S., *Mechanisms for lithium insertion in carbonaceous materials.* Science, 1995. **270**(5236): p. 590.
18. Aurbach, D., Markovsky, B., Weissman, I., Levi, E., and Ein-Eli, Y., *On the correlation between surface chemistry and performance of graphite negative electrodes for Li ion batteries.* Electrochimica Acta, 1999. **45**(1): p. 67.

19. Flandrois, S. and Simon, B., *Carbon materials for lithium-ion rechargeable batteries.* Carbon, 1999. **37**(2): p. 165.
20. Nishi, Y., *The development of lithium ion secondary batteries.* Chemical Record, 2001. **1**(5): p. 406.
21. Aurbach, D., Zinigrad, E., Cohen, Y., and Teller, H., *A short review of failure mechanisms of lithium metal and lithiated graphite anodes in liquid electrolyte solutions.* Solid State Ionics, 2002. **148**(3-4): p. 405.
22. Kaskhedikar, N.A. and Maier, J., *Lithium storage in carbon nanostructures.* Advanced Materials, 2009. **21**(25-26): p. 2664.
23. Poizot, P., Laruelle, S., Grugeon, S., Dupont, L., and Tarascon, J.M., *Nano-sized transition-metal oxides as negative-electrode materials for lithium-ion batteries.* Nature, 2000. **407**(6803): p. 496.
24. Dominko, R., Arcon, D., Mrzel, A., Zorko, A., Cevc, P., Venturini, P., Gaberscek, M., Remskar, M., and Mihailovic, D., *Dichalcogenide nanotube electrodes for Li-ion batteries.* Advanced Materials, 2002. **14**(21): p. 1531.
25. Lai, C.H., Huang, K.W., Cheng, J.H., Lee, C.Y., Hwang, B.J., and Chen, L.J., *Direct growth of high-rate capability and high capacity copper sulfide nanowire array cathodes for lithium-ion batteries.* Journal of Materials Chemistry, 2010. **20**(32): p. 6638.
26. Han, Y., Wang, Y.P., Gao, W.H., Wang, Y.J., Jiao, L.F., Yuan, H.T., and Liu, S.X., *Synthesis of novel CuS with hierarchical structures and its application in lithium-ion batteries.* Powder Technology, 2011. **212**(1): p. 64.
27. Zhang, D., Tu, J.P., Xiang, J.Y., Qiao, Y.Q., Xia, X.H., Wang, X.L., and Gu, C.D., *Influence of particle size on electrochemical performances of pyrite FeS2 for Li-ion batteries.* Electrochimica Acta, 2011. **56**(27): p. 9980.
28. Paolella, A., George, C., Povia, M., Zhang, Y., Krahne, R., Gich, M., Genovese, A., Falqui, A., Longobardi, M., Guardia, P., Pellegrino, T., and Manna, L., *Charge transport and electrochemical properties of colloidal greigite (Fe3S4) nanoplatelets.* Chemistry of Materials, 2011. **23**(16): p. 3762.
29. Wang, Q., Jiao, L., Han, Y., Du, H., Peng, W., Huan, Q., Song, D., Si, Y., Wang, Y., and Yuan, H., *CoS2 hollow spheres: fabrication and their application in lithium-ion batteries.* Journal of Physical Chemistry C, 2011. **115**(16): p. 8300.
30. Shi, W., Zhu, J., Rui, X., Cao, X., Chen, C., Zhang, H., Hng, H.H., and Yan, Q., *Controlled synthesis of carbon-coated cobalt sulfide nanostructures in oil phase*

with enhanced Li storage performances. Acs Applied Materials & Interfaces, 2012. **4**(6): p. 2999.

31. Gu, Y., Xu, Y., and Wang, Y., *Graphene-wrapped CoS nanoparticles for high-capacity lithium-ion storage.* Acs Applied Materials & Interfaces, 2013. **5**(3): p. 801.
32. Chen, G.Y., Wei, Z.Y., Jin, B., Zhong, X.B., Wang, H., Zhang, W.X., Liang, J.C., and Jiang, Q., *Hydrothermal synthesis of copper sulfide with novel hierarchical structures and its application in lithium-ion batteries.* Applied Surface Science, 2013. **277**: p. 268.
33. Feng, C., Zhang, L., Wang, Z., Song, X., Sun, K., Wu, F., and Liu, G., *Synthesis of copper sulfide nanowire bundles in a mixed solvent as a cathode material for lithium-ion batteries.* Journal of Power Sources, 2014. **269**: p. 550.
34. Liu, X., Kim, H.S., Hong, J.H., Xu, Z., Xiao, H., Ahn, I.S., and Kim, K.W., *Electrochemical properties of mechanically alloyed Ni-doped FeS2 cathode materials for lithium-ion batteries.* Powder Technology, 2014. **256**: p. 545.
35. Liu, W.L., Rui, X.H., Tan, H.T., Xu, C., Yan, Q.Y., and Hng, H.H., *Solvothermal synthesis of pyrite FeS2 nanocubes and their superior high rate lithium storage properties.* RSC Advances, 2014. **4**(90): p. 48770.
36. Rui, X., Tan, H., and Yan, Q., *Nanostructured metal sulfides for energy storage.* Nanoscale, 2014. **6**(17): p. 9889.
37. Cabana, J., Monconduit, L., Larcher, D., and Rosa Palacin, M., *Beyond intercalation-based Li-ion batteries: the state of the art and challenges of electrode materials reacting through conversion reactions.* Advanced Materials, 2010. **22**(35): p. E170.
38. Lai, C.H., Lu, M.Y., and Chen, L.J., *Metal sulfide nanostructures: synthesis, properties and applications in energy conversion and storage.* Journal of Materials Chemistry, 2012. **22**(1): p. 19.
39. Guo, Y.G., Hu, J.S., and Wan, L.J., *Nanostructured materials for electrochemical energy conversion and storage devices.* Advanced Materials, 2008. **20**(15): p. 2878.
40. Arico, A., Bruce, P., Scrosati, B., Tarascon, J., and Schalkwijk, W., *Nanostructured materials for advanced energy conversion and storage devices.* Nat Mater, 2005. **4**: p. 366

41. B., M., *Chalcogens and metal chalcogenides*, in *Electrochemistry of metal chalcogenides*, F. S., Editor. 2010, Springer Berlin Heidelberg. p. 1-56.
42. Meyer, B., *Solid allotropes of sulfur.* Chemical Reviews, 1964. **64**(4): p. 429.
43. Rauh, R.D., Shuker, F.S., Marston, J.M., and Brummer, S.B., *Formation of lithium polysulfides in aprotic media.* Journal of Inorganic and Nuclear Chemistry, 1977. **39**(10): p. 1761.
44. Yamin, H. and Peled, E., *Electrochemistry of a nonaqueous lithium/sulfur cell.* Journal of Power Sources, 1983. **9**(3): p. 281.
45. Yamin, H., Gorenshtein, A., Penciner, J., Sternberg, Y., and Peled, E., *Lithium sulfur battery - oxidation/reduction mechanisms of polysulfides in THF solutions.* Journal of the Electrochemical Society, 1988. **135**(5): p. 1045.
46. Jung, H., Park, C.M., and Sohn, H.J., *Bismuth sulfide and its carbon nanocomposite for rechargeable lithium-ion batteries.* Electrochimica Acta, 2011. **56**(5): p. 2135.
47. Nitta, N., Wu, F., Lee, J.T., and Yushin, G., *Li-ion battery materials: present and future.* Materials Today, 2015. **18**(5): p. 252.
48. Cho, Y.J., Im, H.S., Myung, Y., Kim, C.H., Kim, H.S., Back, S.H., Lim, Y.R., Jung, C.S., Jang, D.M., Park, J., Cha, E.H., Choo, S.H., Song, M.S., and Cho, W.I., *Germanium sulfide(ii and iv) nanoparticles for enhanced performance of lithium ion batteries.* Chemical Communications, 2013. **49**(41): p. 4661.

Chapter 2

Literature Review

This chapter provides a brief history on the development of various battery technologies, highlighting the numerous milestones that were achieved with emphasis placed on lithium ion battery technology. The general working principles of a lithium ion battery and the different lithium storage mechanism employed by its anode materials were also explained in this chapter. Past works that have been carried out on metal sulfides, in particular iron and tin sulfides, for lithium ion battery applications were also reviewed in this chapter. Although many different approaches have been attempted by the research community to enhance the lithium storage performance of metal sulfide electrodes, there are still plenty of room for improvement. In order to find more effective solution to the problem of polysulfide dissolution and to better improve the lithium storage capability of metal sulfide electrodes, it is important to first understand the impact of the amount of sulfide ions in a metal sulfide compound on its polysulfide dissolution problem and lithium storage properties and why the metal sulfide compound with one stoichiometry performs better than that with another stoichiometry. Through this understanding, more effective ways of improving the lithium storage properties of the metal sulfide electrodes can be proposed. However, no such study has been reported in the literature to date.

2.1 History of Batteries

Batteries, also known as electrochemical or galvanic cells are devices that can convert the chemical energy stored in them into electrical energy via electrochemical reduction-oxidation (redox) reactions. [1] These redox reactions, being thermodynamically favourable, will occur spontaneously when two materials with different standard reduction potentials are linked together by an electronic load. [2] In general, batteries can be broadly divided into two different categories, namely, primary batteries and secondary batteries. Primary batteries are those that cannot be easily or effectively recharged and, therefore, is disposed after a single discharge or use; while secondary batteries, also known as rechargeable batteries, can be charged and discharged repeatedly.

The discovery of batteries is widely believed to occur around the late 18th century as a result of the dispute between two Italian physicists, Luigi Galvani and Alessandro Volta. In 1781, Galvani observed the twitching of a frog's leg when he placed two different metals in contact with that frog's leg (Figure 2.1). From his observation, he proposed that animals can generate electricity. [3] However, this hypothesis was being challenged in 1794 when Volta claimed that the twitching of the frog's leg is caused by the stimulus of the two metal strips and not because of the generation of electricity by the animal's muscle itself. To support his postulation, Volta invented and demonstrated the production of electricity from the very first battery in 1800. [4] This first battery, which is known as "Volta's pile" or "voltaic pile", is formed by connecting copper and zinc disks in an alternating sequence where each pair of copper-zinc disk is separated by a cloth that is wetted with brine solution (Figure 2.2).

The invention of the voltaic pile by Volta provided a new concept for the conversion and storage of energy, inspiring and accelerating the development of many different electrochemical systems. Table 2.1 highlights some of the milestones in the history of battery development. Notably, following the invention of the voltaic pile in 1800, French physicist Raymond Gaston Planté came out with the first lead-acid battery in 1859, which employs lead oxide as its positive electrode, metallic lead as its negative electrode and sulfuric acid as the electrolyte. [5] This lead-acid battery can be

discharged and electrically charged back again by applying an external bias to its electrodes. As this battery can be discharged and charged for many times, lead-acid batteries are also known as a type of “rechargeable battery”. In fact, the lead-acid battery is the oldest rechargeable battery that was invented and is also the first rechargeable battery to be commercialized.

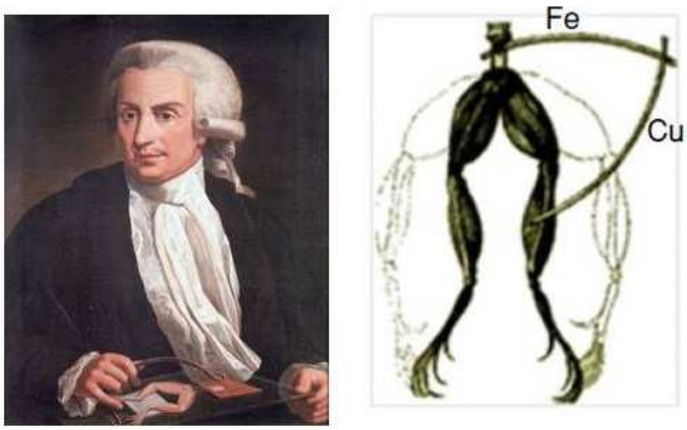

Figure 2.1: Luigi Galvani and his classical experiment on frog’s leg. *(Reprinted from [4], © 2013, with permission from John Wiley & Sons, Inc)*

Figure 2.2: Alessandro Volta and his Volta’s pile. *(Reprinted from [4], © 2013, with permission from John Wiley & Sons, Inc)*

Another important discovery in the history of battery development would have to be the nickel-cadmium (Ni-Cd) rechargeable battery that was created by Swedish engineer, Waldmar Jungner in 1899. This Ni-Cd cell uses a mixture of nickel hydroxide and graphite as its cathode, a mixture of cadmium oxide or cadmium hydroxide with iron or iron-based compounds as its anode and potassium hydroxide as its electrolyte. [6] Being the second rechargeable battery that was commercialized, the Ni-Cd battery has a higher gravimetric and volumetric energy density but also a higher cost compared to the lead-acid battery.

Innovations are usually an outcome resulting from the need to solve certain problems or to meet certain demands in the society. Therefore, the outburst of portable consumer electronic products in the market and the occurrence of the first oil crisis in the 1970s have triggered many inventions in the field of battery technology. With more work being put into creating a battery that has high capacity and yet, at the same time, is light in weight and small in size so as to meet the continuing need for better energy storage systems, it soon dawned on researchers that the crucial limiting factor in a battery system would be the choice of its electrodes. It was noticed that the combination of materials used as electrodes at that time has limited theoretical capacity, thereby restricting the specific gravimetric and volumetric energy density of those energy storage systems.

A breakthrough in the development of battery technology occurred when it was first shown that lithium can be employed as an electrode material. In comparison to the other elemental metals in the periodic table, lithium (Li) has a very small atomic weight of 6.941 g mol^{-1}, a low density of 0.534 g cm^{-3} and one of the lowest standard electrode potential (-3.04 V versus standard hydrogen electrode), allowing batteries with high gravimetric and volumetric energy density and high output voltage to be fabricated when Li is chosen as the anode material. [7] In fact, when lithium, which has a higher specific capacity (3860 A h g^{-1}) compared to zinc (820 A h g^{-1}) is used as an anode material in a battery with an iodine-based material as the cathode (lithium-iodine battery), a high practical energy density (≈ 250 W h kg^{-1}) that is nearly five times higher than a zinc-mercury oxide battery can be attained. [3]

Table 2.1: Selected milestones in the history of battery development. [2, 3]

Year	Cell	Inventor
1800	Volta's Pile	Alessandro Volta
1836	Daniel Cell	John Frederic Daniel
1859	Lead–Acid Battery ($Pb/H_2SO_4/PbO_2$)	Raymond Gaston Planté
1866	Leclanché Cell	Georges - Lionel Leclanché
1888	Zinc–Carbon Dry Cell	Carl Gassner
1899	Nickel-Cadmium Battery	Waldmar Jungner
1946	Alkaline Manganese Secondary Cell	Union Carbide Company
1955	Alkaline Battery	Lewis Urry
1972	Lithium Primary Battery (Li/Organic Electrolyte/CFx)	Matsushita
1972	Solid Lithium Iodine Battery (Li/LiI/I-PVP)	Moser
1975	Lithium–Manganese Cell	Sanyo Electric Co
1977	Rechargeable Lithium Battery (Li/Organic Electrolyte/TiS_2)	Michael Stanley Whittingham
1980	Rocking Chair Battery (Li_xWO_2/Organic Electrolyte/TiS_2)	Bruno Scrosati
1980	Lithium–Molybdenum Disulfide	Moli Energy
1990	Nickel–Metal Hydride Battery	Samsung
1991	Lithium Ion Battery (C/Organic Electrolyte/$LiCoO_2$)	Sony

Although lithium primary batteries were already very well-established as commercial products by the 1970s, the widespread usage of rechargeable lithium batteries was prevented due to some serious operational faults i.e. overheating and thermal runaway associated to its metallic lithium anode. Hence, to improve the safety of this battery, work has been done to search for a less aggressive material to replace the highly

reactive lithium metal. This prompted the research on lithium ion battery (LIB), a modified version of lithium battery that uses the more reliable lithiated compounds instead of lithium metal as its electrode, thus improving the safety of the cell. The whole concept of LIB started back in the late 1970s [8-10] and obtained practical demonstration by building on two important discoveries: (1) the discovery of lithium cobalt oxide (Li_xCoO_2), a lithium-intercalation material with high working voltage by John Goodenough et. al in 1979 [11] and (2) the demonstration of low working voltage, carbonaceous materials that can undergo lithium insertion and extraction reversibly by Rachid Yamazi in 1980. [12] Following the assembly and patenting of a prototype LIB cell by Akira Yoshino and coworkers in 1985 [13], the very first commercial LIB was released by Sony Cooperation in June 1991 [14, 15] and remained one of the batteries of choice for portable electronics like notebook computers and cellular phones till today.

2.2 Basic Principles of Lithium Ion Battery

A lithium ion battery, like all other electrochemical cells, is generally made up of two electrodes separated by an electrolyte, as shown in Figure 2.3. These two electrodes in the cell have different standard reduction potentials and, hence, redox reactions should occur spontaneously between them when they are connected together by an electronic load. [2] Among the two electrodes, the electrode which has a lower positive reduction potential is commonly known as the negative electrode or anode, while that with a higher positive reduction potential is known as the positive electrode or cathode. [16] The electrolyte serves as a medium for the transfer of charge such as lithium ions in the case of LIB between the two electrodes inside the cell. A wide variety of electrolyte choices are available for use in batteries and the most common one would be liquid electrolyte, either aqueous or non-aqueous, with salts, alkalis or acids dissolved in it to give the electrolyte its ionic conductivity. [17] Other electrolytes used in electrochemical cells include polymer, glass and ceramic electrolytes. To prevent short-circuiting of the battery cell, a separator is placed between the two electrodes. This separator should have with good ionic but poor electronic permeability, allowing ions and not electrons to pass through it.

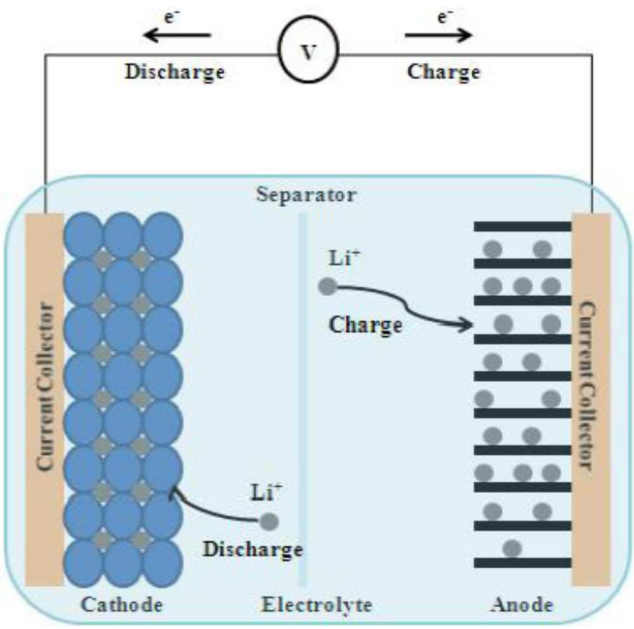

Figure 2.3: Schematic diagram of a lithium ion battery cell. (*Reprinted from [18], © 2012, with permission from Elsevier)*

When the LIB is in its charged state, lithium ions are "stored" in the anode. During discharging, the lithium ions in the anode are extracted and transported through the electrolyte and separator to reach the cathode, where they are inserted into the positive electrode. At the same time, the anode loses electrons (gets oxidized) and these electrons moved through an external circuit to reach the cathode, thereby reducing it. This movement of electrons from the negative to the positive electrode allows the user to tap on it to power up devices for various applications. To recharge the LIB, an external voltage is applied to the electrodes, causing the lithium ions to be extracted from the cathode and inserted into the anode i.e. reverse of the discharging process. As the energy conversion process in a LIB occurs via the transportation of lithium ions to and fro the two electrodes, such a cell is also commonly referred to as a rocking-chair battery.

Since the commercialization of the very first LIB by Sony Corporation in 1991, vast amount of work has been carried out to further improve its energy storage properties so

as to meet the increasing demand for better and safer energy storage systems by both existing and emerging applications in the society. To achieve better lithium storage performance, researchers focuses a lot of effort in finding new cathode [19-24] and anode [25-32] materials that has higher energy density or power than the current commercial choice i.e. graphite and lithium cobalt oxide ($LiCoO_2$).

2.3 Anode Materials for Lithium Ion Battery

Carbon-based materials such as pyrolytic carbon were first reported as negative electrode for LIB in 1989 [33, 34] and, since then, they have become a popular choice as anode materials in LIB. Amongst these carbonaceous materials, graphite, in particular, has gathered a lot of attention as an alternative to the lithium metal anode in rechargeable lithium ion batteries because of its ability to accommodate repetitive insertion and extraction of lithium ions into and out of its lattice. Other reasons for using graphite as an anode material in LIB include its small irreversible capacity, good cycling stability, a long and almost flat plateau in its charge/discharge voltage profiles and, most importantly, its high abundance and low cost. [35] In fact, graphite is used as the anode material in the first commercial LIB and has remained as the predominant anode material used in today's commercial LIB. However, graphitic carbons such as graphite only have limited theoretical capacities of about 372 mA h g^{-1} (based on the formation of LiC_6) and observed capacities in the range of 280 – 330 mA h g^{-1}, depending on the type of graphitic carbon material. [36] And, this low capacity value is not sufficient to meet the requirements of new and emerging technologies like electric vehicles and hybrid electric vehicles. Furthermore, the electrochemical potential value of LiC_6 (*vs.* Li/Li^+) is very close to that of lithium metal. Although this low potential enables the fabrication of batteries with high terminal voltage when coupled with a cathode material that has a high reduction potential, there are several safety concerns with regards to the use of graphitic carbon anode in rechargeable LIB. The practically-zero electrochemical potential of LiC_6 (*vs.* Li/Li^+) could result in possible lithium deposition at the surface of the anode especially during fast charging under cold temperatures, thus degrading the performance of the battery and, in the worst case, leading to a thermal runaway and fire. In fact, the International Civil Aviation

Organization has recently imposed a ban for the transportation of LIB shipment via passenger aircraft due to LIB being a fire hazard which requires special firefighting systems. [37] Hence, many researchers have been working on finding other promising anode materials with higher volumetric/gravimetric capacities and better safety aspects than graphitic carbon to meet society's demand for better and safer energy storage systems.

In a commercial battery system, an ideal anode material should meet the following criteria:

(1) Have an adequate electrochemical potential value (*vs.* Li/Li^+) that is slightly above that of lithium metal and, yet, not too close to it.

(2) Have high specific capacity (A h g^{-1} or A h cm^{-1}) and energy density (W h g^{-1} or W h cm^{-1}) in terms of volume and weight

(3) Have good cycling stability, allowing it to maintain its capacity after prolong cycling

(4) Have both good electrical and ionic conductivities

(5) Have good chemical stability in the electrolyte

(6) Abundance on Earth

(7) Have low material and manufacturing cost

(8) Should be non-toxic and safe to handle

Table 2.2: Various anode materials for lithium ion battery and their characteristics. [36, 38-42]

Host Material	Theoretical Specific Capacity (mA h g^{-1})	Potential (*vs.* Li/Li^+)	Remarks
Graphite	372	0.1–0.2	Volume change: ~11%
$Li_4Ti_5O_{12}$	175	1.55	High voltage, Negligible volume change
Si	4198	0.5–1	Poor cycling, Volume change: 320%
Sn	993	<0.5	Poor cycling, Volume change: 350%
Al	2235	<0.3	Poor cycling, Volume change: 238%
Bi	385	<0.8	Volume change: 115%
SnO_2	782	<0.5	Large initial irreversible loss
Fe_2O_3	1007	1.6	High voltage, Low cost
CoO	715	1.8	High voltage
FeS_2	890	1.5	High voltage, Poor cycling

Table 2.2 shows some anode materials used in or studied for potential application in lithium ion batteries. These negative electrode materials can be broadly classified into three major types, namely, insertion-type materials, alloying-type materials and conversion-type materials, depending on how they store Li ions.

2.3.1 Insertion / Intercalation-Type Anode Materials

Insertion-type materials, also known as intercalation-type materials, for LIB store lithium ions by inserting them into the space between the host layers, as illustrated in Figure 2.4. [43] During charging, lithium ions are inserted into the interspace between the anode material layers and, during discharging, these lithium ions were extracted from the host layers through a process known as de-intercalation or de-insertion.

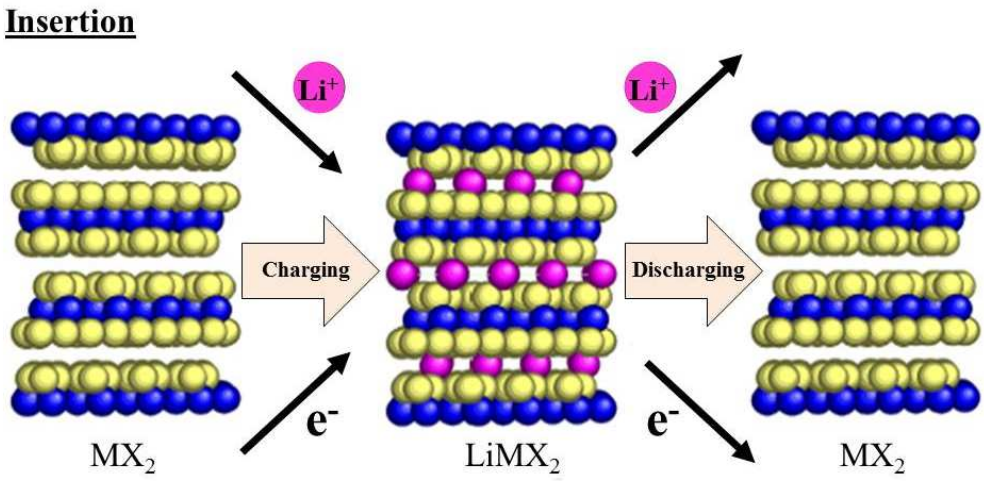

Figure 2.4: Schematic representation showing the insertion or intercalation reaction. (*Reprinted from [44], © 2007, with permission from Elsevier)*

One of the most widely studied insertion-type anodic materials for application in lithium ion batteries would have to be graphite. Graphite is a crystalline material with layered structure. It is made up of carbon atoms that are sp^2-bonded to each other, forming layers of graphene and these graphene layers are held together to its neighbouring graphene layers by weak van der Waals forces, as shown in Figure 2.5. During charging, the lithium ions can intercalate into the space between the graphene layers to form Li_xC_6 and, during discharging, they can be extracted from this interlayer spacing to form back graphite, as shown by the reaction in Equation 2.1. This intercalation and de-intercalation process causes the graphite anode to undergo a

volume change of at most 11%. [45] As this volume change is not too large, graphite anodes do not experience excessive mechanical strain during charging-discharging cycling, allowing them to achieve a stable and reversible capacity of about 330 mA h g^{-1}. [36]

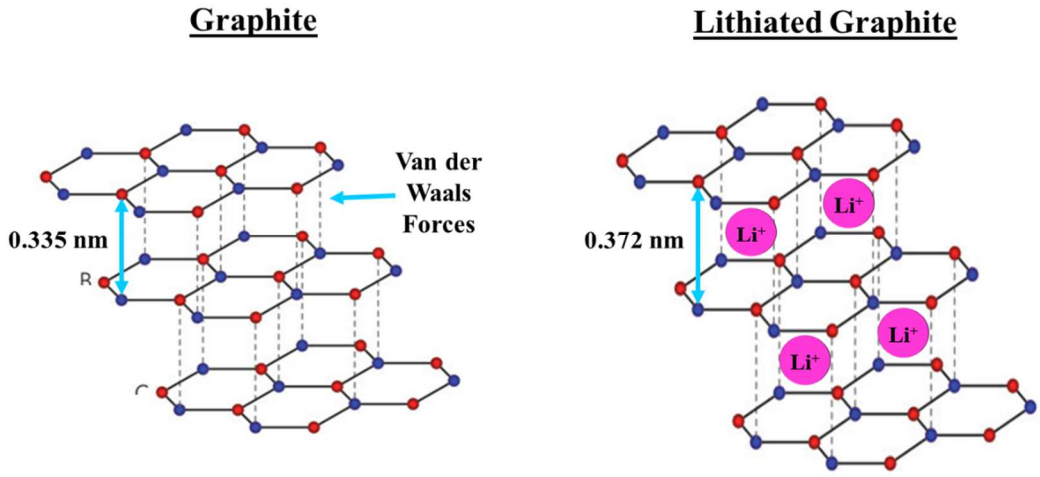

Figure 2.5: Schematic representation showing the intercalation and de-intercalation of lithium ions into and out of graphite and the corresponding change in its lattice parameter.

$$C_6 + x\,Li^+ + x\,e^- \underset{\text{Discharging}}{\overset{\text{Charging}}{\rightleftharpoons}} Li_xC_6 \quad ; \quad 0 \le x \le 1$$

Equation 2.1

Lithium titanate spinel ($Li_4Ti_5O_{12}$) is another insertion-type anode material that has gained extensive research interest. It has a theoretical gravimetric specific capacity of 175 mA h g^{-1} as each formula unit of $Li_4Ti_5O_{12}$ can accommodate the insertion of up to 3 Li atoms into its lattice (Equation 2.2). Although the theoretical capacity of $Li_4Ti_5O_{12}$ is lower than that of graphite, it has an interesting property that makes it a very attractive choice as the anode in LIB. $Li_4Ti_5O_{12}$ is a well-known zero-strain material for lithium insertion. [46] When lithium ion is intercalated into $Li_4Ti_5O_{12}$, the material undergoes

a phase transformation from a spinel structure to a rock salt structure, resulting in a small volume change of only 0.2% in the cell volume (Figure 2.6). This enables $Li_4Ti_5O_{12}$ to exhibit good structural stability and long cycling life as its small volume change during intercalation and de-intercalation implies that the material will experience negligible lattice strain during cycling. [47-49]

$$Li_4Ti_5O_{12} + 3\,Li^+ + 3\,e^- \underset{\text{Discharging}}{\overset{\text{Charging}}{\rightleftharpoons}} Li_7Ti_5O_{12}$$

Equation 2.2

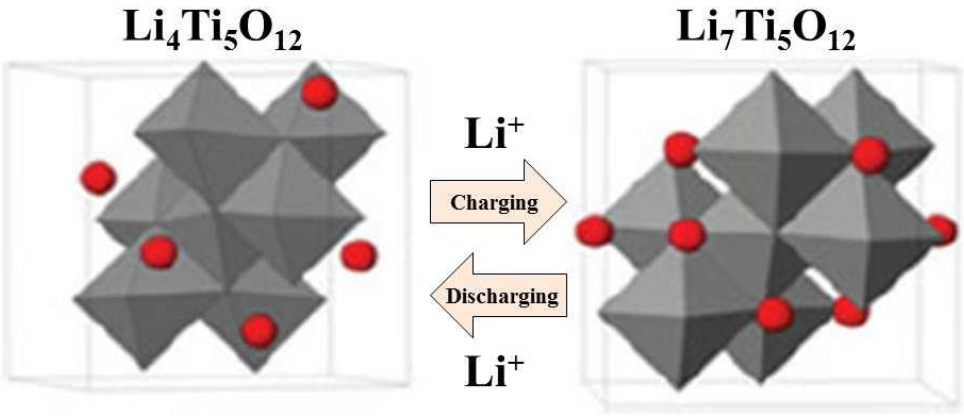

Figure 2.6: Schematic representation showing the negligible volume change during intercalation and de-intercalation of lithium ions into and out of lithium titanate. *(Reprinted from [50], © 2013, with permission from John Wiley & Sons, Inc)*

Other materials that store Li ions via intercalation reaction include some transition metal oxides such as the various polymorphs of titanium dioxide (TiO_2) and tungsten oxide (WO_2). [51-54] However, insertion reaction mechanism only allows a restricted number of Li atoms, usually about one or at most three Li atoms per formula unit, to be intercalated into the anode. This limits the maximum capacity attainable by the

electrode material. Thus, new anode chemistries must be developed to increase the capacity of the electrode materials.

2.3.2 Alloying-Type Anode Materials

A second type of anode materials for lithium ion batteries is the alloying-type materials. In 1971, Dey reported that metallic lithium can electrochemically alloy and de-alloy with numerous metals in a liquid organic electrolyte at room temperature. [55] Since then, alloying-type anode materials for LIB, which includes mainly metals such as aluminium (Al), germanium (Ge), lead (Pb), silver (Ag), indium (In), zinc (Zn), and antimony (Sb) have gained widespread attention, with silicon (Si) and tin (Sn) being two of the more attractive candidates. [56-59]

Equation 2.3 shows a generalized equation for a typical alloying reaction where M can be either an element like Si or a compound like SnSb. [60] During charging, the lithium ions diffuse from the cathode to the anode, where they alloy with the alloying-type anode material, M to form a lithium-based compound, Li_xM. This process is reversed during discharging, where the lithium ions are extracted from the lithiated anode, Li_xM to form back to the initial alloying-type anode material, M.

$$M + x\,Li^+ + x\,e^- \underset{\text{Discharging}}{\overset{\text{Charging}}{\rightleftharpoons}} Li_xM$$

where M *can be an element or compound*

Equation 2.3

Typically, lithium-alloying anodes have much higher theoretical volumetric and gravimetric capacities than that of conventional graphite. Fully-lithiated silicon ($Li_{4.4}Si$), for example, has a theoretical capacity of about 4200 mA h g^{-1}, which is more than 10-fold higher than that of graphite (LiC_6), whose theoretical capacity is only 372 mA h g^{-1}. Sn, another widely-studied alloying-type anode material for LIB, can alloy with lithium ions to form $Li_{4.4}Sn$, giving it a theoretical capacity (990 mA h g^{-1}) which is also much higher than that of graphite. Although alloying-typed anode materials have high theoretical capacities, this class of anode materials also has their own problems. Unlike the relatively open crystal framework of graphite, metals tend to have a more densely-packed structure. Therefore, when lithium ions are inserted into these metal anodes to form an alloy, the electrodes usually experience massive volume change as illustrated by the schematic representation in Figure 2.7. [61, 62] Si, for instance, is expanded by about 320% upon lithiation to form $Li_{4.4}Si$ [38], while Sn undergoes a volume change of 350% when it alloys with lithium ions to form $Li_{4.4}Sn$. [39] This large volume change in the material that occurs during alloying and de-alloying process generates mechanical strain, resulting in the cracking and rapid capacity fading of the anode upon repeated cycling.

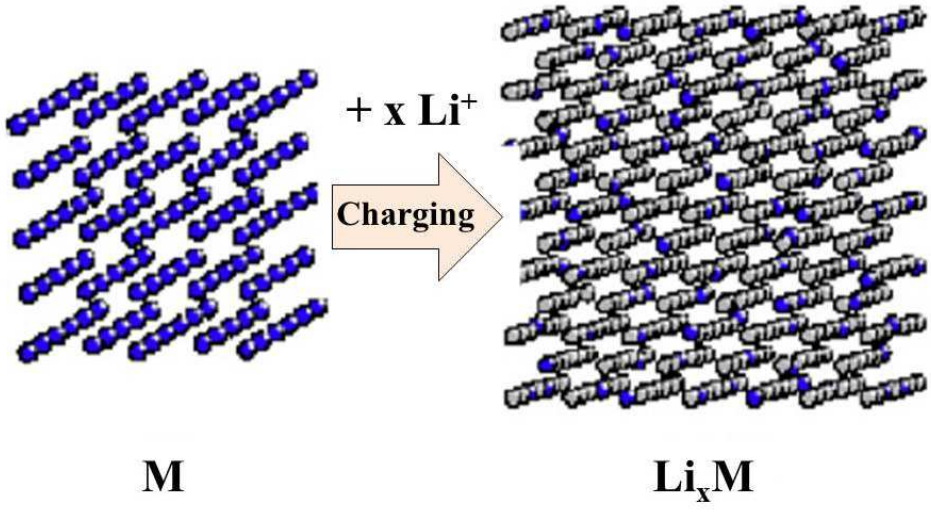

Figure 2.7: Schematic representation showing the alloying reaction. (*Reprinted from [63], © 2010, with permission from Elsevier)*

While the high capacities of alloying-typed materials make them an attractive choice as anodes in high energy density lithium-ion batteries and promising progress has already been achieved, issues relating to the structural stability of these electrode materials still remain. Hence, more research work needs to be done to overcome this challenge in order for alloying-typed materials to be widely used as anodes in commercial rechargeable lithium-ion batteries. In fact, since the demonstration by Cui Yi in 2007 that nanostructured Si film can undergo lithiation and delithiation cycling without succumbing to the mechanical stresses resulting from the large volume change, a lot of studies has been carried out on nanostructuring of Si to improve the structural stability of this alloying anode material. Eventually, Amprius, a start-up company in California commercialized LIB which uses Si nanowires as anode in 2014, delivering much higher energy densities of 800 – 1000 W h L^{-1} and 325 – 400 W h kg^{-1} than traditional commercial LIB.

2.3.3 Conversion-Type Anode Materials

The third and last class of anode materials is the conversion-type materials. This class of anode materials include a number of binary compounds, M–X where M is a transition metal such as iron (Fe), cobalt (Co), nickel (Ni) and copper (Cu) and X is an anion like oxide (O^{2-}), sulfide (S^{2-}), fluoride (F^{-}), nitride (N^{3-}) or phosphide (P^{3-}). Equation 2.4 shows a generalized equation for the reaction between these conversion-type anode materials and lithium ions, where M is a transition metal element. As shown in the forward equation, the conversion-type material, MX_y reacts with lithium ions to form metallic M and $Li\frac{y}{z}X$. After delithiation, the compounds are formed back into its initial state, MX_y.

Although transition metals in the 3d block like Fe and Cu are not active towards lithium, the oxides and sulfides of these transition metals are actually able to store lithium ion reversibly. [41, 64] And, the main reason for the reversibility of the conversion reaction appears to be linked to the formation of nanoparticles. After the first lithiation, the fully

$$MX_y + z\,Li^+ + z\,e^- \underset{\text{Discharging}}{\overset{\text{Charging}}{\rightleftharpoons}} M + Li_zX_y$$

$$\text{where } y = z \text{ for } X = F;\ y = \tfrac{z}{2} \text{ for } X = O, S;\ y = \tfrac{z}{3} \text{ for } X = N, P$$

Equation 2.4

reduced product forms a nanocomposite comprising of metallic nanoparticles (usually in the range of 1 – 5 nm) dispersed in a Li_zX_y matrix as depicted in Figure 2.8. This structure can help to prevent the agglomeration of the metal nanoparticles and maintained their large surface area. Due to the large interfacial area between these metal nanoparticles and the Li_zX_y matrix material, when a reverse potential is applied, they can readily decompose the matrix in which they are embedded in, forming back the MX_y binary compound. [7, 41, 65] It has been shown that the size of the metal particles remains in the nanometre regime even after several charging-discharging cycles, giving the conversion-typed anode its good cycling stability. [66]

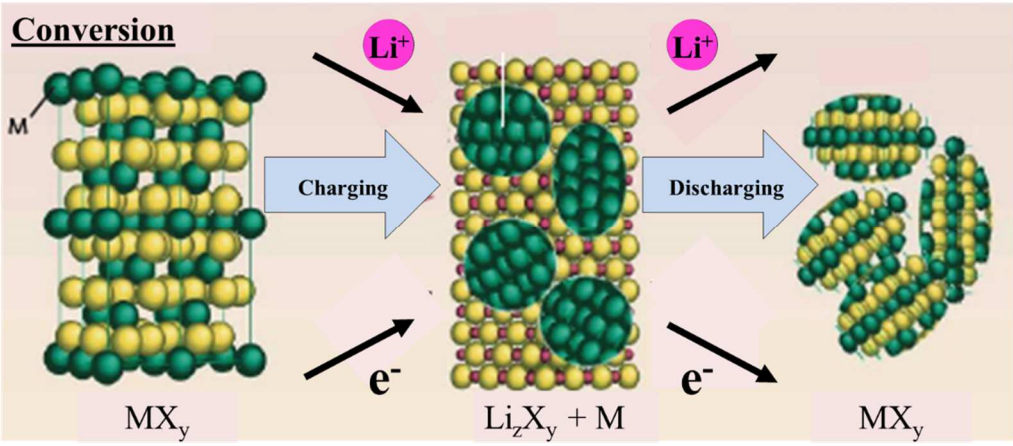

Figure 2.8: Schematic representation showing the conversion reaction. *(Reprinted by permission from Macmillan Publishers Ltd: [67], © 2008)*

Anodes made from these conversion-type materials typically exhibit high capacities that are about 2 – 3 times higher than that of graphite because at least one or more lithium ions are involved in the conversion reaction per transition metal in the formula unit of the anodic material. [68] Unlike graphite where no more than one lithium ion can be inserted into the structural framework for each formula unit of carbon (C_6), cobalt oxide (CoO), a conversion-type anodic material, can accommodate up to two lithium ions per formula unit of CoO. [41] Conversion reactions have been reported for many different transition metal oxides and sulfides, where each material reacts with lithium at a different voltage, usually in the range of 1.2 – 2.5 V *vs.* Li/Li^+. [69-73] This goes to show that the actual potential at which conversion reaction takes place depends on both the type of transition metal and the accompanying anionic species. So, in principle, the reaction potential for the conversion anode can easily be tuned to meet that required by different applications. For a particular metal atom, the lithiation potential is usually observed to decrease from metal fluoride, metal sulfide, metal oxide, and metal nitride to metal phosphide, following the trend in the decrease in the metal-anion (M-X) bond polarization when going from metal fluoride to metal phosphide. However, achieving good and stable cycling performance for conversion-type anode materials remains a challenge. During conversion reaction, the material is subjected to structural reorganization and large volume change. When chromium oxide (Cr_2O_3) undergoes a conversion reaction to form metallic chromium (Cr) and lithium oxide (Li_2O), the material will experience a volume change of about 100%. Although this volume change is much smaller compared to that experience by most alloying-type materials like Si and Sn, it can still lead to pulverization and capacity fading in the anode. Hence, a lot of research work has been carried out to improve the cycling performance of conversion-type anode materials, exploring their potential as anode in next generation commercial LIB.

2.4 Metal Sulfides for Lithium Ion Battery

Metal sulfides are an attractive group of materials for application in lithium and lithium ion batteries because of their ability to “store” lithium ions. Furthermore, metal sulfides are Earth-abundant and low cost as they usually exist as minerals like pyrite FeS_2,

pyrrhotite $Fe_{1-x}S$, molybdenite MoS_2, chalcocite Cu_2S, herzenbergite SnS and berndtite SnS_2 in nature, making it possible to reduce the cost of commercial LIB. [74] Other advantages of metal sulfides for application in LIB include their good electrical conductivity, mechanical properties and thermal stability. [75] Owing to their rich redox chemistry which allows one or more lithium ion per metal atom to be "inserted" into it, metals sulfides generally have specific capacity that is much higher than graphitic carbon, the current material of choice for most commercial LIB. [68]

In the beginning, metal sulfides such as MoS_2 and FeS_2 were used as cathode materials in primary lithium batteries. [76-78] When Whittingham first demonstrated the rapid and reversible intercalation of lithium into layered titanium disulfide (TiS_2) at ambient temperature, this material gained a lot of interest as cathode material for rechargeable lithium batteries [79] Following, a lot of work were carried out on metal sulfides and lithiated metal sulfides like TiS_2, tantalum(IV) sulfide (TaS_2), MoS_2, lithium vanadium sulfide ($LiVS_2$) and lithium chromium sulfide ($LiCrS_2$) which can store lithium ions reversibly via an intercalation reaction. [80] However, research focus was shifted to lithiated metal oxide after it was shown that lithium ions can be reversibly inserted into and extracted from $LiCoO_2$, providing an open circuit voltage that is about twice that of Li_xTiS_2. [11]

$$MoS_2 + x\,Li^+ + x\,e^- \longrightarrow Li_xMoS_2 \qquad (\approx 1.1\,V\ vs.\ Li/Li^+;\ 0 \le x \le 1)$$

$$Li_xMoS_2 + (4-x)\,Li^+ + (4-x)\,e^- \longrightarrow Mo + 2\,Li_2S \qquad (\approx 0.6\,V\ vs.\ Li/Li^+)$$

Equation 2.5

$$In_2S_3 + 6\,Li^+ + 6\,e^- \longrightarrow 2\,In + 3\,Li_2S$$

$$In + x\,Li^+ + x\,e^- \longrightarrow Li_xIn \qquad (0 \le x \le 4.33)$$

Equation 2.6

Since the discovery of a new lithium storage mechanism known as “conversion reaction”, metal sulfides that can store lithium ions reversibly via conversion reaction have regained vast interest as potential electrode material for LIB application. [41] Examples of such materials include transition metal sulfides like iron sulfides, cobalt sulfides and nickel sulfides. [81-85] In fact, most metal sulfides will undergo conversion reaction with lithium ions if the electrode materials are charged or discharged to the required potential for the reaction to occur. [68] MoS_2, for example, will undergo intercalation reaction when in the voltage range of 3.0 V to 1.1 V and, when it is in the voltage range below 1.1 V, conversion reaction will predominate (Equation 2.5). [86, 87] Besides intercalation and conversion reactions, some metal sulfides are able to store lithium ions reversibly via an alloying reaction. Indium sulfide (In_2S_3), for instance, will first undergo a conversion reaction with lithium ions to form a composite made up of indium particles embedded in a Li_2S matrix where the indium can further alloy with more lithium ions to form Li_xIn, as shown in Equation 2.6. [88-90] Other metal sulfides that store lithium ions through a combination of conversion and alloying reaction includes tin sulfides, antimony sulfides and bismuth sulfides. [91-93]

2.4.1 Iron Sulfides

As mentioned in Section 1.2, sulfur has a rich and versatile chemistry where it can form a vast variety of binary metal sulfides. If the metal can adopt more than one oxidation states, various metal sulfide compounds with different metal to sulfur stoichiometric ratio can be formed. Iron, with its possibility to adopt an oxidation state of +2 and +3, can form numerous iron sulfide compounds and some of them are shown in Table 2.3. These materials are of great interest for LIB application because of their various advantages. Firstly, FeS_2, Fe_3S_4 and FeS all have high theoretical specific capacities. Based on Faraday’s Law, the theoretical capacities of FeS_2, Fe_3S_4 and FeS are calculated to be 894 mA h g^{-1} ($FeS_2 + 4\ Li^+ + 4\ e^- \rightarrow Fe + 2\ Li_2S$), 725 mA h g^{-1} ($Fe_3S_4 + 8\ Li^+ + 8\ e^- \rightarrow 3\ Fe + 4\ Li_2S$) and 609 mA h g^{-1} ($FeS + 2\ Li^+ + 2\ e^- \rightarrow Fe + Li_2S$)

respectively [94-97] and all these values are much higher than the theoretical specific capacity of graphitic carbon (372 mA h g^{-1}), the most widely-used anode material for commercial LIB currently. Other attractive features of iron sulfides include their low environmental impact (Fe and S are generally non-toxic elements), abundance (Fe and S are both abundant on Earth) and, most importantly, affordable cost (USD150 for 1 ton of natural pyrite) which makes them suitable for large-scale production. [98-101] However, iron sulfides are not without disadvantages as anode materials for LIB. Sulfur and sulfide electrodes were reported to react with lithium to form lithium polysulfides (Li_2S_x, $1 \leq x \leq 8$) which can dissolve into the liquid electrolyte in the battery cell, thus resulting in a loss of active material, poor capacity retention and cycling performance. [93, 102-104] Furthermore, iron sulfides have discharge voltages that are higher than graphite. Iron pyrite (FeS_2), for example, has a high discharge voltage of about 1.5 V (*vs.* Li/Li^+), which will result in a reduction in the overall working voltage of the full battery cell. However, this high discharge potential also makes pyrite FeS_2 safer from the formation of lithium dendrites during repeated charge-discharge cycling compared to carbon-based and alloying-type anodes which have discharge potentials that are close to that of metallic lithium.

Table 2.3: Various iron sulfide phases and their crystal structure. [105]

Phase	Mineral Name	S:Fe Ratio	Crystal System	Cell Parameters		
				a (Å)	b (Å)	c (Å)
FeS	Troilite	1.00	Hexagonal	5.97	5.97	11.76
$Fe_{1-x}S$	Pyrrhotite	1.00 – 1.25	Hexagonal	6.90	6.90	34.52
Fe_9S_{10}	Pyrrhotite	1.11	Hexagonal	34.49	34.49	23.00
Fe_7S_8	Pyrrhotite	1.14	Hexagonal	6.90	6.90	17.28
Fe_3S_4	Greigite	1.33	Cubic	9.88	9.88	9.88
FeS_2	Pyrite	2.00	Cubic	5.42	5.42	5.42
FeS_2	Marcasite	2.00	Orthorhombic	4.44	5.42	3.39

Iron sulfides exist in the nature as a variety of minerals and play critical roles in the biogeochemical cycle of sulfur. [106, 107] However, natural iron sulfides tend to contain trace metal impurities and these impurities can have negative effects on their properties. Furthermore, the natural iron sulfides obtained from different sources or locations tend to have different amount of impurities, particle and grain size, thus resulting in different lithium storage performance. [108] Therefore, there is a need to shift the focus of the research work from natural to synthetic iron sulfides. In fact, many studies have shown that synthetic iron sulfide like iron pyrite achieves better lithium storage performance than natural iron sulfides. In a report in 1983, Iwakura et al. prepared pyrite FeS_2 via sulfurization of $FeCl_2$ and Fe_2O_3 using H_2S gas and showed that the synthesized pyrite displayed higher and better electrode efficiencies compared to natural pyrite, and such improvement has been attributed to the differences in particle size or specific surface area between the synthesized and natural pyrite. [77] Subsequently, Yang et al. did some study on natural and synthetic pyrite, arriving to the conclusion that, since both samples contain trace impurities, synthetic pyrite has better rate capability than natural pyrite because of its smaller grain size. [108] The work done by Feng et al. also attained similar results, with the synthesized FeS_2 achieving an initial discharge capacity (863 mA h g^{-1}) which is almost 100 mA h g^{-1} higher than that of natural pyrite (≈ 763 mA h g^{-1}). [99] All these reports showed that synthetic pyrite exhibits improved lithium storage performance compared to natural pyrite and this encouraged more research work to be carried out on the synthesis of iron sulfides with good purity and smaller particle or grain size for application in LIB.

Throughout the years, many different approaches have been employed to synthesize pure iron sulfides. Iron sulfide films have been prepared via several methods such as thermal sulfurization of iron or iron oxide film, spray pyrolysis, spark plasma sintering, chemical vapour deposition or chemical vapour transport, electrochemical deposition, magnetron sputtering and molecular beam deposition. [81, 82, 97, 109-127] Other techniques like solid state reaction, mechanical milling and alloying, micelle-assisted synthesis method, hydrothermal, solvothermal and hot injection method have also been used to synthesize iron sulfide particles. [81, 128-143] The lithium storage properties of some of the prepared iron sulfides were examined in the literature and Table 2.4 shows a summary of selected results.

Table 2.4: Tabulation of lithium storage performance of some iron sulfides reported in literature.

Phase	Morphology	Synthesis Method	Cut-off Voltage	Current Density	Initial Capacity (mA h g^{-1})	Capacity (mA h g^{-1}) / Nth Cycle	Ref
Troilite FeS	Nanosheets	Solution-based synthesis	0.01 – 3 V	100 mA g^{-1}	1022	615 / 100th	[82]
	Nanoparticles		0.01 – 3 V	100 mA g^{-1}	1000	580 / 100th	
	Nanoplates		0.01 – 3 V	100 mA g^{-1}	1010	525 / 100th	
	RGO-wrapped nanoparticles	Direct precipitation	0.005 – 3 V	100 mA g^{-1}	1357	1064 / 15th	[144]
Pyrrhotite $Fe_{1-x}S$	Nanoparticles embedded in carbon microspheres	Solvothermal	0.001 – 2.5 V	50 mA g^{-1}	1564	736 / 50th	[145]
Pyrrhotite Fe_7S_8	Fe_7S_8@C nanospheres	Solid-solid reaction	0.01 – 3.00 V	100 mA g^{-1}	~825	~400 / 100th	[146]

Table 2.4: Tabulation of lithium storage performance of some iron sulfides reported in literature. (Continued)

Phase	Morphology	Synthesis Method	Cut-off Voltage	Current Density	Initial Capacity (mA h g^{-1})	Capacity (mA h g^{-1}) / Nth Cycle	Ref
Pyrrhotite Fe_7S_8	Micron-sized particles	Precipitation	0.9 – 2.50 V	66 mA g^{-1}	~800	110 / 50th	[147]
Greigite Fe_3S_4	Nanoplatelets	Colloidal	0 – 3 V	1 mA	110	~55 / 2nd	[148]
	Octahedral microcrystals	Hydrothermal	0.005 – 3 V	100 mA g^{-1}	1161	563 / 100th	[149]
Pyrite FeS_2	Film	Sulfurization of Fe_2O_3 film	1 – 2.5 V	50 µA cm^{-2}	844	291 / 500th	[97]
	Submicron particles	Solid state reaction	1.2 – 2.6 V	89 mA g^{-1}	730	420 / 30th	[135]
	Microspheres	Solvothermal	1.2 – 2.6 V	45 mA g^{-1}	773	387 / 30th	[150]

Table 2.4: Tabulation of lithium storage performance of some iron sulfides reported in literature. (Continued)

Phase	Morphology	Synthesis Method	Cut-off Voltage	Current Density	Initial Capacity (mA h g^{-1})	Capacity (mA h g^{-1}) / Nth Cycle	Ref
Pyrite FeS_2	Microcubes	Solvothermal	1 – 3 V	144 μ A	500	190 / 30th	[151]
	Nanocubes	Solvothermal	0.001 – 3 V	1000 mA g^{-1}	980	540 / 150th	[152]
	Microspheres	Solvothermal	1.0 – 3.0 V	1000 mA g^{-1}	~690	540 / 100th	[153]

Due to it having the highest theoretical specific capacity, FeS_2 has gained the most attention as a potential anode material for commercial LIB amongst the many iron sulfide phases. Huang et al. prepared iron pyrite film through sulfurizing of iron oxide film and achieved a discharge capacity of 844 mA h g^{-1} and 291 mA h g^{-1} for the 1st and 500th cycle when cycled at a current density of 50 µA cm^{-2}. [97] To achieve better lithium storage performance than the iron pyrite film, several groups have attempted to increase the surface area of the active material by reducing its particle size, thus providing more interface for the reactions with lithium ions and result in an improvement in the kinetics of these electrode reactions. By adopting this approach, the pyrite FeS_2 microspheres prepared by Wang and co-workers achieved an initial discharge capacity of 868 mA h g^{-1} when the electrode is discharged from 2.4 V to 1.45 V at a current density of 30 mA g^{-1}. [81] On the other hand, the iron pyrite microspheres synthesized by Zhang et al. delivered an initial discharge capacity of 773 mA h g^{-1} and, after 30 cycles at a current density of 45 mA g^{-1}, they retained a discharge capacity of 387 mA h g^{-1}. [150] Lately, Hu and co-workers prepared nanoplates-assembled pyrite FeS_2 microspheres which achieved a high discharge capacity of about 690 mA h g^{-1} and 540 mA h g^{-1} for the 1st and 100th cycle when cycled between 1.0 V and 3.0 V at a current density of 1 A g^{-1}. [153] Further improvement in lithium storage performance (discharge capacity of 730 mA h g^{-1} and 420 mA h g^{-1} for the 1st and 30th cycle respectively) was attained by Zhang et al. who prepared sub-micron iron pyrite particles (mean particle size ≈ 0.28 µm), which have an even higher surface area than micron-sized particles, using a solid-state method. [135] Pyrite FeS_2 nanocubes have also been shown to deliver good lithium storage performance where an initial discharge capacity of 980 mA h g^{-1} and a discharge capacity of 540 mA h g^{-1} at the 150th cycle was reported by Liu and co-workers. [152]

Another tactic commonly used to increase the surface area of the active materials would be to synthesize particles with distinct morphologies such as nanosheets and nanoflowers, which tend to have high surface area. In view of this, Xu and co-workers investigated the lithium storage properties of troilite FeS nanomaterials with different morphologies, attaining initial discharge capacities of more than 1000 mA h g^{-1} for all three samples. [82] And, after cycling for 100 cycles, the troilite FeS nanosheets, nanoparticles and nanoplates retained a discharge capacity of 615 mA h g^{-1}, 580 mA h g^{-1} and 525 mA h g^{-1} respectively, where the author attributed the enhanced

performance of the troilite FeS nanosheets partly to its higher surface area and ultra-thin thickness which reduces the diffusion pathway of the charge carriers and allows a faster charge transfer.

A third approach used to improve the lithium storage performance of the iron sulfide compounds is by embedding or encapsulating the particles in another material like carbon or polymers. This method has been shown to effectively reduce dissolution into the electrolyte, thereby reducing the loss of active material in the electrode and allow better retention of its lithium storage capacity during cycling. Based on this approach, Fei and co-workers prepared nanocomposite comprising of FeS wrapped with reduced graphene oxide (FeS@rGO) and measured its electrochemical properties. [144] They reported that the FeS@rGO exhibited better lithium storage performance than the bare FeS particles due to several reasons and, amongst them, the most important one would be the absorption and entrapment of the polysulfides (formed from the FeS particles during galvanostatic cycling) by the rGO wrapping layer which reduces the dissolution of polysulfides into the electrolyte. This enabled the FeS@rGO to achieve a high discharge capacity of 1064 mA h g^{-1} at the 15th cycle when cycled at a current density of 100mA g^{-1} in the voltage window of 0.005 – 3 V. This approach was also adopted by Wu and co-workers who prepared iron sulfide ($Fe_{1-x}S$) nanoparticles embedded in carbon microspheres and characterized their lithium storage performance, reporting a high discharge capacity of 736 mA h g^{-1} at the 50th cycle when cycled between 0.001 V and 2.5 V at a current density of 50 mA g^{-1}. [145] The authors attributed this excellent electrochemical performance partly to its carbon nanosheet-wrapped structure, which reduces the direct contact between the $Fe_{1-x}S$ nanoparticles and the electrolyte, thereby making it more difficult for the polysulfides formed during lithiation to dissolve into the electrolyte.

Iron sulfides are very promising as electrode materials for application in LIB and good lithium storage performance have been reported by several research groups. Although many attempts have been made to improve their lithium storage performance by increasing the surface area of these iron sulfide electrode materials through reducing their particle size and by preparing particles with distinct morphologies, there are still problems to be addressed for these electrodes. As with all sulfide electrodes, polysulfides will be formed during its partial reduction and that the dissolution of these

polysulfides into the electrolyte will result in loss of active materials, poor capacity retention and poor cycling performance. [93, 102, 103, 154] To address this problem, iron sulfide particles embedded or encapsulated with another material like carbon or polymers have been prepared and studies have shown that this method is indeed effective in improving their lithium storage performance. However, it should be highlighted that these carbon and polymeric encapsulating materials will reduce the overall theoretical capacity of the electrode material by acting either as a dead weight or an active material with lower theoretical capacity than the iron sulfide compound. In addition, these encapsulating materials also hinder the diffusion of lithium ions into the iron sulfide active material as the lithium ion will have to first diffusion through these encapsulating layers to reach the surface of the iron sulfide particles. To find more effective solution to the problem of polysulfide dissolution and to better improve the lithium storage capability of iron sulfide electrodes, it is important to first understand whether having more sulfide ions in an iron sulfide compound is more beneficial or detrimental to its lithium storage performance and why the iron sulfide compound with one stoichiometry performs better than that with another stoichiometry. Through this understanding, possible ways of improving the lithium storage properties of the metal sulfide electrodes can be proposed. However, to date, no such study which attempt to understand the impact of the amount of sulfide ions in an iron sulfide compound on its polysulfide dissolution problem and lithium storage properties has been reported.

2.4.2 Tin Sulfides

Tin (Sn), being a Group 14 element, can adopt an oxidation state of +2 or +4. This, together with the ability of sulfur (S) to adopt oxidation states in the range of -2 to +6, enables Sn to form various binary compounds with S and the most commonly found tin sulfide compounds are listed in Table 2.5. [155] Amongst the various tin sulfides, tin monosulfide (SnS) and tin disulfide (SnS_2) have been more widely studied as a potential anode material for lithium ion battery (LIB) due to various reasons and the main motivation would be the high theoretical capacity of both SnS and SnS_2. Based on an irreversible reaction of SnS with Li to yield Sn (Equation 5.1) followed by a reversible lithiation and delithiation of Sn to form $Li_{4.4}Sn$ (Equation 5.3), SnS is determined to

have a theoretical reversible lithium storage capacity of 781 mA h g^{-1}. [156, 157] On the other hand, SnS_2 is reported to have a more complicated electrode reaction, though, in general, it involves SnS_2 to undergo an irreversible conversion reaction with Li to form Sn (Equation 5.2) and a subsequent reversible alloying reaction between Sn and Li to form $Li_{4.4}Sn$ (Equation 5.3), thereby yielding a theoretical reversible capacity of 645 mA h g^{-1}. [158-160] All these values are much higher than the theoretical specific capacity of graphitic carbon (372 mA h g^{-1}), the most widely-used anode material for commercial LIB currently. Other attractive features of tin sulfides include their low toxicity, abundance and affordable cost which are very important for large-scale production [161] However, tin sulfides also have several drawbacks as anode materials for LIB. Similar to the iron sulfide (Section 2.4.1) and other sulfur and sulfide electrodes, the problem relating to the dissolution of lithium polysulfides (Li_2S_x, $1 \leq x \leq 8$) is also present, thereby resulting in loss of active material, poor capacity retention and unsatisfactory cycling performance. [93, 102-104] Another disadvantage of tin sulfide electrodes would be the irreversible consumption of a large amount of lithium for the conversion reaction of tin sulfide into Sn during the initial cycle. As a result of this irreversible consumption of Li, more cathodic material needs to be used to ensure enough supply of Li for the subsequent lithiation and delithiation process in a full battery cell.

Table 2.5: Various tin sulfide phases and their crystal structure. [162]

Phase	Mineral Name	Sn:S Ratio	Crystal System	Cell Parameters		
				a (Å)	b (Å)	c (Å)
SnS	Herzenbergite	1	Orthorhombic	4.33	11.19	3.98
Sn_2S_3	Ottemannite	1.50	Orthorhombic	8.86	14.02	3.75
SnS_2	Berndtite	2.00	Hexagonal	3.65	3.65	5.90

Table 2.6: Tabulation of lithium storage performance of some tin sulfides reported in literature.

Phase	Morphology	Synthesis Method	Cut-off Voltage (V)	Current Density	Initial Capacity (mA h g^{-1})	Capacity (mA h g^{-1}) / Nth Cycle	Ref
SnS	Nanoflower	Solution-based synthesis	0.01 – 1.1	50 mA g^{-1}	1050	~500 / 30th	[163]
	Yolk-shell	Gas sulfurization of yolk-shell SnO_2	0.001 – 1	1 A g^{-1}	1487	~672 / 100th	[164]
	Nanorod	Solvothermal	0.01 – 1.2	160 mA g^{-1}	1528	385 / 50th	[165]
	Nanosheet sandwiched between polypyrrole nanosheets	Hydrothermal	0.01 – 3	63 mA g^{-1}	~1800	~1000 / 50th	[166]
SnS_2	Nanosheet	Solvothermal	0 – 1.15	323 mA g^{-1}	~1500	430 / 50th	[167]
	Hexagonal nanoplate	Thermal decomposition	0.001 – 1.1	323 mA g^{-1}	1311	~583 / 30th	[168]

Table 2.6: Tabulation of lithium storage performance of some tin sulfides reported in literature. (Continued)

Phase	Morphology	Synthesis Method	Cut-off Voltage (V)	Current Density	Initial Capacity (mA h g^{-1})	Capacity (mA h g^{-1}) / Nth Cycle	Ref
SnS_2	Nanosheet	Hydrothermal	0.001 – 1.5	100 mA g^{-1}	~1350	163 / 50th	[169]
	SnS_2/graphene nanosheets assembled spheres	Hydrothermal	0.001 – 1.5	100 mA g^{-1}	~1650	920 / 50th	[169]
	Nanoplates decorated on graphene	Gas sulfurization of graphene-support SnO_2 nanoparticles	0.005 – 1.3	50 mA g^{-1}	~1875	~650 / 30th	[159]
	Nanosheet	Solvothermal	0.01 – 1.5	100 mA g^{-1}	2057	437 / 100th	[170]
	Nanoflower	Solvothermal	0.01 – 1.5	100 mA g^{-1}	2169	542 / 100th	[170]

To date, many approaches have been employed to synthesize tin sulfides like SnS and SnS_2 with good purity. Methods such as the sulfurization of metallic Sn film [171-173], spray pyrolysis [174-177] electrochemical deposition [178], chemical vapor deposition [179], thermal evaporation [180-184], sputtering [185] and atomic layer deposition [186] were used to prepare tin sulfide thin films. Tin sulfide particles have also been synthesized via various techniques like mechanical alloying [187, 188], hydrothermal [189-191], solvothermal [192-199], polyol route [200, 201], thermal decomposition [168], sulfurization of tin oxide [159, 164], laser ablation [202] and wet chemical method [163]. Some of the tin sulfides prepared have been studied as potential anode material for LIB application and the lithium storage performance reported in selected literature was tabulated and presented in Table 2.6.

To achieve good lithium storage performance for the SnS electrodes, many research groups have turned into preparing small particles i.e. micron or nano-size with unique morphologies that will (1) yield a high surface area and, hence, provide more interface for the reaction between the active material and the lithium ions and (2) provide voids between the tin sulfide particles so that there will be available spaces to accommodate the large volume expansion during the alloying reaction between Sn and Li. By adopting this approach, the SnS nanorod prepared by Tripathi and co-worker displayed a high initial discharge capacity of 1528 mA h g^{-1} but only a fair cycling performance (discharge capacity of 385 mA h g^{-1} at the 50^{th} cycle) when subjected to galvanostatic cycling at 160 mA h g^{-1}. [165] Vaughn II et al. prepared SnS nanoflowers which are made up of a hierarchical assembly of crystalline SnS nanosheets using a simple solution-based method and reported that these SnS nanoflowers exhibited an initial discharge capacity of 1050 mA h g^{-1}. [163] After cycling for 50 cycles in a voltage window of 0.01 – 1.1 V and at a current density of 50 mA g^{-1}, these nanoflowers retained a discharge capacity of ≈500 mA h g^{-1}. In another report, Choi attempted to synthesize SnS particles with a yolk-shell structure and he showed that these SnS yolk-shell displayed enhanced lithium storage properties, maintaining a high discharge capacity of ≈672 mA h g^{-1} at the 100^{th} cycle when cycled at a high current density of 1 A g^{-1}. The author attributed this superior cycling performance to the porous yolk-shell structure with large void space in between the yolk and the shell, thereby decreases the lithium ion diffusion distance, enables rapid lithium ion diffusion, promotes electrolyte penetration and reduces pulverization of the electrode during repeated lithium insertion

and de-insertion process. [164] Similar approach has also been applied to SnS_2 electrodes, where the hexagonal SnS_2 nanoplates prepared by Seo et al. via thermal decomposition displayed a discharge capacity of 1311 mA h g^{-1} and about 583 mA h g^{-1} at its 1st and 30th cycle respectively when cycled at a current density of 323 mA g^{-1} in the voltage window of 0.001 – 1.1 V. [168] SnS_2 nanosheets and nanoflowers have also been synthesized and examined for their lithium storage properties, where it was reported that both of them exhibit good cycling performance, retaining a discharge capacity of 437 mA g^{-1} and 542 mA g^{-1} at the 100th cycle respectively. [170]

To further improve the lithium storage capability of tin sulfide electrodes, attempts to prepare tin sulfide-graphene composites were made. Graphene, with its high conductivity, can increase the overall electronic conductivity of the tin sulfide-graphene composite. Furthermore, the possible interaction between the delocalized π-electrons in graphene and the S atoms in SnS_2 could promote faster charge transfer during lithiation and delithiation. Thus, tin sulfide-graphene composites should achieve better lithium storage performance than the tin sulfide compound alone. In fact, the SnS_2-graphene hybrids prepared by Luo and co-workers exhibited a high initial discharge capacity of about 1875 mA h g^{-1} and retained a discharge capacity approximately 650 mA h g^{-1} after 30 cycles. [159] SnS_2/graphene nanosheets assembled spheres also displayed good lithium storage capability, achieving a discharge capacity of around 1650 mA h g^{-1} and 920 mA h g^{-1} at its 1st and 50th cycle. [169] Besides graphene, polymers with good electronic conductivity have also been used to form tin sulfide composites with the aim of enhancing their lithium storage properties. By sandwiching a SnS layer in between polypyrrole, a material with good electronic conductivity, to increase the electronic conductivity and lithium ion diffusion kinetics at the electrode, Liu et al. achieved an excellent cycling results for their sandwich-like SnS/polypyrrole nanosheets with an initial discharge capacity of 1800 mA h g^{-1} and a high discharge capacity about 1000 mA h g^{-1} at the 50th cycle. [166]

The good lithium storage performances of tin sulfides that have been reported by several research groups make them are very favourable as potential anode materials for application in commercial LIB. However, there are still some problems to be addressed for these electrodes. As mentioned previously, the formation and dissolution of polysulfides into the electrolyte will result in a loss of active materials, poor capacity

retention and poor cycling performance. [93, 102, 103, 154] Furthermore, the irreversible consumption of a large amount of lithium for the irreversible conversion reaction of tin sulfide with Li during the initial cycle will require the use of more cathodic material in a full battery cell so as to ensure enough supply of Li for the subsequent lithiation and delithiation process. It should be mentioned that a tin sulfide compound with more sulfide content will require more lithium for this irreversible conversion reaction ($SnS + 2\ Li^+ + 2\ e^- \rightarrow Sn + Li_2S$ and $SnS_2 + 4\ Li^+ + 4\ e^- \rightarrow Sn + 2\ Li_2S$) in the first cycle. In order to find effective solutions to the problem of polysulfide dissolution and to better improve the lithium storage capability of tin sulfide electrodes, it is important to first understand the impact of the amount of sulfide ions on the lithium storage performance of a tin sulfide electrode i.e. whether having more sulfide ions in a tin sulfide compound is more beneficial or detrimental to its lithium storage performance and why the tin sulfide compound with one stoichiometry performs better than that with another stoichiometry. Through this understanding, more effective solution can be proposed to address the problem of polysulfide dissolution and to better judge the necessity to use a tin sulfide compound with lesser or more sulfide content for a particular application. However, to date, no such study which attempt to understand the impact of the amount of sulfide ions in a tin sulfide compound on its polysulfide dissolution problem and lithium storage properties has been reported.

References:

1. Linden, D., *Basic Concepts*, in *Handbook of Batteries* D. Linden and T.B. Reddy, Editors. 2002, New York : McGraw-Hill, 2002.

3rd ed. p. 1.1-1.18.

2. Kumar, R.V. and Sarakonsri, T., *Introduction to electrochemical cells*, in *High energy density lithium batteries*. 2010, Wiley-VCH Verlag GmbH & Co. KGaA. p. 1-25.

3. Scrosati, B., *History of lithium batteries.* Journal of Solid State Electrochemistry, 2011. **15**(7-8): p. 1623.

4. *Lithium batteries: from early stages to the future*, in *Lithium batteries*. 2013, John Wiley & Sons, Inc. p. 21-38.
5. Salkind, A.J., Cannone, A.G., and Trumbure, F.A., *Lead-acid batteries*, in *Handbook of batteries*, D. Linden and T.B. Reddy, Editors. 2002, McGraw-Hill: New York. p. 23.1-23.88.
6. Kumar, R.V. and Sarakonsri, T., *A review of materials and chemistry for secondary batteries*, in *High energy density lithium batteries*. 2010, Wiley-VCH Verlag GmbH & Co. KGaA. p. 53-80.
7. Tarascon, J.M. and Armand, M., *Issues and challenges facing rechargeable lithium batteries.* Nature, 2001. **414**(6861): p. 359.
8. Murphy, D.W. and Carides, J.N., *Low voltage behavior of lithium/metal dichalcogenide topochemical cells.* Journal of The Electrochemical Society, 1979. **126**(3): p. 349.
9. Basu, S., *U.S. Patent 4,423,125*. 1983.
10. Scrosati, B., *Lithium rocking chair batteries: an old concept?* Journal of The Electrochemical Society, 1992. **139**(10): p. 2776.
11. Mizushima, K., Jones, P.C., Wiseman, P.J., and Goodenough, J.B., *LixCoO2 ($0<x\leqslant1$): a new cathode material for batteries of high energy density*. Solid State Ionics, 1981. **3**: p. 171.
12. Yazami, R. and Touzain, P., *A reversible graphite-lithium negative electrode for electrochemical generators.* Journal of Power Sources, 1983. **9**(3): p. 365.
13. Yoshino, A., Sanechika, K., and Nakajima, T., *U.S. Patent 4,668,595*. 1987.
14. Nagaura, T. and Tozawa, K., *Progress in batteries and solar cells*. 1990: JEC Press Inc.
15. Patil, A., Patil, V., Shin, D.W., Choi, J.W., Paik, D.S., and Yoon, S.J., *Issue and challenges facing rechargeable thin film lithium batteries.* Materials Research Bulletin, 2008. **43**(8-9): p. 1913.
16. Gasteiger, H., Krischer, K., and Scrosati, B., *Electrochemical cells: basics*, in *Lithium Batteries*. 2013, John Wiley & Sons, Inc. p. 1-19.
17. Broadhead, J. and C., K.H., *Electrochemical principles and reactions*, in *Handbook of batteries*, D. Linden and T.B. Reddy, Editors. 2002, McGraw-Hill: New York p. 2.1-2.37.

18. Mukherjee, R., Krishnan, R., Lu, T.M., and Koratkar, N., *Nanostructured electrodes for high-power lithium ion batteries.* Nano Energy, 2012. **1**(4): p. 518.
19. Goodenough, J.B. and Manivannan, V., *Cathodes for lithium-ion batteries: some comparisons.* Denki Kagaku, 1998. **66**(12): p. 1173.
20. Kim, H.S., Cho, B.W., and Cho, W.I., *Cycling performance of LiFePO4 cathode material for lithium secondary batteries.* Journal of Power Sources, 2004. **132**(1–2): p. 235.
21. Fergus, J.W., *Recent developments in cathode materials for lithium ion batteries.* Journal of Power Sources, 2010. **195**(4): p. 939.
22. Masashi, O. and Itaru, H., *High-rate Li-ion intercalation in nanocrystalline cathode materials for high-power Li-ion batteries*, in *Nanomaterials for Lithium-Ion Batteries*. 2013, Pan Stanford Publishing. p. 227-258.
23. Zheng, J.C., Ou, X., Zhang, B., Shen, C., Zhang, J.F., Ming, L., and Han, Y.D., *Effects of Ni2+ doping on the performances of lithium iron pyrophosphate cathode material.* Journal of Power Sources, 2014. **268**: p. 96.
24. Li, L., Song, S., Zhang, X., Chen, R., Lu, J., Wu, F., and Amine, K., *Ultrasonic-assisted co-precipitation to synthesize lithium-rich cathode Li1.3Ni0.21Mn0.64O2+d materials for lithium-ion batteries.* Journal of Power Sources, 2014. **272**: p. 922.
25. Brousse, T., Lee, S.M., Pasquereau, L., Defives, D., and Schleich, D.M., *Composite negative electrodes for lithium ion cells.* Solid State Ionics, 1998. **113-115**: p. 51.
26. Maranchi, J.P., Hepp, A.F., and Kumta, P.N., *High capacity, reversible silicon thin-film anodes for lithium-ion batteries.* Electrochemical and Solid-State Letters, 2003. **6**(9): p. A198.
27. Chan, C.K., Zhang, X.F., and Cui, Y., *High capacity Li ion battery anodes using Ge nanowires.* Nano Letters, 2007. **8**(1): p. 307.
28. Nishio, K. and Furukawa, N., *Practical batteries*, in *Handbook of battery materials*. 2011, Wiley-VCH Verlag GmbH & Co. KGaA. p. 27-85.
29. Huang, X. and Li, H., *Nanometer anode materials for Li-ion batteries*, in *Nanomaterials for lithium-ion batteries*. 2013, Pan Stanford Publishing. p. 167-197.

30. Zhang, X., Jiang, B., Guo, J., Xie, Y., and Tang, L., *Large and stable reversible lithium-ion storages from mesoporous SnO2 nanosheets with ultralong lifespan over 1000 cycles.* Journal of Power Sources, 2014. **268**: p. 365.
31. Zou, M., Li, J., Wen, W., Chen, L., Guan, L., Lai, H., and Huang, Z., *Silver-incorporated composites of Fe2O3 carbon nanofibers as anodes for high-performance lithium batteries.* Journal of Power Sources, 2014. **270**: p. 468.
32. Xie, Q., Ma, Y., Zhang, X., Wang, L., Yue, G., and Peng, D.L., *ZnO/Ni/C composite hollow microspheres as anode materials for lithium ion batteries.* Journal of Alloys and Compounds, 2014. **619**: p. 235.
33. Kanno, R., Takeda, Y., Ichikawa, T., Nakanishi, K., and Yamamoto, O., *Carbon as negative electrodes in lithium secondary cells.* Journal of Power Sources, 1989. **26**(3-4): p. 535.
34. Mohri, M., Yanagisawa, N., Tajima, Y., Tanaka, H., Mitate, T., Nakajima, S., Yoshida, M., Yoshimoto, Y., Suzuki, T., and Wada, H., *Rechargeable lithium battery based on pyrolytic carbon as a negative electrode.* Journal of Power Sources, 1989. **26**(3-4): p. 545.
35. Liu, C., Li, F., Ma, L.P., and Cheng, H.M., *Advanced materials for energy storage.* Advanced Materials, 2010. **22**(8): p. E28.
36. Choi, D., Wang, W., and Yang, Z., *Material challenges and perspectives*, in *Lithium-ion batteries*. 2011, CRC Press. p. 1-50.
37. L., A. *UN agency bans lithium-ion batteries on passenger aircraft*. 2016 23 Feb 2016 [cited 2016; Available from: http://www.channelnewsasia.com/news/world/un-agency-bans-lithium/2539264.html.
38. Fauteux, D. and Koksbang, R., *Rechargeable lithium battery anodes - alternatives to metallic lithium.* Journal of Applied Electrochemistry, 1993. **23**(1): p. 1.
39. Mao, O. and Dahn, J.R., *Mechanically alloyed Sn-Fe(-C) powders as anode materials for Li-ion batteries - II. The SnFe system.* Journal of the Electrochemical Society, 1999. **146**(2): p. 414.
40. Liu, J., Li, Y., Fan, H., Zhu, Z., Jiang, J., Ding, R., Hu, Y., and Huang, X., *Iron oxide-based nanotube arrays derived from sacrificial template-accelerated hydrolysis: large-area design and reversible lithium storage.* Chemistry of Materials, 2010. **22**(1): p. 212.

41. Poizot, P., Laruelle, S., Grugeon, S., Dupont, L., and Tarascon, J.M., *Nano-sized transition-metal oxides as negative-electrode materials for lithium-ion batteries.* Nature, 2000. **407**(6803): p. 496.
42. Montoro, L.A. and Rosolen, J.M., *Gelatin/DMSO: a new approach to enhancing the performance of a pyrite electrode in a lithium battery.* Solid State Ionics, 2003. **159**(3-4): p. 233.
43. Flandrois, S. and Simon, B., *Carbon materials for lithium-ion rechargeable batteries.* Carbon, 1999. **37**(2): p. 165.
44. Amatucci, G.G. and Pereira, N., *Fluoride based electrode materials for advanced energy storage devices.* Journal of Fluorine Chemistry, 2007. **128**(4): p. 243.
45. Yue, Q. and Harris, S.J., *In situ observation of strains during lithiation of a graphite electrode.* Journal of the Electrochemical Society, 2010. **157**(6): p. A741.
46. Ohzuku, T., Ueda, A., and Yamamoto, N., *Zero-strain insertion material of Li[Li1/3Ti5/3Ti5/3]O4 for rechargeable lithium cells.* Journal of the Electrochemical Society, 1995. **142**(5): p. 1431.
47. Panero, S., Satolli, D., Salomon, M., and Scrosati, B., *A new type of lithium-ion cell based on the Li4Ti5O12/Li2Co0.4Fe0.4Mn3.2O8 high-voltage, electrode combination.* Electrochemistry Communications, 2000. **2**(11): p. 810.
48. Ohzuku, T. and Makimura, Y., *Layered lithium insertion material of LiNi1/2Mn1/2O2: a possible alternative to LiCoO2 for advanced lithium-ion batteries.* Chemistry Letters, 2001. **30**(8): p. 744.
49. Reale, P., Panero, S., Scrosati, B., Garche, J., Wohlfahrt-Mehrens, M., and Wachtler, M., *A safe, low-cost, and sustainable lithium-ion polymer battery.* Journal of The Electrochemical Society, 2004. **151**(12): p. A2138.
50. Chen, Z., Belharouak, I., Sun, Y.K., and Amine, K., *Li4Ti5O12 for high-power, long-life, and safe lithium-ion batteries*, in *Lithium batteries*. 2013, John Wiley & Sons, Inc. p. 277-290.
51. Guo, Y.G., Hu, Y.S., and Maier, J., *Synthesis of hierarchically mesoporous anatase spheres and their application in lithium batteries.* Chemical Communications, 2006(26): p. 2783.

52. Guo, Y.G., Hu, Y.S., Sigle, W., and Maier, J., *Superior electrode performance of nanostructured mesoporous TiO2 (anatase) through efficient hierarchical mixed conducting networks.* Advanced Materials, 2007. **19**(16): p. 2087.
53. Saravanan, K., Ananthanarayanan, K., and Balaya, P., *Mesoporous TiO2 with high packing density for superior lithium storage.* Energy and Environmental Science, 2010. **3**(7): p. 939.
54. Sleigh, A.K. and McKinnon, W.R., *Structure and electrochemistry of LixWO2.* Solid State Ionics, 1991. **45**(1-2): p. 67.
55. Dey, A.N., *Electrochemical alloying of lithium in organic electrolytes.* Journal of The Electrochemical Society, 1971. **118**(10): p. 1547.
56. Besenhard, J.O. and Fritz, H.P., *Reversible electrochemical alloys of metals of main groups - 5 in organic Li+ solutions.* Electrochimica Acta, 1975. **20**(6-7): p. 513.
57. Rao, B.M.L., Francis, R.W., and Christopher, H.A., *Lithium-aluminum electrode.* Journal of the Electrochemical Society, 1977. **124**(10): p. 1490.
58. Besenhard, J.O., *Cycling behavior and corrosion of Li-Al electrodes in organic electrolytes.* Journal of Electroanalytical Chemistry, 1978. **94**(1): p. 77.
59. Aifantis, K.E., *Next-generation anodes for secondary Li-ion batteries*, in *High energy density lithium batteries*. 2010, Wiley-VCH Verlag GmbH & Co. KGaA. p. 129-164.
60. Kiyotaka, Y., *Alloy electrode and its breakthrough technology*, in *Nanomaterials for lithium-ion batteries*. 2013, Pan Stanford Publishing. p. 139-165.
61. Yang, J., Winter, M., and Besenhard, J.O., *Small particle size multiphase Li-alloy anodes for lithium-ion-batteries.* Solid State Ionics, 1996. **90**(1-4): p. 281.
62. Beaulieu, L.Y., Eberman, K.W., Turner, R.L., Krause, L.J., and Dahn, J.R., *Colossal reversible volume changes in lithium alloys.* Electrochemical and Solid State Letters, 2001. **4**(9): p. A137.
63. Scrosati, B. and Garche, J., *Lithium batteries: status, prospects and future.* Journal of Power Sources, 2010. **195**(9): p. 2419.
64. Cabana, J., Monconduit, L., Larcher, D., and Rosa Palacin, M., *Beyond intercalation-based Li-ion batteries: the state of the art and challenges of electrode materials reacting through conversion reactions.* Advanced Materials, 2010. **22**(35): p. E170.

65. Li, H., Richter, G., and Maier, J., *Reversible formation and decomposition of LiF clusters using transition metal fluorides as precursors and their application in rechargeable Li batteries.* Advanced Materials, 2003. **15**(9): p. 736.
66. Grugeon, S., Laruelle, S., Dupont, L., and Tarascon, J.M., *An update on the reactivity of nanoparticles co-based compounds towards Li.* Solid State Sciences, 2003. **5**(6): p. 895.
67. Armand, M. and Tarascon, J.M., *Building better batteries.* Nature, 2008. **451**(7179): p. 652.
68. C., F.M., D., H., and L, Y.A., *Beyond intercalation: nanoscale-enabled conversion anode materials for lithium-ion batteries*, in *Nanotechnology for lithium-ion batteries*, Y.A. L. and I. D., Editors. 2013, Springer US: Boston, MA. p. 85 - 116.
69. Thackeray, M.M. and Coetzer, J., *A preliminary investigation of the electrochemical performance of α-Fe2O3 and Fe3O4 cathodes in high-temperature cells.* Materials Research Bulletin, 1981. **16**(5): p. 591.
70. Thackeray, M.M., Baker, S.D., Adendorff, K.T., and Goodenough, J.B., *Lithium insertion into Co3O4: a preliminary investigation.* Solid State Ionics, 1985. **17**(2): p. 175.
71. Idota, Y., Kubota, T., Matsufuji, A., Maekawa, Y., and Miyasaka, T., *Tin-based amorphous oxide: a high-capacity lithium-ion-storage material.* Science, 1997. **276**(5317): p. 1395.
72. Larcher, D., Masquelier, C., Bonnin, D., Chabre, Y., Masson, V., Leriche, J.B., and Tarascon, J.M., *Effect of particle size on lithium intercalation into α-Fe2O3.* Journal of the Electrochemical Society, 2003. **150**(1): p. A133.
73. Mukaibo, H., Yoshizawa, A., Momma, T., and Osaka, T., *Particle size and performance of SnS2 anodes for rechargeable lithium batteries.* Journal of Power Sources, 2003. **119-121**: p. 60.
74. Lai, C.H., Lu, M.Y., and Chen, L.J., *Metal sulfide nanostructures: synthesis, properties and applications in energy conversion and storage.* Journal of Materials Chemistry, 2012. **22**(1): p. 19.
75. Rui, X., Tan, H., and Yan, Q., *Nanostructured metal sulfides for energy storage.* Nanoscale, 2014. **6**(17): p. 9889.
76. Blomgren, G.E. *Lithium batteries at Energizer*. in *Proceedings of the Annual Battery Conference on Applications and Advances*. 1998.

77. Iwakura, C., Isobe, N., and Tamura, H., *Preparation of iron disulfide and its use for lithium batteries.* Electrochimica Acta, 1983. **28**(3): p. 269.

78. Jacobson, A.J., Chianelli, R.R., and Whittingham, M.S., *Amorphous molybdenum-disulfide cathodes.* Journal of the Electrochemical Society, 1979. **126**(12): p. 2277.

79. Whittingham, M.S., *Electrical energy storage and intercalation chemistry.* Science, 1976. **192**(4244): p. 1126.

80. *Lithium batteries and cathode materials.* Chemical Reviews, 2004. **104**(10): p. 4271.

81. Wang, D.W., Wu, M.H., Wang, Q.H., Wang, T.M., and Chen, J.A., *Controlled growth of uniform nanoflakes-built pyrite FeS2 microspheres and their electrochemical properties.* Ionics, 2011. **17**(2): p. 163.

82. Xu, C., Zeng, Y., Rui, X., Xiao, N., Zhu, J., Zhang, W., Chen, J., Liu, W., Tan, H., Hng, H.H., and Yan, Q., *Controlled soft-template synthesis of ultrathin C@FeS nanosheets with high-Li-storage performance.* Acs Nano, 2012. **6**(6): p. 4713.

83. Wang, Q., Jiao, L., Han, Y., Du, H., Peng, W., Huan, Q., Song, D., Si, Y., Wang, Y., and Yuan, H., *CoS2 hollow spheres: fabrication and their application in lithium-ion batteries.* Journal of Physical Chemistry C, 2011. **115**(16): p. 8300.

84. Shi, W., Zhu, J., Rui, X., Cao, X., Chen, C., Zhang, H., Hng, H.H., and Yan, Q., *Controlled synthesis of carbon-coated cobalt sulfide nanostructures in oil phase with enhanced Li storage performances.* Acs Applied Materials & Interfaces, 2012. **4**(6): p. 2999.

85. Han, S.C., Kim, H.S., Song, M.S., Lee, P.S., Lee, J.Y., and Ahn, H.J., *Electrochemical properties of NiS as a cathode material for rechargeable lithium batteries prepared by mechanical alloying.* Journal of Alloys and Compounds, 2003. **349**(1-2): p. 290.

86. Du, G., Guo, Z., Wang, S., Zeng, R., Chen, Z., and Liu, H., *Superior stability and high capacity of restacked molybdenum disulfide as anode material for lithium ion batteries.* Chemical Communications, 2010. **46**(7): p. 1106.

87. Xiao, J., Wang, X., Yang, X.Q., Xun, S., Liu, G., Koech, P.K., Liu, J., and Lemmon, J.P., *Electrochemically induced high capacity displacement reaction of PEO/MoS2/graphene nanocomposites with lithium.* Advanced Functional Materials, 2011. **21**(15): p. 2840.

88. Ho, W.H., Li, C.F., Liu, H.C., and Yen, S.K., *Electrochemical performance of In2O3 thin film electrode in lithium cell.* Journal of Power Sources, 2008. **175**(2): p. 897.

89. Ye, F., Wang, C., Du, G., Chen, X., Zhong, Y., and Jiang, J.Z., *Large-scale synthesis of In2S3 nanosheets and their rechargeable lithium-ion battery.* Journal of Materials Chemistry, 2011. **21**(43): p. 17063.

90. Liu, Y., Xu, H.Y., and Qian, Y.T., *Double-source approach to In2S3 single crystallites and their electrochemical properties.* Crystal Growth & Design, 2006. **6**(6): p. 1304.

91. Du, N., Wu, X., Zhai, C., Zhang, H., and Yang, D., *Large-scale synthesis and application of SnS2-graphene nanocomposites as anode materials for lithium-ion batteries with enhanced cyclic performance and reversible capacity.* Journal of Alloys and Compounds, 2013. **580**: p. 457.

92. Prikhodchenko, P.V., Gun, J., Sladkevich, S., Mikhaylov, A.A., Lev, O., Tay, Y.Y., Batabyal, S.K., and Yu, D.Y.W., *Conversion of hydroperoxoantimonate coated graphenes to Sb2S3@graphene for a superior lithium battery anode.* Chemistry of Materials, 2012. **24**(24): p. 4750.

93. Jung, H., Park, C.M., and Sohn, H.J., *Bismuth sulfide and its carbon nanocomposite for rechargeable lithium-ion batteries.* Electrochimica Acta, 2011. **56**(5): p. 2135.

94. Kim, Y. and Goodenough, J.B., *Lithium insertion into transition-metal monosulfides: tuning the position of the metal 4s band.* Journal of Physical Chemistry C, 2008. **112**(38): p. 15060.

95. Apostolova, R.D., Kolomoets, O.V., and Shembel, E.M., *Electrolytic iron sulfides for thin-layer lithium-ion batteries.* Russian Journal of Applied Chemistry, 2009. **82**(11): p. 1939.

96. Yamaguchi, Y., Takeuchi, T., Sakaebe, H., Kageyama, H., Senoh, H., Sakai, T., and Tatsumi, K., *Ab initio simulations of Li/Pyrite- MS2 (M=Fe, Ni) battery cells.* Journal of the Electrochemical Society, 2010. **157**(6): p. A630.

97. Huang, S., Liu, X., Li, Q., and Chen, J., *Pyrite film synthesized for lithium-ion batteries.* Journal of Alloys and Compounds, 2009. **472**(1-2): p. L9.

98. Choi, J.W., Cheruvally, G., Ahn, H.J., Kim, K.W., and Ahn, J.H., *Electrochemical characteristics of room temperature Li/FeS2 batteries with*

natural pyrite cathode. Journal of Power Sources, 2006. **163**(1 SPEC. ISS.): p. 158.

99. Feng, X., He, X.M., Pu, W.H., Jiang, C.Y., and Wan, C.R., *Hydrothermal synthesis of FeS2 for lithium batteries.* Ionics, 2007. **13**(5): p. 375.
100. Izatt, R.M., Izatt, S.R., Bruening, R.L., Izatt, N.E., and Moyer, B.A., *Challenges to achievement of metal sustainability in our high-tech society.* Chemical Society Reviews, 2014. **43**(8): p. 2451.
101. Ltd, G.B.C.C. *High quality pyrite*. 2009 9 Dec 2014]; Available from: http://www.alibaba.com/product-detail/High-Quality-Pyrite_2004141976.html.
102. Yamin, H. and Peled, E., *Electrochemistry of a nonaqueous lithium/sulfur cell.* Journal of Power Sources, 1983. **9**(3): p. 281.
103. Yamin, H., Gorenshtein, A., Penciner, J., Sternberg, Y., and Peled, E., *Lithium sulfur battery - oxidation/reduction mechanisms of polysulfides in THF solutions.* Journal of the Electrochemical Society, 1988. **135**(5): p. 1045.
104. Su, Y.S., Fu, Y., Cochell, T., and Manthiram, A., *A strategic approach to recharging lithium-sulphur batteries for long cycle life.* Nat Commun, 2013. **4**.
105. Morimoto, N., Gyobu, A., Mukaiyama, H., and Izawa, E., *Crystallography and stability of pyrrhotites.* Economic Geology, 1975. **70**(4): p. 824.
106. Billon, G., Ouddane, B., Laureyns, J., and Boughriet, A., *Chemistry of metal sulfides in anoxic sediments.* Physical Chemistry Chemical Physics, 2001. **3**(17): p. 3586.
107. Rickard, D. and Luther, G.W., *Chemistry of iron sulfides.* Chemical Reviews, 2007. **107**(2): p. 514.
108. Yang, S.H. and Quinn, C.H., *Chemical, structural and electrochemical comparison of natural and synthetic FeS2 pyrite in lithium cells.* Electrochimica Acta, 2001. **46**(17): p. 2613.
109. Ennaoui, A., Fiechter, S., Goslowsky, H., and Tributsch, H., *Photoactive synthetic polycrystalline pyrite (FeS2).* Journal of the Electrochemical Society, 1985. **132**(7): p. 1579.
110. Smestad, G., Dasilva, A., Tributsch, H., Fiechter, S., Kunst, M., Meziani, N., and Birkholz, M., *Formation of semiconducting iron pyrite by spray pyrolysis.* Solar Energy Materials, 1989. **18**(5): p. 299.

111. Smestad, G., Ennaoui, A., Fiechter, S., Tributsch, H., Hofmann, W.K., Birkholz, M., and Kautek, W., *Photoactive thin-film semiconducting iron pyrite prepared by sulfurization of iron-oxides.* Solar Energy Materials, 1990. **20**(3): p. 149.

112. Blenk, O., Bucher, E., and Willeke, G., *P-type conduction in pyrite single crystals prepared by chemical vapor transport.* Applied Physics Letters, 1993. **62**(17): p. 2093.

113. Lichtenberger, D., Ellmer, K., Schieck, R., Fiechter, S., and Tributsch, H., *Structural, optical and electrical-properties of polycrystalline iron pyrite layers deposited by reactive dc magnetron sputtering.* Thin Solid Films, 1994. **246**(1-2): p. 6.

114. Thomas, B., Ellmer, K., Muller, M., Hopfner, C., Fiechter, S., and Tributsch, H., *Structural and photoelectrical properties of FeS2 (pyrite) thin films grown by MOCVD.* Journal of Crystal Growth, 1997. **170**(1-4): p. 808.

115. Bronold, M., Kubala, S., Pettenkofer, C., and Jaegermann, W., *Thin pyrite (FeS2) films by molecular beam deposition.* Thin Solid Films, 1997. **304**(1-2): p. 178.

116. Raturi, A.K., Ndjeli, L., and Rabah, K., *FeS2 thin films prepared by spray pyrolysis.* Renewable Energy, 1997. **11**(2): p. 191.

117. Jiang, J.Z., Larsen, R.K., Lin, R., Mørup, S., Chorkendorff, I., Nielsen, K., Hansen, K., and West, K., *Mechanochemical synthesis of Fe-S materials.* Journal of Solid State Chemistry, 1998. **138**(1): p. 114.

118. Thomas, B., Cibik, T., Höpfner, C., Diesner, K., Ehlers, G., Fiechter, S., and Ellmer, K., *Formation of secondary iron-sulphur phases during the growth of polycrystalline iron pyrite (FeS2) thin films by MOCVD.* Journal of Materials Science: Materials in Electronics, 1998. **9**(1): p. 61.

119. Meng, L. and Liu, M.S., *Thin pyrite (FeS2) films prepared by thermal-sulfurating iron films at various temperatures.* Materials Science and Engineering B: Solid-State Materials for Advanced Technology, 1999. **60**(3): p. 168.

120. Oertel, J., Ellmer, K., Bohne, W., Röhrich, J., and Tributsch, H., *Growth of n-type polycrystalline pyrite (FeS2) films by metalorganic chemical vapour deposition and their electrical characterization.* Journal of Crystal Growth, 1999. **198-199**(pt 2): p. 1205.

121. Raturi, A.K., Waita, S., Aduda, B., and Nyangonda, T., *Photoactive iron pyrite films for photoelectrochemical (PEC) cells.* Renewable Energy, 2000. **20**(1): p. 37.

122. Nakamura, S. and Yamamoto, A., *Electrodeposition of pyrite(FeS2) thin films for photovoltaic cells.* Solar Energy Materials and Solar Cells, 2001. **65**(1): p. 79.

123. Meng, L., Liu, Y.H., and Huang, W., *Synthesis of pyrite thin films obtained by thermal-sulfurating iron films at different sulfur atmosphere pressure.* Materials Science and Engineering B: Solid-State Materials for Advanced Technology, 2002. **90**(1-2): p. 84.

124. Hamdadou, N., Khelil, A., and Bernède, J.C., *Pyrite FeS2 films obtained by sulphuration of iron pre-deposited films.* Materials Chemistry and Physics, 2003. **78**(3): p. 591.

125. Yamamoto, A., Nakamura, M., Seki, A., Li, E.L., Hashimoto, A., and Nakamura, S., *Pyrite (FeS2) thin films prepared by spray method using FeSO4 and (NH4)2Sx.* Solar Energy Materials and Solar Cells, 2003. **75**(3-4): p. 451.

126. Takeuchi, T., Kageyama, H., Nakanishi, K., Inada, Y., Katayama, M., Ohta, T., Senoh, H., Sakaebe, H., Sakai, T., Tatsumi, K., and Kobayashi, H., *Improvement of cycle capability of FeS2 positive electrode by forming composites with Li2S for ambient temperature lithium batteries.* Journal of The Electrochemical Society, 2011. **159**(2): p. A75.

127. Wang, D.W., Wang, Q.H., and Wang, T.M., *Controlled growth of pyrite FeS2 crystallites by a facile surfactant-assisted solvothermal method.* CrystEngComm, 2010. **12**(3): p. 755.

128. Kar, S. and Chaudhuri, S., *Solvothermal synthesis of nanocrystalline FeS2 with different morphologies.* Chemical Physics Letters, 2004. **398**(1-3): p. 22.

129. Wu, R., Zheng, Y.F., Zhang, X.G., Sun, Y.F., Xu, J.B., and Jian, J.K., *Hydrothermal synthesis and crystal structure of pyrite.* Journal of Crystal Growth, 2004. **266**(4): p. 523.

130. Kim, B.C., Takada, K., Ohta, N., Seino, Y., Zhang, L.Q., Wada, H., and Sasaki, T., *All solid state Li-ion secondary battery with FeS anode.* Solid State Ionics, 2005. **176**(31-34): p. 2383.

131. Chin, P.P., Ding, J., Yi, J.B., and Liu, B.H., *Synthesis of FeS2 and FeS nanoparticles by high-energy mechanical milling and mechanochemical processing.* Journal of Alloys and Compounds, 2005. **390**(1-2): p. 255.

132. Dai, Z., Liu, S., Bao, J., and Jui, H., *Nanostructured FeS as a mimic peroxidase for biocatalysis and biosensing.* Chemistry-a European Journal, 2009. **15**(17): p. 4321.

133. Zhang, Z.J. and Chen, X.Y., *Magnetic greigite (Fe3S4) nanomaterials: shape-controlled solvothermal synthesis and their calcination conversion into hematite (alpha-Fe2O3) nanomaterials.* Journal of Alloys and Compounds, 2009. **488**(1): p. 339.

134. Wang, D., Wang, Q., and Wang, T., *Shape controlled growth of pyrite FeS2 crystallites via a polymer-assisted hydrothermal route.* CrystEngComm, 2010. **12**(11): p. 3797.

135. Zhang, D., Tu, J.P., Xiang, J.Y., Qiao, Y.Q., Xia, X.H., Wang, X.L., and Gu, C.D., *Influence of particle size on electrochemical performances of pyrite FeS2 for Li-ion batteries.* Electrochimica Acta, 2011. **56**(27): p. 9980.

136. Bi, Y., Yuan, Y., Exstrom, C.L., Darveau, S.A., and Huang, J., *Air stable, photosensitive, phase pure iron pyrite nanocrystal thin films for photovoltaic application.* Nano Letters, 2011. **11**(11): p. 4953.

137. Puthussery, J., Seefeld, S., Berry, N., Gibbs, M., and Law, M., *Colloidal iron pyrite (FeS2) nanocrystal inks for thin-film photovoltaics.* Journal of the American Chemical Society, 2011. **133**(4): p. 716.

138. Yuan, B., Luan, W., and Tu, S.T., *One-step synthesis of cubic FeS2 and flower-like FeSe2 particles by a solvothermal reduction process.* Dalton Transactions, 2012. **41**(3): p. 772.

139. Zhang, D., Wang, X.L., Mai, Y.J., Xia, X.H., Gu, C.D., and Tu, J.P., *Enhanced electrochemical performance of FeS2 synthesized by hydrothermal method for lithium ion batteries.* Journal of Applied Electrochemistry, 2012. **42**(4): p. 263.

140. Kirkeminde, A., Scott, R., and Ren, S., *All inorganic iron pyrite nano-heterojunction solar cells.* Nanoscale, 2012. **4**(24): p. 7649.

141. Dutta, A.K., Maji, S.K., Srivastava, D.N., Mondal, A., Biswas, P., Paul, P., and Adhikary, B., *Synthesis of FeS and FeSe nanoparticles from a single source precursor: a study of their photocatalytic activity, peroxidase-like behavior,*

and electrochemical sensing of H2O2. Acs Applied Materials & Interfaces, 2012. **4**(4): p. 1919.

142. Sines, I.T., Vaughn Ii, D.D., Misra, R., Popczun, E.J., and Schaak, R.E., *Synthesis of tetragonal mackinawite-type FeS nanosheets by solvothermal crystallization.* Journal of Solid State Chemistry, 2012. **196**: p. 17.
143. Liu, L., Yuan, Z.Z., Qiu, C.X., and Liu, J.C., *A novel FeS2/CNT micro-spherical cathode material with enhanced electrochemical characteristics for lithium-ion batteries.* Solid State Ionics, 2013. **241**: p. 25.
144. Fei, L., Lin, Q., Yuan, B., Chen, G., Xie, P., Li, Y., Xu, Y., Deng, S., Smirnov, S., and Luo, H., *Reduced graphene oxide wrapped FeS nanocomposite for lithium-ion battery anode with improved performance.* Acs Applied Materials & Interfaces, 2013. **5**(11): p. 5330.
145. Wu, B., Song, H., Zhou, J., and Chen, X., *Iron sulfide-embedded carbon microsphere anode material with high-rate performance for lithium-ion batteries.* Chemical Communications, 2011. **47**(30): p. 8653.
146. Zhang, K., Zhang, T., Liang, J., Zhu, Y., Lin, N., and Qian, Y., *A potential pyrrhotite (Fe7S8) anode material for lithium storage.* RSC Advances, 2015. **5**(19): p. 14828.
147. Zheng, X., *Electrochemical characteristics of pyrrhotine as anode material for lithium-ion batteries.* Journal of Alloys and Compounds, 2016. **661**: p. 483.
148. Paolella, A., George, C., Povia, M., Zhang, Y., Krahne, R., Gich, M., Genovese, A., Falqui, A., Longobardi, M., Guardia, P., Pellegrino, T., and Manna, L., *Charge transport and electrochemical properties of colloidal greigite (Fe3S4) nanoplatelets.* Chemistry of Materials, 2011. **23**(16): p. 3762.
149. Li, G., Zhang, B., Yu, F., Novakova, A.A., Krivenkov, M.S., Kiseleva, T.Y., Chang, L., Rao, J., Polyakov, A.O., Blake, G.R., De Groot, R.A., and Palstra, T.T.M., *High-purity Fe3S4 greigite microcrystals for magnetic and electrochemical performance.* Chemistry of Materials, 2014. **26**(20): p. 5821.
150. Zhang, D., Wu, G., Xiang, J., Jin, J., Cai, Y., and Li, G., *Synthesis and electrochemical performance of bud-like FeS2 microspheres as anode materials for rechargeable lithium batteries.* Materials Science and Engineering B: Solid-State Materials for Advanced Technology, 2013. **178**(8): p. 483.

151. Yersak, T.A., Macpherson, H.A., Kim, S.C., Le, V.D., Kang, C.S., Son, S.B., Kim, Y.H., Trevey, J.E., Oh, K.H., Stol dt, C., and Lee, S.H., *Solid state enabled reversible four electron storage.* Advanced Energy Materials, 2013. **3**(1): p. 120.

152. Liu, W.L., Rui, X.H., Tan, H.T., Xu, C., Yan, Q.Y., and Hng, H.H., *Solvothermal synthesis of pyrite FeS2 nanocubes and their superior high rate lithium storage properties.* RSC Advances, 2014. **4**(90): p. 48770.

153. Hu, Z., Zhang, K., Zhu, Z., Tao, Z., and Chen, J., *FeS2 microspheres with an ether-based electrolyte for high-performance rechargeable lithium batteries.* Journal of Materials Chemistry A, 2015. **3**(24): p. 12898.

154. Rauh, R.D., Shuker, F.S., Marston, J.M., and Brummer, S.B., *Formation of lithium polysulfides in aprotic media.* Journal of Inorganic and Nuclear Chemistry, 1977. **39**(10): p. 1761.

155. B., M., *Chalcogens and metal chalcogenides*, in *Electrochemistry of metal chalcogenides*, F. S., Editor. 2010, Springer Berlin Heidelberg. p. 1-56.

156. Huggins, R.A., *Lithium alloy negative electrodes.* Journal of Power Sources, 1999. **81–82**: p. 13.

157. Robert, F., Lippens, P.E., Olivier-Fourcade, J., Jumas, J.C., and Morcrette, M., *Mössbauer spectroscopy as an efficient tool to study Li insertion mechanisms in negative electrodes for Li ion batteries.* Journal of Power Sources, 2005. **146**(1–2): p. 492.

158. Julien, C. and Pérez-Vicente, C., *Vibrational studies of lithium-intercalated SnS2.* Solid State Ionics, 1996. **89**(3–4): p. 337.

159. Luo, B., Fang, Y., Wang, B., Zhou, J., Song, H., and Zhi, L., *Two dimensional graphene-SnS2 hybrids with superior rate capability for lithium ion storage.* Energy & Environmental Science, 2012. **5**(1): p. 5226.

160. Ji, L., Xin, H.L., Kuykendall, T.R., Wu, S.L., Zheng, H., Rao, M., Cairns, E.J., Battaglia, V., and Zhang, Y., *SnS2 nanoparticle loaded graphene nanocomposites for superior energy storage.* Physical Chemistry Chemical Physics, 2012. **14**(19): p. 6981.

161. Ricardo, A., Pedro, L., Carlos, P.V., and José, L.T., *Anode materials for lithium-ion batteries*, in *Lithium-ion batteries*. 2011, CRC Press. p. 97-146.

162. Mosburg, S., Ross, D.R., Bethke, P.M., and Toulmin, P., *X-ray powder data for herzenbergite, teallite and tin trisulfide.* U.S. Geol. Surv. Prof. Paper, 1961. **424C**: p. 347.

163. Vaughn, D.D., Hentz, O.D., Chen, S., Wang, D., and Schaak, R.E., *Formation of SnS nanoflowers for lithium ion batteries.* Chemical Communications, 2012. **48**(45): p. 5608.

164. Choi, S.H. and Kang, Y.C., *Synthesis for yolk-shell-structured metal sulfide powders with excellent electrochemical performances for lithium-ion batteries.* Small, 2014. **10**(3): p. 474.

165. Tripathi, A.M. and Mitra, S., *Tin sulfide (SnS) nanorods: structural, optical and lithium storage property study.* RSC Advances, 2014. **4**(20): p. 10358.

166. Liu, J., Gu, M., Ouyang, L., Wang, H., Yang, L., and Zhu, M., *Sandwich-like SnS/polypyrrole ultrathin nanosheets as high-performance anode materials for Li-ion batteries.* ACS Applied Materials & Interfaces, 2016. **8**(13): p. 8502.

167. Kim, T.J., Kim, C., Son, D., Choi, M., and Park, B., *Novel SnS2-nanosheet anodes for lithium-ion batteries.* Journal of Power Sources, 2007. **167**(2): p. 529.

168. Seo, J.W., Jang, J.T., Park, S.W., Kim, C., Park, B., and Cheon, J., *Two-dimensional SnS2 nanoplates with extraordinary high discharge capacity for lithium ion batteries.* Advanced Materials, 2008. **20**(22): p. 4269.

169. Chang, K., Wang, Z., Huang, G., Li, H., Chen, W., and Lee, J.Y., *Few-layer SnS2/graphene hybrid with exceptional electrochemical performance as lithium-ion battery anode.* Journal of Power Sources, 2012. **201**: p. 259.

170. Bhaskar, A., Deepa, M., and Rao, T.N., *Tin disulfide nanoflowers versus nanosheets as anodes in lithium-ion batteries: how the nanostructure controls performance.* Electrochimica Acta, 2015. **184**: p. 239.

171. Ramakrishna Reddy, K.T., Purandhara Reddy, P., Datta, P.K., and Miles, R.W., *Formation of polycrystalline SnS layers by a two-step process.* Thin Solid Films, 2002. **403–404**: p. 116.

172. Mutsumi, S., Keisuke, M., Takehiro, M., Kenichi, O., Koji, N., and Hisayuki, N., *Preparation of SnS films by sulfurization of Sn sheet.* Japanese Journal of Applied Physics, 2008. **47**(6R): p. 4494.

173. Klochko, N.P., Momotenko, O.V., Tyukhov, I.I., Volkova, N.D., Kopach, V.R., Khrypunov, G.S., Lyubov, V.M., and Kirichenko, M.V., *Structure and properties of SnS thin layers obtained by sulfurization of electrodeposited tin precursors.* Solar Energy, 2015. **118**: p. 117.

174. Polivtseva, S., Acik, I.O., Katerski, A., Mere, A., Mikli, V., and Krunks, M., *Spray pyrolysis deposition of SnxSy thin films.* Energy Procedia, 2014. **60**: p. 156.

175. Messaoudi, M., Aida, M.S., Attaf, N., Bezzi, T., Bougdira, J., and Medjahdi, G., *Deposition of tin(II) sulfide thin films by ultrasonic spray pyrolysis: evidence of sulfur exo-diffusion.* Materials Science in Semiconductor Processing, 2014. **17**: p. 38.

176. Sajeesh, T.H., Warrier, A.R., Kartha, C.S., and Vijayakumar, K.P., *Optimization of parameters of chemical spray pyrolysis technique to get n and p-type layers of SnS.* Thin Solid Films, 2010. **518**(15): p. 4370.

177. Thangaraju, B. and Kaliannan, P., *Spray pyrolytic deposition and characterization of SnS and SnS2 thin films.* Journal of Physics D-Applied Physics, 2000. **33**(9): p. 1054.

178. Sato, N., Ichimura, M., Arai, E., and Yamazaki, Y., *Characterization of electrical properties and photosensitivity of SnS thin films prepared by the electrochemical deposition method.* Solar Energy Materials and Solar Cells, 2005. **85**(2): p. 153.

179. Price, L.S., Parkin, I.P., Hardy, A.M.E., Clark, R.J.H., Hibbert, T.G., and Molloy, K.C., *Atmospheric pressure chemical vapor deposition of tin sulfides (SnS, Sn2S3, and SnS2) on glass.* Chemistry of Materials, 1999. **11**(7): p. 1792.

180. Park, H.K., Jo, J., Hong, H.K., Song, G.Y., and Heo, J., *Structural, optical, and electrical properties of tin sulfide thin films grown with electron-beam evaporation.* Current Applied Physics, 2015. **15**(9): p. 964.

181. Devika, M., Reddy, N.K., Reddy, D.S., Ahsanulhaq, Q., Ramesh, K., Gopal, E.S.R., Gunasekhar, K.R., and Hahn, Y.B., *Synthesis and characterization of nanocrystalline SnS films grown by thermal evaporation technique.* Journal of the Electrochemical Society, 2008. **155**(2): p. H130.

182. Jeng, M.J., Yang, H.C., and Chang, L.B., *Tin sulfide thin films prepared by thermal evaporation and sulfurization.* 2014 IEEE 40th Photovoltaic Specialist Conference (Pvsc), 2014: p. 379.

183. Robles, V., Trigo, J.F., Guillen, C., and Herrero, J., *Structural, chemical, and optical properties of tin sulfide thin films as controlled by the growth temperature during co-evaporation and subsequent annealing.* Journal of Materials Science, 2013. **48**(11): p. 3943.

184. Reddy, N.K., Ramesh, K., Ganesan, R., Reddy, K.T.R., Gunasekhar, K.R., and Gopal, E.S.R., *Synthesis and characterisation of co-evaporated tin sulphide thin films.* Applied Physics a-Materials Science & Processing, 2006. **83**(1): p. 133.

185. Sousa, M.G., da Cunha, A.F., and Fernandes, P.A., *Annealing of RF-magnetron sputtered SnS2 precursors as a new route for single phase SnS thin films.* Journal of Alloys and Compounds, 2014. **592**: p. 80.

186. Sinsermsuksakul, P., Heo, J., Noh, W., Hock, A.S., and Gordon, R.G., *Atomic layer deposition of tin monosulfide thin films.* Advanced Energy Materials, 2011. **1**(6): p. 1116.

187. Balaz, P., Takacs, L., Ohtani, T., Mack, D.E., Boldizarova, E., Soika, V., and Achimovicova, M., *Properties of a new nanosized tin sulphide phase obtained by mechanochemical route.* Journal of Alloys and Compounds, 2002. **337**: p. 76.

188. Balaz, P., Ohtani, T., Bastl, Z., and Boldizarova, E., *Properties and reactivity of mechanochemically synthesized tin sulfides.* Journal of Solid State Chemistry, 1999. **144**(1): p. 1.

189. Salavati-Niasari, M., Ghanbari, D., and Davar, F., *Shape selective hydrothermal synthesis of tin sulfide nanoflowers based on nanosheets in the presence of thioglycolic acid.* Journal of Alloys and Compounds, 2010. **492**(1-2): p. 570.

190. Wang, C.R., Tang, K.B., Yang, Q., Qian, Y.T., and Xu, C.Y., *Hydrothermal synthesis and characterization of SnS2 nanocrystals.* Chemistry Letters, 2001(12): p. 1294.

191. Ji, Y., Zhang, H., Ma, X., Xu, J., and Yang, D., *Single-crystalline SnS2 nano-belts fabricated by a novel hydrothermal method.* Journal of Physics: Condensed Matter, 2003. **15**(44): p. L661.

192. Tang, H., Yu, J., and Zhao, X., *Solvothermal synthesis of novel dendrite-like SnS particles in a mixed solvent of ethylenediamine and dodecanethiol.* Journal of Alloys and Compounds, 2008. **460**(1-2): p. 513.

193. Schlecht, S. and Kienle, L., *Mild solvothermal synthesis and TEM investigation of unprotected nanoparticles of tin sulfide.* Inorganic Chemistry, 2001. **40**(22): p. 5719.

194. Koktysh, D.S., McBride, J.R., and Rosenthal, S.J., *Synthesis of SnS nanocrystals by the solvothermal decomposition of a single source precursor.* Nanoscale Research Letters, 2007. **2**(3): p. 144.

195. Chauhan, H., Singh, M.K., Hashmi, S.A., and Deka, S., *Synthesis of surfactant-free SnS nanorods by a solvothermal route with better electrochemical properties towards supercapacitor applications.* RSC Advances, 2015. **5**(22): p. 17228.

196. Hai, B., Tang, K.B., Wang, C.R., An, C.H., Yang, Q., Shen, G.Z., and Qian, Y.T., *Synthesis of SnS2 nanocrystals via a solvothermal process.* Journal of Crystal Growth, 2001. **225**(1): p. 92.

197. Qian, X.F., Zhang, X.M., Wang, C., Wang, W.Z., Xie, Y., and Qian, Y.T., *Solvent-thermal preparation of nanocrystalline tin chalcogenide.* Journal of Physics and Chemistry of Solids, 1999. **60**(3): p. 415.

198. Su, H.L., Xie, Y., Xiong, Y.J., Gao, P., and Qian, Y.T., *Preparation and morphology control of rod-like nanocrystalline tin sulfides via a simple ethanol thermal route.* Journal of Solid State Chemistry, 2001. **161**(2): p. 190.

199. An, C.H., Tang, K.B., Shen, G.Z., Wang, C.R., Yang, Q., Hai, B., and Qian, Y.T., *Growth of belt-like SnS crystals from ethylenediamine solution.* Journal of Crystal Growth, 2002. **244**(3-4): p. 333.

200. Shen, G.Z., Chen, D., Tang, K.B., Huang, L.Y., Qian, Y.T., and Zhou, G., *Novel polyol route to nanoscale tin sulfides flaky crystallines.* Inorganic Chemistry Communications, 2003. **6**(2): p. 178.

201. Chen, D., Shen, G.Z., Tang, K.B., Lei, S.J., Zheng, H.G., and Qian, Y.T., *Microwave-assisted polyol synthesis of nanoscale SnSx(x=1,2) flakes.* Journal of Crystal Growth, 2004. **260**(3-4): p. 469.

202. Kang, J.G., Ko, Y.D., Choi, K.J., Park, J.G., and Kim, D.W., *Fabrication of tin monosulfide nanosheet arrays using laser ablation.* Applied Physics a-Materials Science & Processing, 2011. **103**(2): p. 505.

Chapter 3

Experimental Methods

This chapter summarizes the various methodologies employed in the synthesis and characterization of the metal sulfides studied in this dissertation. The metal sulfides used in this study were all synthesized via a solution-based chemical synthesis method using different precursors and conditions. X-ray diffraction, Raman spectroscopy and transmission electron microscopy were used to study the phase and purity of the as-synthesized samples, while field emission scanning electron microscopy was employed to find out their particle size and morphology. The procedures used to fabricate the lithium ion cells and the experimental parameters used for evaluating the electrochemical properties of the assembled battery cells are also stated in this chapter. To study the lithium storage properties of the as-synthesized samples, CR2032 coin cells were assembled based on the half-cell configuration cycled galvanostatically in the voltage range of 0.001–3 V at room temperature under various scan rates.

3.1 Material Synthesis

The metal sulfides used in this study were all synthesized via a solution-based chemical synthesis method using different precursors and conditions. This method of synthesis was chosen for the study because of its versatility, wide range of available precursors, solvents and surfactants that can be used, and ease of parameters manipulation to form metal sulfides of different phases and morphologies.

3.1.1 Synthesis of Iron Sulfide Particles

The materials used for the synthesis of iron sulfides in this study includes anhydrous iron(II) chloride ($FeCl_2$, anhydrous, 99.5%, Alfa Aesar), sulfur powder (S, -325 mesh, 99.5%, Alfa Aesar) and oleylamine (technical grade, 70%, Sigma Aldrich). All the chemicals were used without any further purification or treatment.

Table 3.1: Sample codes and amount of precursors used for the synthesis of the iron sulfide samples.

	Sample Code			
	Fe-S_1	**Fe-S_2**	**Fe-S_4**	**Fe-S_6**
Amount of Anhydrous $FeCl_2$ (mmol)	0.5	0.5	0.5	0.5
Amount of S (mmol)	0.5	1.0	2.0	3.0
Fe : S Molar Ratio	1 : 1	1 : 2	1 : 4	1 : 6

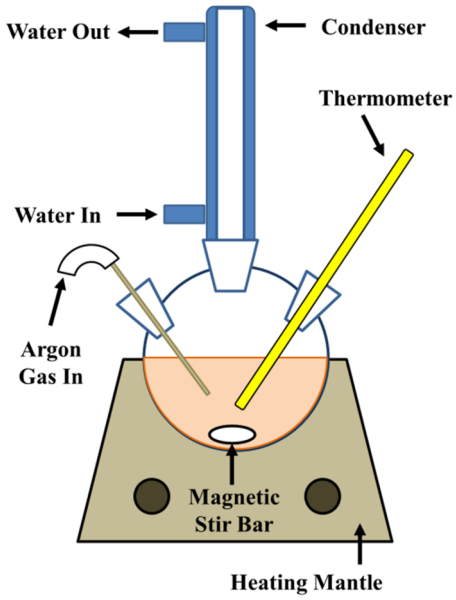

Figure 3.1: Schematic illustration of the reaction set-up for the metal sulfide particle synthesis.

The sample code and amount of precursors used for the synthesis of the different iron sulfide samples are shown in Table 3.1 and a schematic illustration of the reaction set-up is depicted in Figure 3.1. In general, 0.5 mmol of anhydrous $FeCl_2$ powder and the required amounts of S powder (Table 3.1) were added into a three-neck round bottom flask containing 10 mL of oleylamine. Oleylamine was used in this synthesis because of its various functions. Firstly, oleylamine has the ability to donate electron at elevated temperatures, thereby acting as a reducing agent in the absence of strong reducing agents. Its high boiling point of ≈ 360 °C makes it a good solvent choice for chemical reactions at moderately high temperatures (≥ 200 °C). Oleylamine is also known to form complex compounds with some metal ions and these metastable metal-oleylamine complex can function as secondary precursors in the synthesis of nanoparticles. [1] Besides being able to act as reducing agent, solvent and surfactant, other reasons for using oleylamine in this synthesis includes its liquid state at room temperature which simplifies the collection and washing of the prepared powder and its lower cost compared to many commonly-used alkylamines. [2]

The mixture was degassed by bubbling it with argon gas for 10 min at approximately 60 °C under magnetic stirring to dissolve the powders in the solvent completely and to remove the moisture and oxygen in the mixture. Subsequently, this mixture was heated to 220 °C and held for 30 min under stirring in argon atmosphere. After reaction, the round bottom flask was removed from the heating mantle and allowed to cool to room temperature naturally. Methanol was then added into the mixture to precipitate the particles. The precipitated particles were isolated by centrifuging the mixture at 8000 revolutions per minute (rpm) for 10 min and then removing the supernatant. Following, the collected powder was washed by dispersing it in 20 mL of technical hexane via sonication and subjecting this dispersion to centrifugation at 8000 rpm for 10 min. The supernatant was decanted to collect the washed powder and this washing procedure was repeated for 5 times to remove the excess sulfur and oleylamine. The washed powder was dried at 50 °C in a vacuum oven overnight prior to collection for further characterization.

3.1.2 Synthesis of Tin Sulfide Particles

The materials used for the synthesis of tin sulfides in this study includes anhydrous tin(II) chloride ($SnCl_2$, anhydrous, 98%, Alfa Aesar), sulfur powder (S, -325 mesh, 99.5%, Alfa Aesar), oleylamine (technical grade, 70%, Sigma Aldrich) and 1-octadecene (technical grade, 90%, Sigma Aldrich). All the chemicals were used without any further purification or treatment.

Table 3.2: Sample codes and reaction duration for the tin sulfide samples.

	Sample Code			
	Sn-S_30	**Sn-S_60**	**Sn-S_120**	**Sn-S_Onight**
Reaction Duration (min)	30	60	120	Overnight

A schematic illustration of the reaction set-up for this synthesis is shown in Figure 3.1. A typical reaction involves adding 0.5 mmol of anhydrous $SnCl_2$ powder and 3.0 mmol of S powder into a three-neck round bottom flask containing 5 mL of oleylamine and 5 mL of 1-octadecene. The mixture was degassed by bubbling it with argon gas for 10 min at approximately 60 °C under magnetic stirring to dissolve the powders and to remove the moisture and oxygen in it. Subsequently, this mixture was heated to 240 °C and held for different durations (Table 3.2) under stirring in argon atmosphere. After reaction, the round bottom flask was removed from the heating mantle and allowed to cool to room temperature naturally when methanol was then added into the mixture to precipitate the particles. The precipitated particles were isolated by centrifuging the mixture at 8000 rpm for 10 min and then removing the supernatant. Following, the collected powder was washed by dispersing it in 20 mL of technical hexane via sonication and subjecting this dispersion to centrifugation at 8000 rpm for 10 min. The supernatant was decanted to collect the washed powder and this washing procedure was repeated for 5 times to remove the excess sulfur and oleylamine. The washed powder was dried at 50 °C in a vacuum oven overnight prior to collection for further characterization.

3.2 Materials Characterization

3.2.1 Powder X-ray Diffraction (XRD)

The phase and crystal structural information of the synthesized powders were characterized by powder X-ray diffraction (Bruker AXS, D8 Advance) using a Cu Kα radiation (λ = 0.15418 nm) and scanned in the 2θ range of either 20 – 70° or 10 – 70° at a step width of 0.05°. The X-ray diffractometer was equipped with a 1° divergence slit, 2.5° soller slit and 0.3 mm receiving slit. XRD was done on the as-synthesized powders without any further sample preparation steps.

XRD is chosen to determine the phase and purity of the as-synthesized powders because of various reasons. Besides its ability to differentiate between the many crystalline metal sulfide phases like SnS and SnS_2 and good detection limit (generally able to see obvious diffraction peaks if the phase present in the sample is polycrystalline and > 5wt%), XRD is a non-destructive technique and the powders used for XRD characterization can be re-used for other characterization. Furthermore, this technique does not require a large amount of powders for the measurement. These two factors are especially important as the samples prepared and studied in this dissertation are synthesized in small scale (< 100 mg) via a solution-based chemical synthesis method. Other advantages of using XRD to determine the phase and purity of the powder samples in this thesis includes its short measurement time-span and ease of XRD sample preparation.

3.2.2 Raman Spectroscopy

Raman spectroscopy, a type of vibrational spectroscopy, is a technique that probes the interaction of a monochromatic light with the molecular vibrations in a molecule to elucidate the molecular structure of a sample. [3, 4] During a standard Raman experiment, the sample is irradiated with monochromatic radiation from a laser. Some of the laser sources used in a Raman experiment includes those in the ultraviolet (UV), visible and near-infrared region (785 and 1064 nm). It should be noted that the Raman scattered light will be in the UV region if the laser source used for the excitation is in the UV region. In order for Raman bands to be observed, the molecular vibration in the sample must cause a change in the polarizability. In other words, only molecular vibrations that can result in a polarizability change are Raman active. Raman spectra are generally analyzed by looking at the intensity, frequency and shape of the vibrational bands which can provide information regarding the molecular structure and environment. As each molecule has its own unique set of vibrational energy levels, its Raman spectrum can function as a “fingerprint” for this particular molecule.

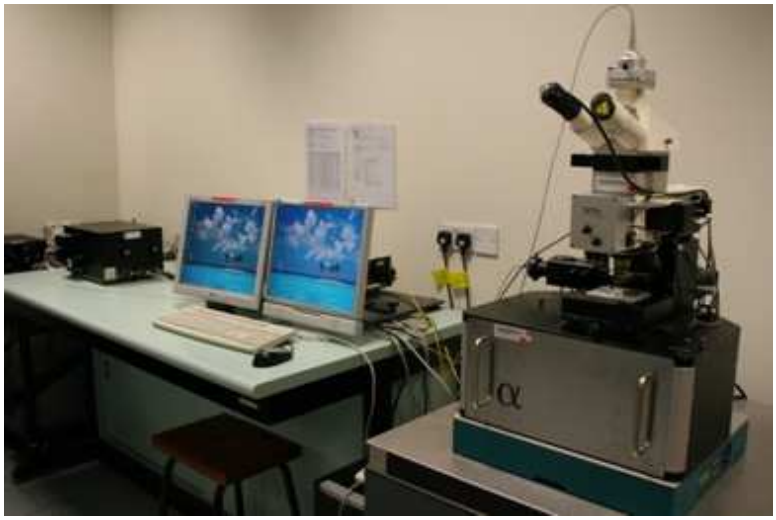

Figure 3.2: Photo of the confocal Raman microscopy system (WITec alpha300 SR) used in this dissertation.

For this dissertation, Raman spectroscopy was performed using a confocal Raman microscopy system (WITec alpha300 SR) (Figure 3.2) with a 488 nm diode laser to study the phase and phase purity of the as-synthesized iron sulfide powders. The Raman samples were prepared by dispersing a small amount of the as-synthesized powder in hexane via sonication and drop-casting a few drops of the dispersion onto a small piece (≈ 5 × 5 mm) of polished silicon wafer. After drying, the drop-casted samples were used directly for Raman experiments.

As iron sulfide has many different phases such as FeS, Fe_3S_4, Fe_7S_8, $Fe_{1-x}S$, marcasite FeS_2 and pyrite FeS_2, each with a different iron to sulfur stoichiometric ratio and atomic arrangement, and the XRD patterns for these various phases have numerous overlaying diffraction peaks, making it extremely challenging to differentiate the diffraction peak for one phase from that of the other phase, particularly when the impurity phase is present in infinitesimal amount with only a few low-intensity peaks in the diffraction pattern. Furthermore, XRD is only good for distinguishing between crystalline phases. Hence, Raman spectroscopy, a technique that probes the chemical bonding between the atoms in a compound, is used to discriminate between the different phases of iron sulfides such as pyrite FeS_2, marcasite FeS_2 and FeS, even when the phases present are

amorphous in nature is employed to further verify the phase purity of the as-synthesized powders.

3.2.3 Field-Emission Scanning Electron Microscopy (FESEM)

A field-emission scanning electron microscope (JEOL JSM-7600F) was used to examine the size and morphology of the as-synthesized powders. This technique was chosen mainly because of its ability to view particles and features that are in the nanometre regime. In fact, JEOL JSM-7600F has a resolution of 1.0 nm when operated at an accelerating voltage of 15 kV. Other reasons for choosing this technique includes the ease of sample preparation and the short duration needed for this characterization technique. The samples for the FESEM characterization were prepared using a similar method as that for the Raman characterization. FESEM images were obtained by sticking the silicon wafers onto the sample holder using a carbon tape and scanning them at a working distance of 6 cm and an accelerating voltage of 5 kV. No additional coating was applied onto the samples prior to scanning.

3.2.4 Transmission Electron Microscopy (TEM)

High resolution transmission electron microscopy (HRTEM) (JEOL JEM-2010) was performed at an accelerating voltage of 200 kV to study the size, morphology and crystallographic structure. With a point resolution of about 2.3 Å, the JEOL JEM-2010 HRTEM allows the imaging of the as-synthesized material at atomic scale, enabling a qualitative study on the crystallinity of the particle i.e. does the particle have good crystallinity with well-aligned lattice fringes and allows a confirmation on the phase of the material. The TEM sample was prepared via a similar method as the Raman and FESEM samples but the dispersion was drop-casted onto a carbon-laced copper grid instead of silicon wafer.

3.2.5 Porosity Measurement

Nitrogen adsorption/desorption isotherm was measured on a Micromeritics ASAP 2020 at –196 °C. The samples were degassed at 120 °C for 4 h under vacuum prior to measurement and the specific surface area was calculated using the Brunauer-Emmet-Teller (BET) method. This is a most common method used for determining the surface area and porosity of powder and porous solid samples. Typically, nitrogen gas is used as the probe molecule. During measurement, the sample is exposed to the nitrogen gas at –196 °C i.e. the boiling temperature of nitrogen and the surface area of the material is calculated from the measured monolayer capacity and the cross-sectional area of the probe molecule.

3.3 Electrochemical Characterization

3.3.1 CR2032 Coin Cell Fabrication

To study the lithium storage properties of the as-synthesized samples, CR2032 coin cells were assembled based on the half-cell configuration. [5-8] This configuration allows the evaluation of the lithium storage capability of the materials without having the need to determine the amount of materials needed for the counter electrode, which could be hard to determine for materials of different phases and morphology. Fabrication of the working electrode was done by first mixing the as-synthesized metal sulfide powder with carbon nanotubes (CNT, P3-SWNT, Carbon Solutions) and poly(vinylidene fluoride) (PVDF) at a weight ratio of 8:1:1 and dispersing them in N-methylpyrrolidone (NMP, 99+%, Alfa Aesar) to form a slurry. CNT was added into the slurry to improve the electrical conductivity of the electrode, while PVDF was used to enhance the binding between the electrode material and the current collector. The resultant slurry was then coated onto a circular copper foil (diameter = 14 mm) which function as a current collector in the battery cell. Following, the coated copper foil was dried in an oven at 50 °C under vacuum for overnight. CR2032 coin cells were

assembled using the dried slurry-coated copper foil as the working electrode, lithium foil as the counter and reference electrode and Celgard 2400 membrane as the separator. The solution made up by dissolving lithium fluorophosphate ($LiPF_6$) in a mixed solvent consisting of an equal weight ratio of ethylene carbonate (EC) and dimethyl carbonate (DMC) to form a 1 M $LiPF_6$ solution was used as the electrolyte for these battery cells. The whole battery-assembling process was carried out in an argon-filled glovebox (MBraun, Germany) where both the oxygen and moisture content were maintained at less than 1 ppm.

3.3.2 Galvanostatic Cycling

The assembled CR2032 coin cells were cycled galvanostatically in the voltage range of 0.001 – 3 V at room temperature under various current densities (0.1 A g^{-1}, 0.5 A g^{-1}, 1 A g^{-1} and 5 A g^{-1}) using a NEWARE Multi-channel Battery Test System. These were done to study the lithium storage performance of the different as-synthesized metal sulfide electrode when cycled at different rates. In fact, subjecting assembled cells to galvanostatic cycling in a pre-defined voltage range is the most widely-used method for evaluation of the cycling performance of a battery cell like lithium ion battery, lithium-air battery and sodium ion battery.

3.3.3 Cyclic Voltametry

Cyclic voltammetry (CV) measurements were done on the assembled CR2032 coin cell to gain an insight into the reaction between the electrode materials and Li ions during charge-discharge cycling. The measurements were carried out at room temperature using a Solartron 1470E analytical equipment in the voltage window of 0.001 – 3 V under a constant scan rate of 0.2 mV s^{-1}. Since lithium foil (0 V *vs.* Li/Li^+) was used as the counter and reference electrode in the assembled battery, the cathodic peaks would be associated with the insertion of lithium ions into the working electrode, while the anodic peaks are related to the extraction of lithium ions from the working electrode.

References:

1. Joo, J., Na, H.B., Yu, T., Yu, J.H., Kim, Y.W., Wu, F., Zhang, J.Z., and Hyeon, T., *Generalized and facile synthesis of semiconducting metal sulfide nanocrystals.* Journal of the American Chemical Society, 2003. **125**(36): p. 11100.
2. Mourdikoudis, S. and Liz-Marzan, L.M., *Oleylamine in nanoparticle synthesis.* Chemistry of Materials, 2013. **25**(9): p. 1465.
3. Larkin, P., *Chapter 1 - Introduction: Infrared and Raman spectroscopy,* in *Infrared and Raman spectroscopy,* P. Larkin, Editor. 2011, Elsevier: Oxford. p. 1-5.
4. *Chapter 2 - Basic principles,* in *Infrared and Raman spectroscopy,* P. Larkin, Editor. 2011, Elsevier: Oxford. p. 7-25.
5. Zhu, J.X., Lu, Z.Y., Oo, M.O., Hng, H.H., Ma, J., Zhang, H., and Yan, Q.Y., *Synergetic approach to achieve enhanced lithium ion storage performance in ternary phased SnO2-Fe2O3/rGO composite nanostructures.* Journal of Materials Chemistry, 2011. **21**(34): p. 12770.
6. Zhu, X., Zhu, Y., Murali, S., Stoller, M.D., and Ruoff, R.S., *Nanostructured reduced graphene oxide/Fe2O3 composite as a high-performance anode material for lithium ion batteries.* ACS Nano, 2011. **5**(4): p. 3333.
7. Xu, C., Zeng, Y., Rui, X., Xiao, N., Zhu, J., Zhang, W., Chen, J., Liu, W., Tan, H., Hng, H.H., and Yan, Q., *Controlled soft-template synthesis of ultrathin C@FeS nanosheets with high-Li-storage performance.* Acs Nano, 2012. **6**(6): p. 4713.
8. Liu, W.L., Rui, X.H., Tan, H.T., Xu, C., Yan, Q.Y., and Hng, H.H., *Solvothermal synthesis of pyrite FeS2 nanocubes and their superior high rate lithium storage properties.* RSC Advances, 2014. **4**(90): p. 48770.

Chapter 4

Iron Sulfides and Their Lithium Storage Properties

This chapter presents the results on the synthesis of iron sulfides via a solution-based chemical synthesis method (procedures detailed in Section 3.1.1). The phase, purity, size and morphology of the as-synthesized powders were characterized using X-ray diffraction, field emission scanning electron microscopy, transmission electron microscopy and Raman spectroscopy. The effect of the molar ratio between the iron and sulfur (Fe:S) precursors on the phase and morphology of the as-synthesized products is investigated and discussed in this chapter. The effect of the iron to sulfur stoichiometric ratio of the as-synthesized iron sulfides on their lithium storage properties was also studied and presented in this chapter. It was found that pyrite FeS_2 exhibits better lithium storage capability than pyrrhotite $Fe_{1-x}S$ when cycled between 0.001 – 3 V and this observation can be attributed to: (1) the lower polarization, better electron and Li^+ ion transport at the interface between the active material and electrolyte at the pyrite FeS_2 electrode than the pyrrhotite $Fe_{1-x}S$ electrode and (2) the reversible lithiation and delithiation of iron sulfide (FeS_y) during the galvanostatic cycling of the pyrite FeS_2 electrode.

4.1 Synthesis and Characterization of Iron Sulfide Particles

To obtain pure phases of the different iron sulfide compounds, four different pots of reaction were carried out with all parameters kept constant except for the molar ratio between the anhydrous $FeCl_2$ and S powder precursors used for the reaction. The experimental parameters and procedures were detailed in Section 3.1.1, where the powder synthesized with an Fe:S precursor molar ratio of 1:1, 1:2, 1:4 and 1:6 are labelled as Fe-S_1, Fe-S_2, Fe-S_4 and Fe-S_6 respectively. Thereafter, the as-synthesized powders were characterized using various techniques.

X-ray diffraction (XRD) was performed on the as-synthesized powders to determine their phase, crystal structure and purity, and the XRD patterns collected for Fe-S_1, Fe-S_2, Fe-S_4 and Fe-S_6 are displayed in Figure 4.1. It can be observed that these patterns have sharp and well-defined diffraction peaks, suggesting the good crystallinity of all four samples even without any post-annealing. XRD also shows that the sample synthesized with an Fe:S precursor molar ratio of 1:1 (Fe-S_1) has a hexagonal iron pyrrhotite ($Fe_{1-x}S$, where $0 \leq x \leq 0.2$) phase with lattice parameters, a = 6.9 Å and c = 28.7 Å (JCPDS 029-0724), while that synthesized with an Fe:S precursor molar ratio of 1:6 (Fe-S_6) has a cubic iron pyrite (FeS_2) phase with lattice parameter, a = 5.4 Å (JCPDS 042-1340). No impurity peak was observed in both XRD patterns, indicating the good purity of the as-synthesized Fe-S_1 and Fe-S_6 samples. From Figure 4.1, it can be seen that Fe-S_4 displayed a similar XRD pattern as that for Fe-S_6, indicating that these two samples have the same phase and that the sample synthesized with an Fe:S precursor molar ratio of 1:4 also consists of pyrite FeS_2 (JCPDS 042-1340) particles. It is also observed that the XRD pattern of Fe-S_4 have fewer diffraction peaks than that of Fe-S_6, suggesting that Fe-S_6 could have a better crystallinity than Fe-S_4. The diffraction peaks in the XRD pattern of Fe-S_2 (Figure 4.1) can be matched to that of two crystal structures – a hexagonal pyrrhotite $Fe_{1-x}S$ (JCPDS 029-0724) and a cubic greigite Fe_3S_4 (JCPDS 016-0713), indicating that this sample consists of a mixture of two different iron sulfide phases.

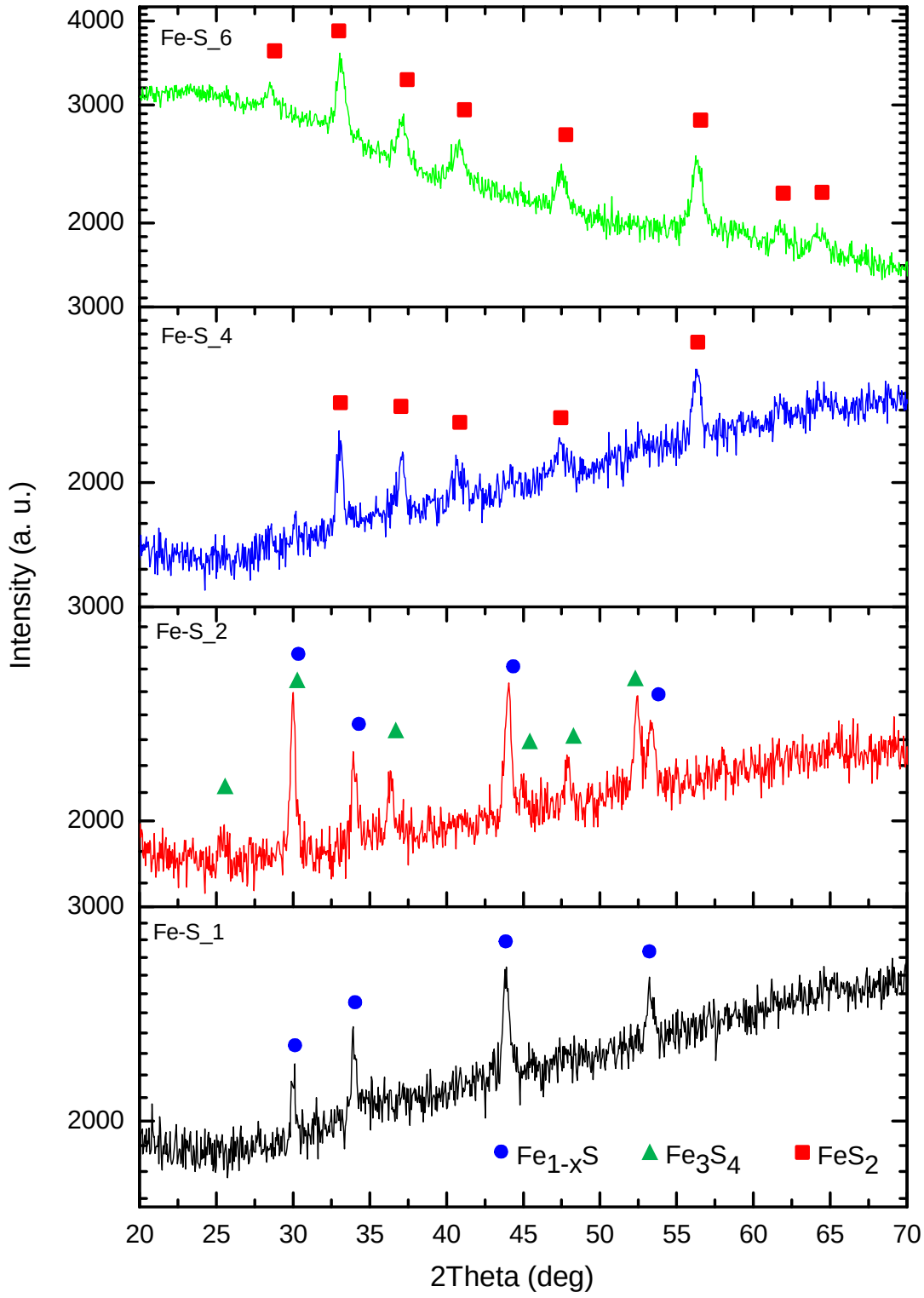

Figure 4.1: XRD patterns of Fe-S_1, Fe-S_2, Fe-S_4 and Fe-S_6.

As mentioned in Section 2.4.1, iron sulfide has many different phases such as FeS, Fe_3S_4, Fe_7S_8, $Fe_{1-x}S$, marcasite FeS_2 and pyrite FeS_2, each with a different iron to sulfur

stoichiometric ratio and atomic arrangement. The XRD patterns for these various phases have numerous overlaying diffraction peaks, making it extremely challenging to differentiate the diffraction peak for one phase from that of the other phase, particularly when the impurity phase is present in infinitesimal amount with only a few low-intensity peaks in the diffraction pattern. Furthermore, XRD is only good for the identification of crystalline phase and is unable to distinguish between amorphous phases. Raman spectroscopy, a technique that probes the chemical bonding between the atoms in a compound, has the capability to discriminate between the different phases of iron sulfides such as pyrite FeS_2, marcasite FeS_2 and FeS, even when the phases present are amorphous in nature. [1-3] Therefore, this technique is employed to further verify the phase purity of the as-synthesized powders.

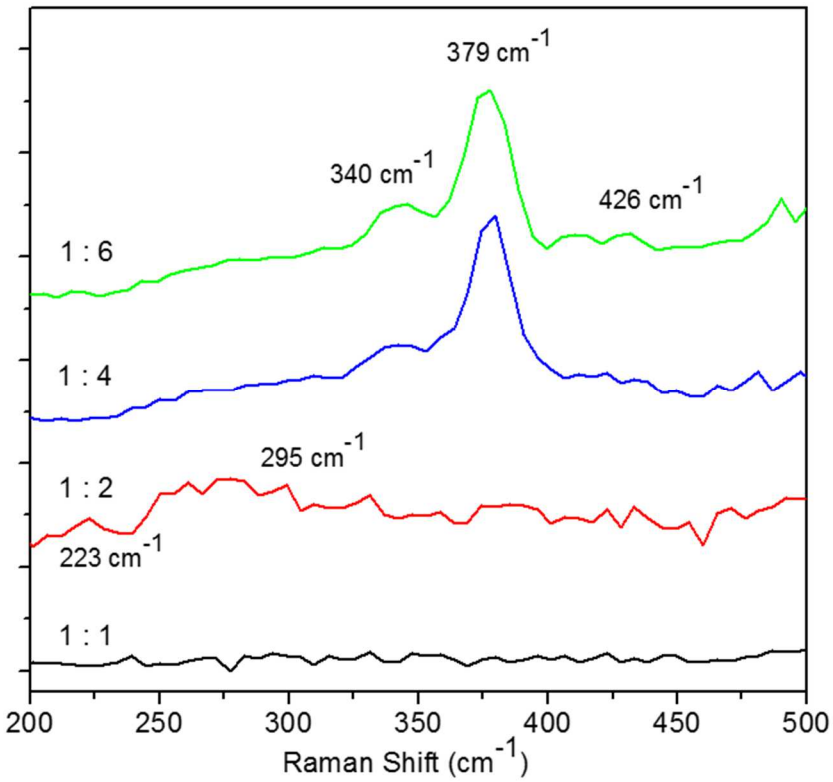

Figure 4.2: Raman spectra of Fe-S_1, Fe-S_2, Fe-S_4 and Fe-S_6

Figure 4.2 depicts the Raman spectra of the powders synthesized with an Fe:S precursor molar ratio of 1:1 (Fe-S_1), 1:2 (Fe-S_2), 1:4 (Fe-S_4) and 1:6 (Fe-S_6). It can be seen from the Raman spectrum of Fe-S_6 that there are only two obvious peaks in the

wavenumber range of 300 – 400 cm^{-1}. This characteristic two-peak spectrum indicates the existence of sulfur-sulfur (S-S) bond in the sample. [3, 4] The position of these peaks match well with that reported in literatures for pyrite iron sulfide (339 cm^{-1} and 378 cm^{-1}), with the peak at 340 cm^{-1} resulting from the translation of the S atoms along the direction perpendicular to the S-S bond axis (E_g mode) and that at 379 cm^{-1} caused by the in-phase stretching of the S_2 dumbbells (A_g mode) in the iron pyrite crystal. [5-7] A small peak is also observed at 426 cm^{-1} which corresponds to the Raman-active T_g mode of the iron pyrite crystal caused by several librational, stretching or their combination. [8, 9] Both FeS and marcasite FeS_2 are not present in Fe-S_6 as evidenced by the absence of Raman peaks at 214 cm^{-1} and 282 cm^{-1} for the FeS phase and at 324 cm^{-1} and 387 cm^{-1} for the marcasite FeS_2 phase. [2, 10] This further confirmed the phase purity of the powder synthesized with an Fe:S precursor molar ratio of 1:6 (Fe-S_6). A Raman spectrum similar to that of Fe-S_6 was observed for Fe-S_4, which is in consistent with their XRD results presented in Figure 4.1 where both samples are determined to have the same pyrite FeS_2 phase.

It can also be seen from Figure 4.2 that there is no obvious peak in the Raman spectrum of Fe-S_1, indicating the absence of iron sulfide compounds with Raman-active species like pyrite FeS_2, marcasite FeS_2 and FeS in this sample. From the XRD pattern of Fe-S_1 (Figure 4.1), it can be seen that this sample has an iron pyrrhotite ($Fe_{1-x}S$) phase and this phase is known to have two polymorphs, namely, hexagonal and monoclinic structure. By using factor group analysis, Mernagh and Trudu predicted that the vibrational modes in both polymorphs are not Raman-active if their crystal structures are ideal and, from their experimental results, no first and second order spectra were observed from the Raman analysis of both materials. [10] Although Raman peaks were observed in the spectrum of some pyrrhotite ($Fe_{1-x}S$ where $0 \leq x \leq 0.2$) samples like that reported by Breier et al., it is believed that these peaks (377 cm^{-1}, 471 cm^{-1} and 676 cm^{-1}) could be the result when sample deviates from ideal pyrrhotite structure since the peaks that Breier et al obtained, though similar to that reported by Battaglia et al. (373 cm^{-1} and 465 cm^{-1}), is not very consistent and repeatable. [3, 11] Furthermore, these peak positions also differ from that reported by Bi et al. for the pyrrhotite $Fe_{1-x}S$ sample used in their study (292 cm^{-1} and 354 cm^{-1}). [7]

From the XRD pattern of Fe-S_2, it is determined that this sample consists of a mixture of pyrrhotite $Fe_{1-x}S$ and greigite Fe_3S_4 phases. As Fe_3S_4 has low metastability and is unstable even in argon atmosphere at temperatures above 240 ˚C, it is difficult to detect Fe_3S_4 in the Raman spectrum especially under ambient environment. [12-14] Instead, Raman peaks corresponding to that observed for Fe_3O_4 phase is commonly detected when Fe_3S_4 is subjected to Raman spectroscopy measurement in air due to an oxidation of Fe_3S_4 to Fe_3O_4 under laser illumination. [14, 15] Hence, two very weak peaks (223 cm^{-1} and 295 cm^{-1}) which can be assigned to the $T_{2g}(3)$ and E_g modes of Fe_3O_4 and no Raman peaks related to Fe_3S_4 phase are observed in the Raman spectrum of Fe-S_2 (Figure 4.2).

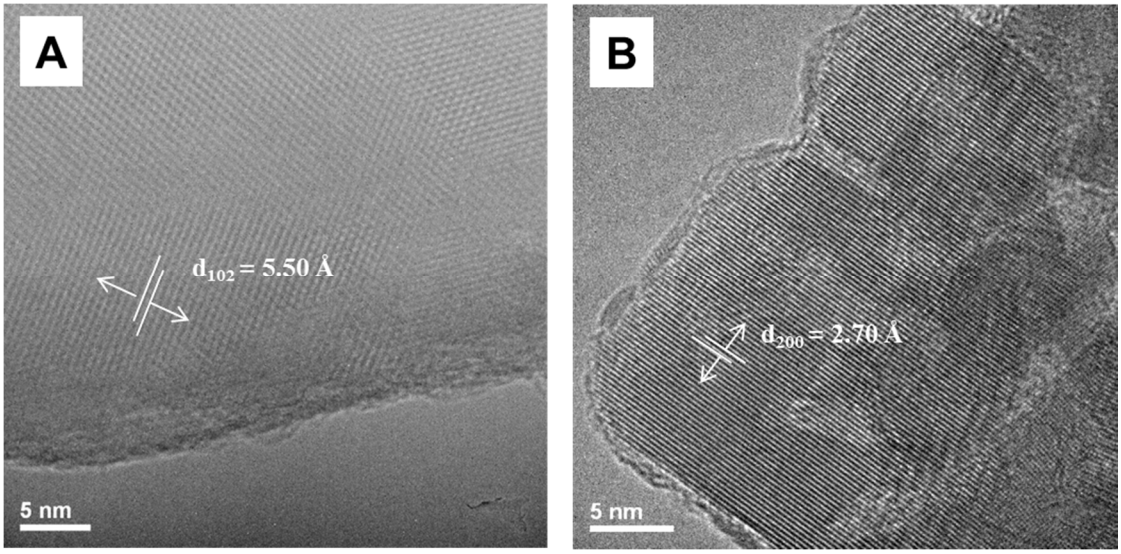

Figure 4.3: HRTEM images of (A) Fe-S_1 and (B) Fe-S_6.

High resolution transmission electron microscopy (HRTEM) were used to examine the crystallographic structure of the as-synthesized particles and the HRTEM images of Fe-S_1 and Fe-S_6 are presented in Figure 4.3. The HRTEM images show obvious and well-aligned lattice fringes for both samples, revealing their good crystallinity. From the HRTEM image of Fe-S_1 (Figure 4.3A), a spacing of 5.50 Å can be measured between two adjacent fringes on the face of the particle and this spacing matches well to the lattice spacing in the (1 0 2) plane of pyrrhotite $Fe_{1-x}S$, providing consistent result

as the XRD analysis for Fe-S_1. A distance of 2.70 Å can be measured between two adjacent fringes in the HRTEM image of Fe-S_6, which is similar to the lattice spacing in the (2 0 0) plane of a cubic pyrite FeS_2 crystal, affirming the phase of this sample.

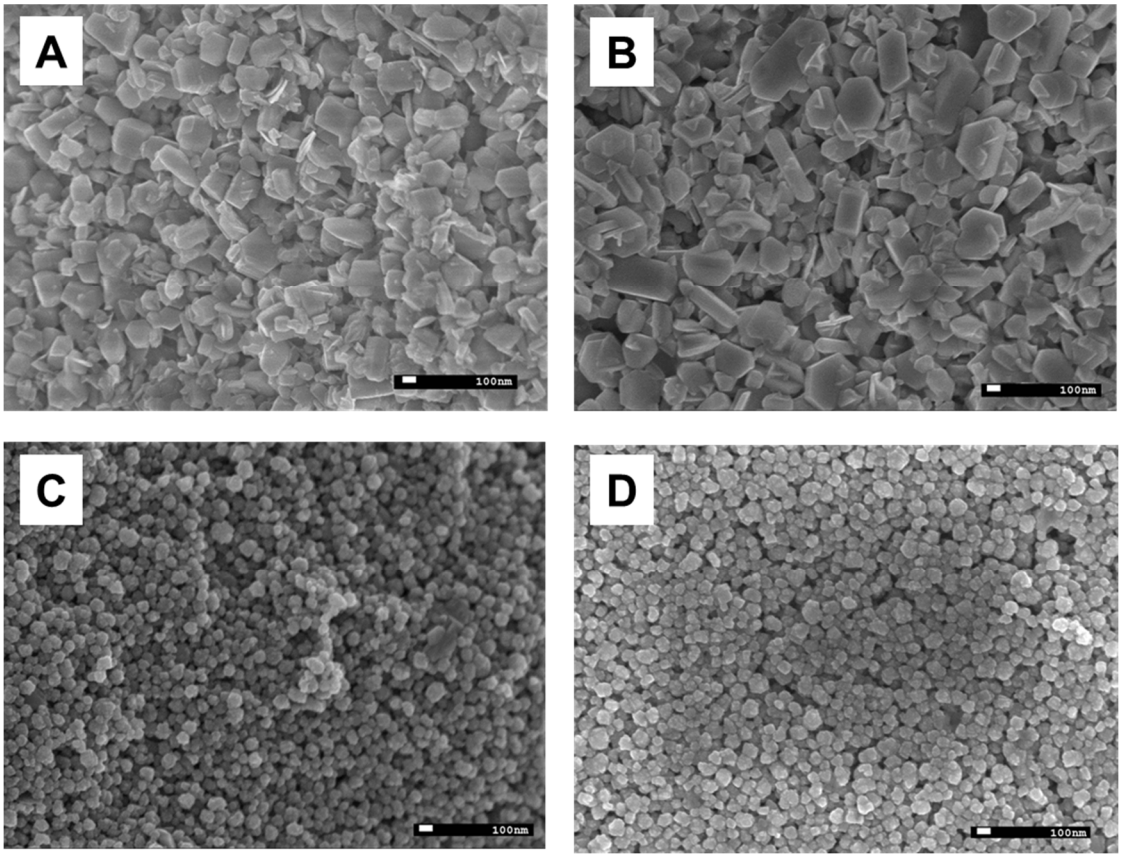

Figure 4.4: FESEM images of (A) Fe-S_1, (B) Fe-S_2, (C) Fe-S_4 and (D) Fe-S_6.

Field emission scanning electron microscopy (FESEM) was used to study the particle size and morphology of the four samples and their changes when the molar ratio between the iron and sulfur precursors was varied. Figure 4.4 shows the FESEM images of Fe-S_1, Fe-S_2, Fe-S_4 and Fe-S_6. From the FESEM image (Figure 4.4A), it can be seen that the sample synthesized with an Fe:S precursor molar ratio of 1:1 has a wide particle size distribution, with particles sizes ranging from about 80 nm to 300 nm. When the molar ratio between the iron and sulfur precursors is increased to 1:2, the particle size distribution is increased to a wider range of 100 – 700 nm (Figure 4.4B).

Fe-S_4 and Fe-S_6 consists of granular particles with sizes of around 80 nm and 100 nm respectively, as illustrated in Figure 4.4.

4.2 Effect of Iron to Sulfur Precursor Molar Ratio on the Synthesized Iron Sulfide Phase

In its normal state, sulfur exists as cycloocta-S (S_8) rings and is unable to react directly with $FeCl_2$ to form iron sulfide. [16, 17] However, it is well-known that amines can be used to activate elemental sulfur, thereby increasing its reactivity and enabling it to react with metal ions. [18-20] In fact, sulfur-amine solution formed by dissolving sulfur powder in amine, especially primary amine with long alkyl chain like oleylamine, is the precursor of choice for many bottom-up synthesis of metal sulfides. [21-23] Hence, oleylamine is being used in the reactions in this thesis, where it functioned as a solvent, a surfactant and, at the same time, a reducing agent. [24, 25] At low temperatures such as room temperature, sulfur exists mainly as alkylammonium polysulfides in oleylamine solution. [26, 27] Upon heating to high temperatures i.e. 220 °C, the hydrogen sulfide (H_2S), produced by the reaction of these polysulfide ions with the excess amine in the solution, can react with the Fe^{2+} ions from the metal precursor salt to form iron sulfides. [27]

Scheme 4.1: Proposed reaction pathway for the formation of pyrite iron sulfide from anhydrous iron chloride and elemental sulfur in oleylamine at elevated temperature.

$$(1-x)\ Fe^{2+} + S_x^{2-} \longrightarrow Fe_{1-x}S + S_{x-1}^{2-}$$

$$3\ Fe_{1-x}S + 3x\ Fe^{2+} + S_x^{2-} \longrightarrow Fe_3S_4 + S_{x-1}^{2-}$$

$$Fe_3S_4 + S_x^{2-} \longrightarrow 3\ FeS_2 + S_{x-2}^{2-}$$

Scheme 4.1 shows a proposed reaction pathway for the formation of pyrite FeS_2 from $FeCl_2$ and elemental S precursors based on literature and the experimental results obtained in this thesis. [28-30] From the XRD (Figure 4.1) and Raman characterization (Figure 4.2), it was found that pure pyrrhotite $Fe_{1-x}S$ (at% Fe : S = 1 : 1 – 1.25) powder is obtained when equal molar ratio of anhydrous $FeCl_2$ and elemental S were used as the starting materials in the synthesis. This is in good agreement with the reaction mechanism reported by Liu and co-workers, where it was found that anhydrous $FeCl_2$ and elemental S first reacted to form $Fe_{1-x}S$ before forming pyrite FeS_2 via solvothermal reaction with oleylamine as the solvent. [30] Hunger and Benning studied the hydrothermal reaction between ammonium iron(II) sulfate hexahydrate ($(NH_4)_2Fe(SO_4)_2 \cdot 6H_2O$) and elemental S, showing that this reaction proceeds with the formation of FeS to Fe_3S_4 and, finally, pyrite FeS_2 when there is an excess of elemental sulfur in the reaction mixture. [29] Under sulfur-limiting condition, a mixture of FeS, Fe_3S_4 and pyrite FeS_2 is obtained instead of pure pyrite FeS_2. [29] Similarly, in this thesis, it is observed that some of the $Fe_{1-x}S$ reacts with the remaining Fe^{2+} ions and excess S (present as polysulfide ions or H_2S) in the reaction mixture to form greigite Fe_3S_4 (at% Fe : S = 1 : 1.33) upon adding more S powder. Hence, when the molar ratio between the $FeCl_2$ and S precursors is increased to 1:2, the product obtained is a mixture of two phases – pyrrhotite $Fe_{1-x}S$ and greigite Fe_3S_4. In fact, Fe_3S_4 was observed to form as an intermediate product in many synthesis of pyrite FeS_2. [28, 31] Pyrite FeS_2 (at% Fe : S = 1 : 2) is only formed when the molar ratio of the precursors is increased to more than 1:4. This is in good agreement with the findings by Kar et al. who subjected $FeCl_3$ and Na_2S to a wet chemical reaction in de-ionized water followed by annealing in argon environment, and observed an increase in the amount of pyrite FeS_2 phase and a decrease in the amount of pyrrhotite $Fe_{1-x}S$ phase in the synthesized powder when the molar ratio between the iron and sulfur precursors is increased from 1:2 to 1:4. [32] From the experiments, it was found that iron sulfides such as $Fe_{1-x}S$, FeS, Fe_3S_4, FeS_2 or a mixture of them will be formed under sulfur-limiting conditions i.e an Fe:S precursor molar ratio of 1:1 or 1:2. Pure pyrite FeS_2 phase can only be formed when excess S is present in the reaction mixture i.e. an Fe:S precursor molar ratio of 1:4 or 1:6.

4.3 Electrochemical Properties

A series of electrochemical characterization was carried out according to the half-cell configuration described in Section 3.3.1 to examine the lithium storage properties of the as-synthesized pyrrhotite $Fe_{1-x}S$ (Fe-S_1) and pyrite FeS_2 (Fe-S_6). These two samples were chosen for the study because of their good purity which allows better comparison on the effect of how the number of sulfide ion in the stoichiometry of an iron sulfide compound i.e. Fe:S = 1:1 (FeS) or 1:2 (FeS_2) affects its lithium storage properties. It should be mentioned that care was taken to ensure that the two iron sulfide compounds were synthesized using the same precursors and surfactant to eliminate any possible effect due to the remaining surfactant on the as-synthesized particles. The fact that the synthesized $Fe_{1-x}S$ and FeS_2 particles do not have any fanciful morphologies eradicated the possible effect of particle morphology on the lithium storage performance of the two iron sulfide samples. To study the cycling performance of the as-synthesized iron sulfides, the assembled cells were cycled galvanostatically between 0.001 and 3 V (*vs.* Li/Li^+) at various current densities. Plots of the capacity of the working electrode against the cycle number for the cells cycled at various current densities are depicted in Figure 4.5 and Figure 4.6.

It can be seen from Figure 4.5 and Figure 4.6A that Fe-S_1 exhibits high initial discharge capacity of 958 mA h g^{-1}, 1127 mA h g^{-1} and 1072 mA h g^{-1} when cycled at a current density of 0.1 A g^{-1}, 0.5 A g^{-1} and 1 A g^{-1} respectively, and these high initial discharge capacities exceed the theoretical capacity of 609 mA h g^{-1} for $Fe_{1-x}S$ phase. [33] Such phenomenon where the discharge capacity of an electrode material exceeds its theoretical capacity, especially for the first cycle, has been observed for numerous material systems from insertion-typed anodic material like carbon, to alloying-typed anodic material like tin-antimony, and conversion-typed anodic material like cobalt oxide. [34-37] This additional lithium storage capacity has been widely accredited to the formation of a gel-like film, commonly known as the solid/electrolyte interphase (SEI) layer, on the surface of an electrode in a lithium ion battery made with alkyl carbonate-based electrolyte. [37] Fe-S_6 is observed to display similar phenomenon where its initial discharge capacities are higher than the theoretical capacity of FeS_2

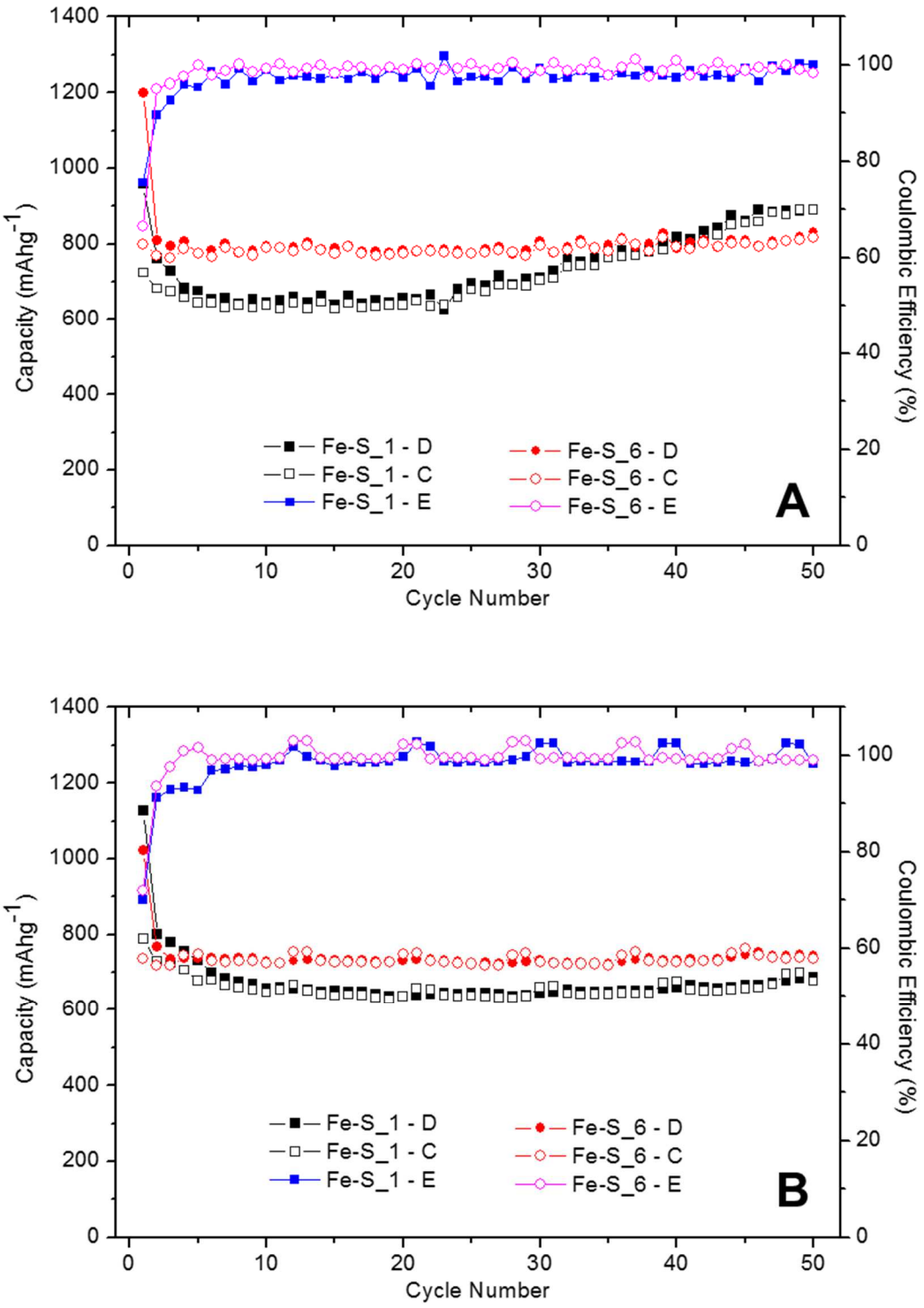

Figure 4.5: Cycling performance of the Fe-S_1 and Fe-S_6 electrodes at a current density of (A) 0.1 A g^{-1} and (B) 0.5 A g^{-1} between 0.001 and 3 V (*vs.* Li/Li^+). Fe-S_1 – D, Fe-S_1 – C and Fe-S_1 – E refers to the discharge and charge capacities and coulombic efficiency of Fe-S_1 respectively, while Fe-S_6 – D, Fe-S_6 – C and Fe-S_6 – E refers to the discharge and charge capacities and coulombic efficiency of Fe-S_6 correspondingly.

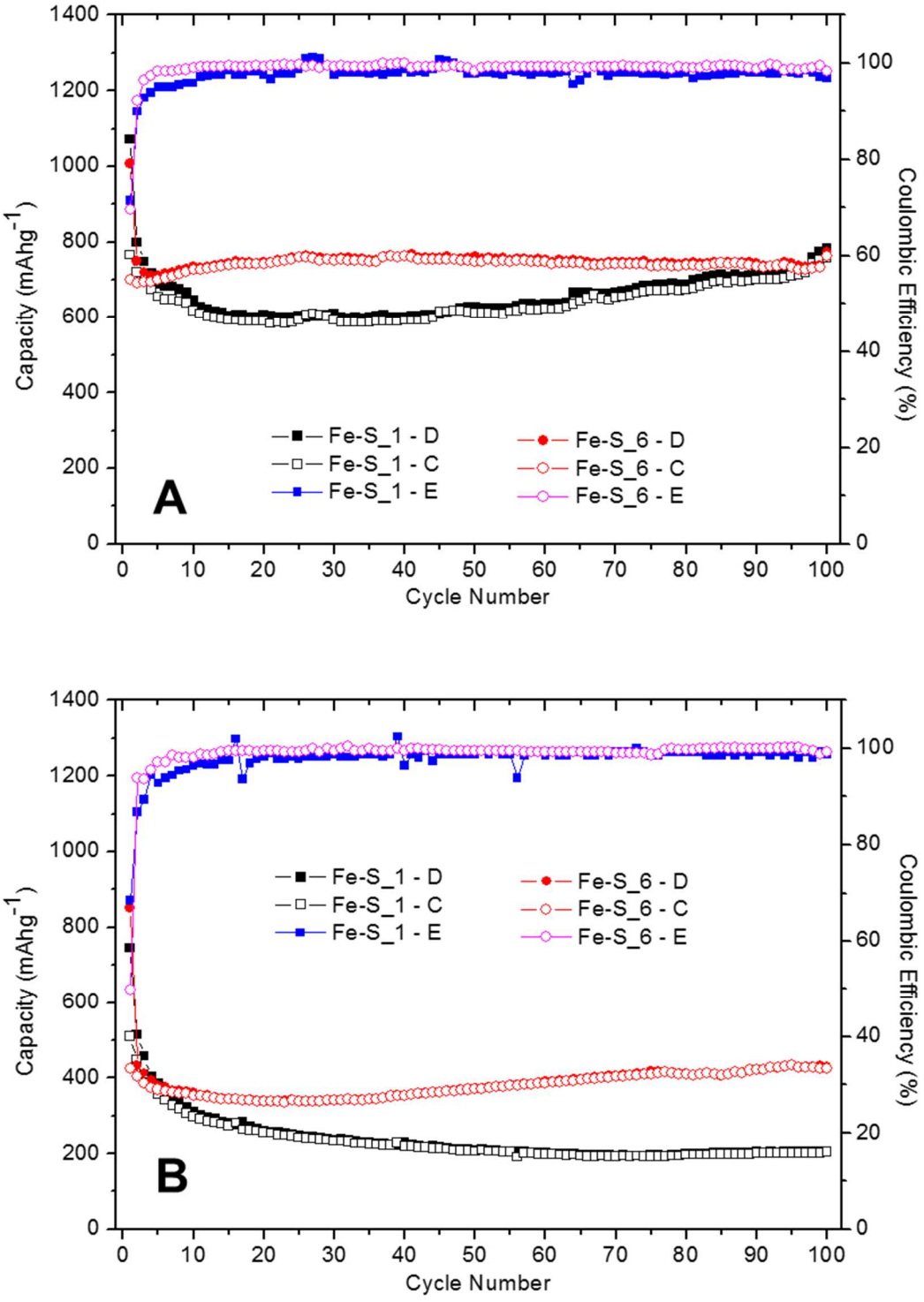

Figure 4.6: Cycling performance of the Fe-S_1 and Fe-S_6 electrodes at a current density of (A) 1 A g^{-1} and (B) 5 A g^{-1} between 0.001 and 3 V (*vs.* Li/Li^+). Fe-S_1 – D, Fe-S_1 – C and Fe-S_1 – E refers to the discharge and charge capacities and coulombic efficiency of Fe-S_1 respectively, while Fe-S_6 – D, Fe-S_6 – C and Fe-S_6 – E refers to the discharge and charge capacities and coulombic efficiency of Fe-S_6 correspondingly.

(890 mA h g^{-1}) when cycled at a current density of 0.1 A g^{-1}, 0.5 A g^{-1} and 1 A g^{-1}. (Figure 4.5 and Figure 4.6A).

From Figure 4.5A, it can be seen that, when cycled at a current density of 0.1 A g^{-1}, the discharge capacity of Fe-S_1 experienced a huge drop from 958 mA h g^{-1} (1^{st} cycle) to 761 mA h g^{-1} (2nd cycle) and slowly reduces to 677 mA h g^{-1} (5^{th} cycle), retaining 79% and 71% of its initial discharge capacity respectively. The discharge capacity of Fe-S_1 remains fairly constant from the 5^{th} (677 mA h g^{-1}) to the 25^{th} cycle (697 mA h g^{-1}), thereafter it slowly increases to reach a value of 927 mA h g^{-1} at its 50^{th} cycle, which is about 95% of its initial discharge capacity. This increase in capacity during the cycling of a working electrode has been observed in several literatures and was being attributed to an activation process. [38-42] It was also observed from Figure 4.5A that the discharge capacity of Fe-S_6 decreased by 32% from its initial capacity of 1199 mA h g^{-1} (1^{st} cycle) to reach a discharge capacity of 810 mA h g^{-1} for the 2^{nd} cycle when cycled at a current density of 0.1 A g^{-1}. From the 2^{nd} cycle to the 50^{th} cycle, Fe-S_6 exhibits a stable cycling performance where its discharge capacity is in the range of 810 mA h g^{-1} ± 5% i.e. 770 – 850 mA h g^{-1}. After 50 charge-discharge cycles, Fe-S_6 delivered a discharge capacity of 833 mA h g^{-1}, retaining 69% of its initial discharge capacity.

In its first cycle when cycled at 0.1 A g^{-1}, $Fe_{1-x}S$ attained a discharge capacity of 958 mA h g^{-1}, a charge capacity of 724 mA h g^{-1} and, hence, a coulombic efficiency of 75.6%. This low initial coulombic efficiency of is a result of the irreversible formation of an SEI layer. At the second cycle, the $Fe_{1-x}S$ electrode exhibited a discharge capacity of 761 mA h g^{-1}, a charge capacity of 682 mA h g^{-1} and a high coulombic efficiency of 89.6 %. From the second to the 50^{th} cycle, the $Fe_{1-x}S$ electrode achieved an average coulombic efficiency of about 97.7% when cycled at a current density of 0.1 A g^{-1} (Figure 4.5A). On the other hand, FeS_2 displayed an initial discharge capacity of 1199 mA h g^{-1}, an initial charge capacity of 798 mA h g^{-1} and an initial coulombic efficiency of 66.5% when cycled at 0.1 A g^{-1}. At its second cycle, a discharge capacity of 810 mA h g^{-1}, charge capacity of 770 mA h g^{-1} and high coulombic efficiency of 95.1% is achieved by the FeS_2 electrode. From the second to the 50^{th} cycle, the FeS_2 electrode

exhibited an average coulombic efficiency of about 99.1% when cycled at a current density of 0.1 A g^{-1}.

Figure 4.5B shows the capacity of Fe-S_1 and Fe-S_6 against the cycle number when the cells are cycled at a current density of 0.5 A g^{-1}. It can be seen from the plot that Fe-S_1 has an initial discharge capacity of 1127 mA h g^{-1}, which drops to 800 mA h g^{-1} in the 2nd cycle. Following, the discharge capacity of Fe-S_1 slowly decreases from 779 mA h g^{-1} (3rd cycle) to 658 mA h g^{-1} (10th cycle) and remains fairly constant till the 50th cycle. At the 50th cycle, Fe-S_1 delivered a reversible capacity of 688 mA h g^{-1}, retaining more than 60% of its initial capacity. From Figure 4.5B, Fe-S_6 is also observed to demonstrate good cycling performance when cycled at a current density of 0.5 A g^{-1}. It delivered an initial discharge capacity of 1021 mA h g^{-1} and, at the second cycle, attained a discharge capacity of 768 mA h g^{-1}, which is 75% of its initial capacity. Upon further cycling, Fe-S_6 exhibits a discharge capacity of around 730 mA h g^{-1} up to the 50th cycle. At the 50th cycle, it achieved a discharge capacity of 744 mA h g^{-1}, retaining 73% of its initial discharge capacity at the 50th cycle.

From Figure 4.5B, it can be seen that $Fe_{1-x}S$ attained a discharge capacity of 1127 mA h g^{-1}, charge capacity of 788 mA h g^{-1} and, therefore, a coulombic efficiency of 70.0% in its first cycle when cycled at 0.5 A g^{-1}. At the second cycle, this electrode exhibited a discharge capacity of 800 mA h g^{-1}, charge capacity of 730 mA h g^{-1} and a high coulombic efficiency of 91.3%. From the second to the 50th cycle, the $Fe_{1-x}S$ electrode achieved an average coulombic efficiency of about 98.8% when cycled at a current density of 0.5 A g^{-1}. As shown in Figure 4.5B, FeS_2 displayed an initial discharge capacity of 1021 mA h g^{-1}, charge capacity of 735 mA h g^{-1} and coulombic efficiency of 72.0% when cycled at 0.5 A g^{-1}. At its second cycle, a discharge and charge capacity of 768 mA h g^{-1} and 719 mA h g^{-1} and high coulombic efficiency of 93.6% is achieved by the FeS_2 electrode. From the second to the 50th cycle, the FeS_2 electrode displayed an average coulombic efficiency as high as 99.9% when cycled at a current density of 0.5 A g^{-1}.

To study the cycling capability of pyrrhotite $Fe_{1-x}S$ (Fe-S_1) and pyrite FeS_2 (Fe-S_6) at fast rates, the battery cells were subjected to galvanostatic charging and discharging

at a higher current density of 1 A g^{-1} and the results are presented in Figure 4.6A. It can be seen that Fe-S_1 delivered a discharge capacity of 1072 mA h g^{-1} and 799 mA h g^{-1} for the first and second cycle respectively, exhibiting an irreversible capacity of 273 mA h g^{-1}. The discharge capacity of this sample slowly decreases to a value of 608 mA h g^{-1} at the 30th cycle and starts to increase gradually. Eventually, Fe-S_1 delivered a discharge capacity of 784 mA h g^{-1} at the 100th cycle, retaining 73% of its initial discharge capacity. As shown in Figure 4.6A, Fe-S_6 also demonstrated good cycling performance, with an initial discharge capacity of 1007 mA h g^{-1} and a discharge capacity of 749 mA h g^{-1} at the second cycle, corresponding to an irreversible capacity of 258 mA h g^{-1}. The discharge capacity of this sample remains fairly constant from the 2nd to the 100th cycle, with a difference of less than 65 mA h g^{-1} between the maximum and minimum discharge capacity value. After undergoing 100 charging-discharging cycles, Fe-S_6 delivered a discharge capacity of 775 mA h g^{-1}, keeping 77% of its initial discharge capacity.

When cycled at 1 A g^{-1}, $Fe_{1-x}S$ attained a discharge capacity of 1072 mA h g^{-1}, charge capacity of 766 mA h g^{-1} and coulombic efficiency of 71.4% in its first cycle. A discharge capacity of 799 mA h g^{-1}, charge capacity of 719 mA h g^{-1} and coulombic efficiency of 89.9% was exhibited at its second cycle. From the second to the 100th cycle, the $Fe_{1-x}S$ electrode achieved an average coulombic efficiency of about 97.7% when cycled at a current density of 1 A g^{-1}. From Figure 4.6A, it can be seen that the FeS_2 displayed an initial discharge capacity of 1007 mA h g^{-1}, charge capacity of 701 mA h g^{-1} and coulombic efficiency of 69.6% when cycled at 1 A g^{-1}. At its second cycle, a discharge and charge capacity of 749 mA h g^{-1} and 691 mA h g^{-1} and high coulombic efficiency of 92.2% was achieved. From the second to the 100th cycle, the FeS_2 electrode obtained an average coulombic efficiency of 99.1% when cycled at a current density of 1 A g^{-1}.

Fe-S_1 and Fe-S_6 were also examined for their cycling performance at a high current density of 5 A g^{-1} and the results are presented in Figure 4.6B. It can be seen from the figure that Fe-S_1 has a discharge capacity of 746 mA h g^{-1} and 515 mA h g^{-1} for the first and second cycle, exhibiting an irreversible capacity of 231 mA h g^{-1}. The discharge capacity of this sample gradually drops to 200 mA h g^{-1} at the 50th cycle and stabilizes around this value up to the 100th cycle. At the 100th cycle, Fe-S_1 displayed

a discharge capacity of 207 mA h g^{-1}, retaining 28% of its initial discharge capacity. As presented in Figure 4.6B, Fe-S_6 displayed a better cycling performance than Fe-S_1, with an initial discharge capacity of 852 mAhg^{-1} and a discharge capacity of 432 mA h g^{-1} at the second cycle, which corresponds to a large irreversible capacity of 420 mA h g^{-1}. From the 3rd to the 100th cycle, this sample delivered a fairly stable discharge capacity that averages around 380 mA h g^{-1}. After 100 cycles, Fe-S_6 retained 50% of its initial discharge capacity, exhibiting a discharge capacity of 429 mA h g^{-1}.

As observed in Figure 4.6B, $Fe_{1-x}S$ displayed a discharge capacity of 746 mA h g^{-1}, charge capacity of 511 mA h g^{-1} and, hence, a coulombic efficiency of 68.5% in its first cycle when cycled at a high current density of 5 A g^{-1}. At the second cycle, this electrode exhibited a discharge capacity of 515 mA h g^{-1}, charge capacity of 447 mA h g^{-1} and a coulombic efficiency of 86.8%. From the second to the 100th cycle, the $Fe_{1-x}S$ electrode achieved an average coulombic efficiency of about 98.1% when cycled at a current density of 5 A g^{-1}. On the other hand, FeS_2 is observed to exhibit an initial discharge capacity of 852 mA h g^{-1}, charge capacity of 425 mA h g^{-1} and a low coulombic efficiency of 49.9% when cycled at 5 A g^{-1}. A discharge and charge capacity of 432 mA h g^{-1} and 406 mA h g^{-1} and high coulombic efficiency of 93.9% is achieved by the FeS_2 electrode at its second cycle. From the second to the 100th cycle, the FeS_2 electrode displayed a high average coulombic efficiency of 99.3% when cycled at a current density of 5 A g^{-1}.

Table 4.1 shows a summary of the battery cycling performance of pyrrhotite $Fe_{1-x}S$ and pyrite FeS_2 at various current densities. It can be seen from the table that both the iron sulfide samples exhibit good performance when cycled at low to slightly high current densities of 0.1 A g^{-1}, 0.5 A g^{-1} and 1 A g^{-1}, obtaining a discharge capacity of above 598 mA h g^{-1} for pyrrhotite $Fe_{1-x}S$ and above 712 mA h g^{-1} for pyrite FeS_2 for the first 50 cycles. When cycled at a high current density of 5 A g^{-1}, pyrrhotite $Fe_{1-x}S$ and pyrite FeS_2 displayed good cycling stability but the discharge capacity is not particularly high. At the 100th cycle, pyrrhotite $Fe_{1-x}S$ only delivered a discharge capacity of 207 mA h g^{-1} while pyrite FeS_2 delivered a discharge capacity of 429 mA h g^{-1}.

As seen from Table 4.1, pyrite FeS_2 exhibit better lithium storage capability than pyrrhotite $Fe_{1-x}S$. For the first 50 cycles, pyrite FeS_2 achieved a discharge capacity of

at least 773 mA h g^{-1}, 722 mA h g^{-1}, 712 mA h g^{-1} and 339 mA h g^{-1} when cycled at a current density of 0.1 A g^{-1}, 0.5 A g^{-1}, 1 A g^{-1} and 5 A g^{-1} respectively. On the other hand, pyrrhotite $Fe_{1-x}S$ attained a lower minimum discharge capacity of 627 mA h g^{-1}, 636 mA h g^{-1}, 598 mA h g^{-1} and 210 mA h g^{-1} for the first 50 cycles when cycled at a current density of 0.1 A g^{-1}, 0.5 A g^{-1}, 1 A g^{-1} and 5 A g^{-1} correspondingly.

Table 4.1: Summary of cycling performance of pyrrhotite $Fe_{1-x}S$ and pyrite FeS_2 at various current densities.

Current Density (A g^{-1})		Pyrrhotite $Fe_{1-x}S$ (Fe-S_1)				Pyrite FeS_2 (Fe-S_6)			
		0.1	0.5	1.0	5.0	0.1	0.5	1.0	5.0
Discharge Capacity at Various Cycle (mA h g^{-1})	Cycle 1	958	1127	1072	746	1199	1021	1007	852
	Cycle 2	761	800	799	515	810	768	749	432
	Cycle 50	889	688	626	210	833	744	762	373
	Cycle 100	-	-	784	207	-	-	775	429
Capacity Retention at Various Cycle (%)	Cycle 2	79	71	75	69	68	75	74	51
	Cycle 50	93	61	58	28	69	73	76	44
	Cycle 100	-	-	73	28	-	-	77	50
Maximum Capacity For The First 50 Cycles (mA h g^{-1})		958	1127	1072	746	1199	1021	1007	852
Minimum Capacity For The First 50 Cycles (mA h g^{-1})		627	636	598	210	773	722	712	339

From Table 4.1, it can be observed that pyrite FeS_2 exhibits better cycling stability than pyrrhotite $Fe_{1-x}S$ when cycled at higher current densities. When cycled at a current density of 0.5 A g^{-1}, pyrite FeS_2 retained 73% of its initial discharge capacity at the 50th cycle while pyrrhotite $Fe_{1-x}S$ only retained 61%. At a current density of 1 A g^{-1}, pyrite FeS_2 preserved 76% and 77% of its initial discharge capacity at the 50th and 100th cycle respectively while pyrrhotite $Fe_{1-x}S$ only managed to maintain 58% and 73% of its initial discharge capacity at the 50th and 100th cycle correspondingly. Even when the current density is increased to 5 A g^{-1}, pyrite FeS_2 still retained 44% and 50% of its initial discharge capacity at the 50th and 100th cycle respectively whereas pyrrhotite $Fe_{1-x}S$ only retained 28% of its initial discharge capacity at both the 50th and 100th cycle. Although it can be seen from Table 4.1 that pyrrhotite $Fe_{1-x}S$ retained a higher percentage (93%) of its initial discharge capacity than pyrite FeS_2 (69%) at the 50th cycle, it is not difficult to observe from Figure 4.5A that pyrite FeS_2 exhibits a more stable cycling performance with the discharge capacity in the range of 810 mA h g^{-1} ± 5% for the 2nd to the 50th cycle. On the other hand, pyrrhotite $Fe_{1-x}S$ displayed a larger difference with the discharge capacity in the range of 758 mA h g^{-1} ± 18% for the 2nd to the 50th cycle.

To make lithium ion batteries that have high power and can undergo fast charging, it is essential for the electrode to have good rate capability. Hence, the cycling performance of the two iron sulfide electrodes at numerous current densities were examined and the results are depicted in Figure 4.7. From this figure, it can be seen that the pyrrhotite $Fe_{1-x}S$ electrode (Fe-S_1**)** exhibits fairly good cycling performance when cycled at varying current densities in a voltage window of 0.001 – 3 V. When subjected to galvanostatic cycling at a current density 0.1 A g^{-1}, 0.2 A g^{-1}, 0.5 A g^{-1}, 1 A g^{-1}, 0.2 A g^{-1}, and 5 A g^{-1}, the pyrrhotite $Fe_{1-x}S$ electrode acheived a discharge capacity of around 660 mA h g^{-1}, 660 mA h g^{-1}, 640 mA h g^{-1}, 600 mA h g^{-1}, 570 mA h g^{-1} and 200 mA h g^{-1} respectively. Pyrite FeS_2 (Fe-S_6), on the other hand, demonstrated an even better cycling performance than the pyrrhotite $Fe_{1-x}S$ electrode, where it attained a discharge capacity of approximately 800 mA h g^{-1}, 740 mA h g^{-1}, 730 mA h g^{-1}, 730 mA h g^{-1}, 730 mA h g^{-1} and 390 mA h g^{-1} when charged and discharged at a current density 0.1 A g^{-1}, 0.2 A g^{-1}, 0.5 A g^{-1}, 1 A g^{-1}, 2 A g^{-1}, and 5 A g^{-1} correspondingly. It is obvious from Figure 4.7 that pyrite FeS_2 has a better lithium storage performance than pyrrhotite

$Fe_{1-x}S$ when subjected to galvanostatic charging and discharging at varying current densities from 0.1 – 5 A g^{-1}.

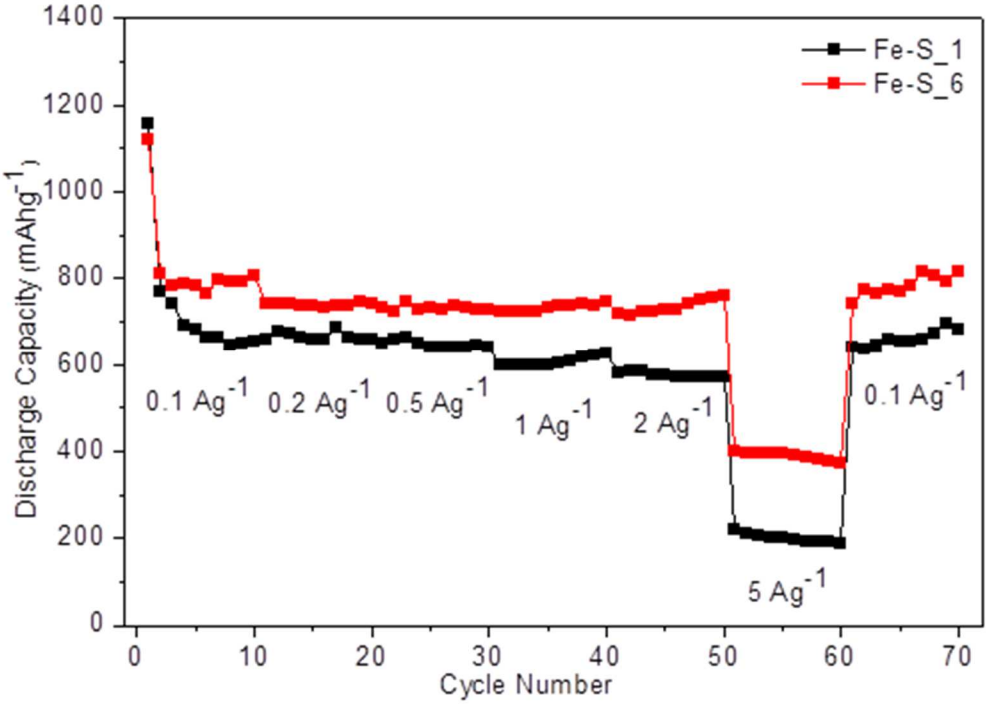

Figure 4.7: Cycling performance of the Fe-S_1 and Fe-S_6 electrodes at various current densities between 0.001 and 3 V (*vs.* Li/Li^+).

To gain an insight into why pyrite FeS_2 exhibits better lithium storage performance i.e. higher capacity and superior cycling stability than pyrrhotite $Fe_{1-x}S$, it is essential to understand the reaction between lithium ions and these two iron sulfide electrodes during cycling. Hence, the galvanostatic discharge (Li ion insertion) and charge (Li ion extraction) voltage profiles for both electrodes when cycled between 0.001 and 3 V (*vs.* Li/Li^+) at a low current density of 0.1 A g^{-1} is plotted and depicted in Figure 4.8. Cyclic voltammetry (CV) of the pyrrhotite $Fe_{1-x}S$ and pyrite FeS_2 electrodes (Figure 4.9) were also performed under ambient temperature in a voltage window of 0.001 – 3 V (*vs.* Li/Li^+) and at a scan rate of 0.2 mV s^{-1} to understand the reaction between the Li^+ ions and the iron sulfide electrodes during lithiation and delithiation process.

From Figure 4.8, it can be seen that, when cycled at 0.1 A g^{-1} in the voltage window of 0.001 – 3 V (*vs.* Li/Li^+), there is only one long plateau at 1.34 V for pyrrhotite $Fe_{1-x}S$ and at 1.49 V for pyrite FeS_2 in the first cycle galvanostatic discharge curve. This single flat plateau is assigned to a couple of reactions involving the reduction of iron sulfide into iron, lithium sulfide and lithium-rich phases, suggesting that these reactions could have occurred simultaneously due to the slow diffusion of Li^+ into the iron sulfides at ambient temperature i.e. ≤ 30 °C. [43-46] For the pyrrhotite $Fe_{1-x}S$ electrode, only one plateau (≈ 1.82 V) that is associated to the oxidation of Fe to $Li_{2-x}FeS_2$ ($0 \leq x < 0.8$) is observed in its first cycle charge curve. [33, 46] On the other hand, pyrite FeS_2 exhibits two platforms at around 1.82 V and 2.48 V in its first cycle charge curve, which are ascribed to the formation of $Li_{2-x}FeS_2$ ($0 \leq x < 0.8$), FeS_y, Li and S. [43, 47] It is observed from Figure 4.8 that, unlike the first cycle where they only have one discharge plateau, both pyrrhotite $Fe_{1-x}S$ and pyrite FeS_2 have two discharge platforms in their second cycle, indicating that these two electrodes undergo a change in their lithium storage mechanism. From the 2^{nd} to the 50^{th} cycle, the two iron sulfide electrodes exhibit similar discharge profiles, suggesting that they undergo similar reactions during discharging. There is no or little change in the electrode reaction for both iron sulfides during charging as implied by the similar charge profile as that for their respective initial charging process. It is well-known that polarization in LIB can occur due to a delay in the transfer of lithium ions and electrons at the interface between the active material and electrolyte. [30, 44] From the voltage difference between the discharge and charge plateaus in the voltage profiles for the two iron sulfide electrodes (Figure 4.8), it can be seen that the pyrite FeS_2 electrode has a lower polarization and, therefore, a better electron and Li^+ ion transport at the interface between the active material and electrolyte than the pyrrhotite $Fe_{1-x}S$ electrode.

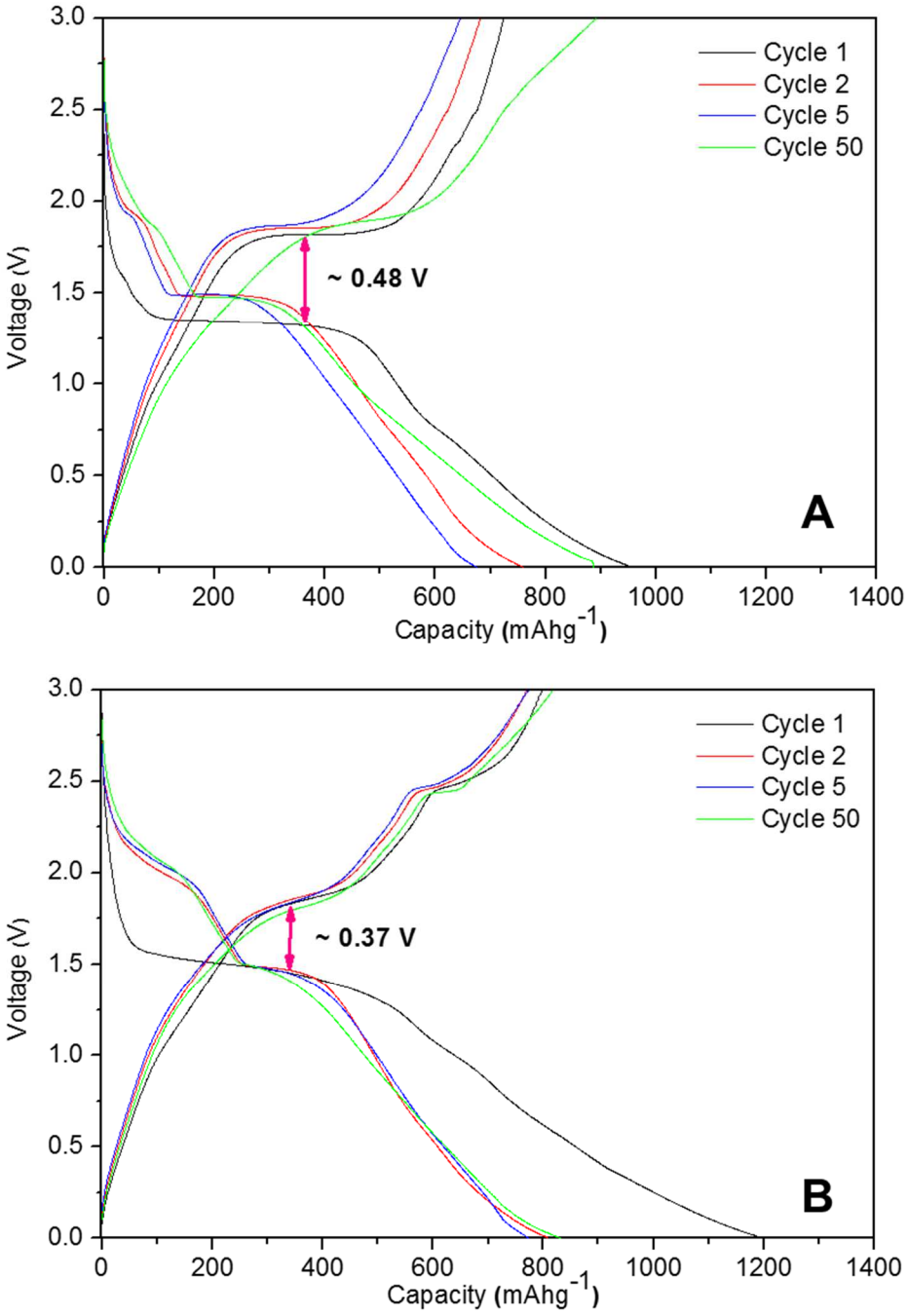

Figure 4.8: Galvanostatic charge/discharge voltage profiles of the (A) Fe-S_1 and (B) Fe-S_6 electrodes when cycled at a current density of 0.1 A g^{-1} between 0.001 and 3 V (*vs.* Li/Li^+).

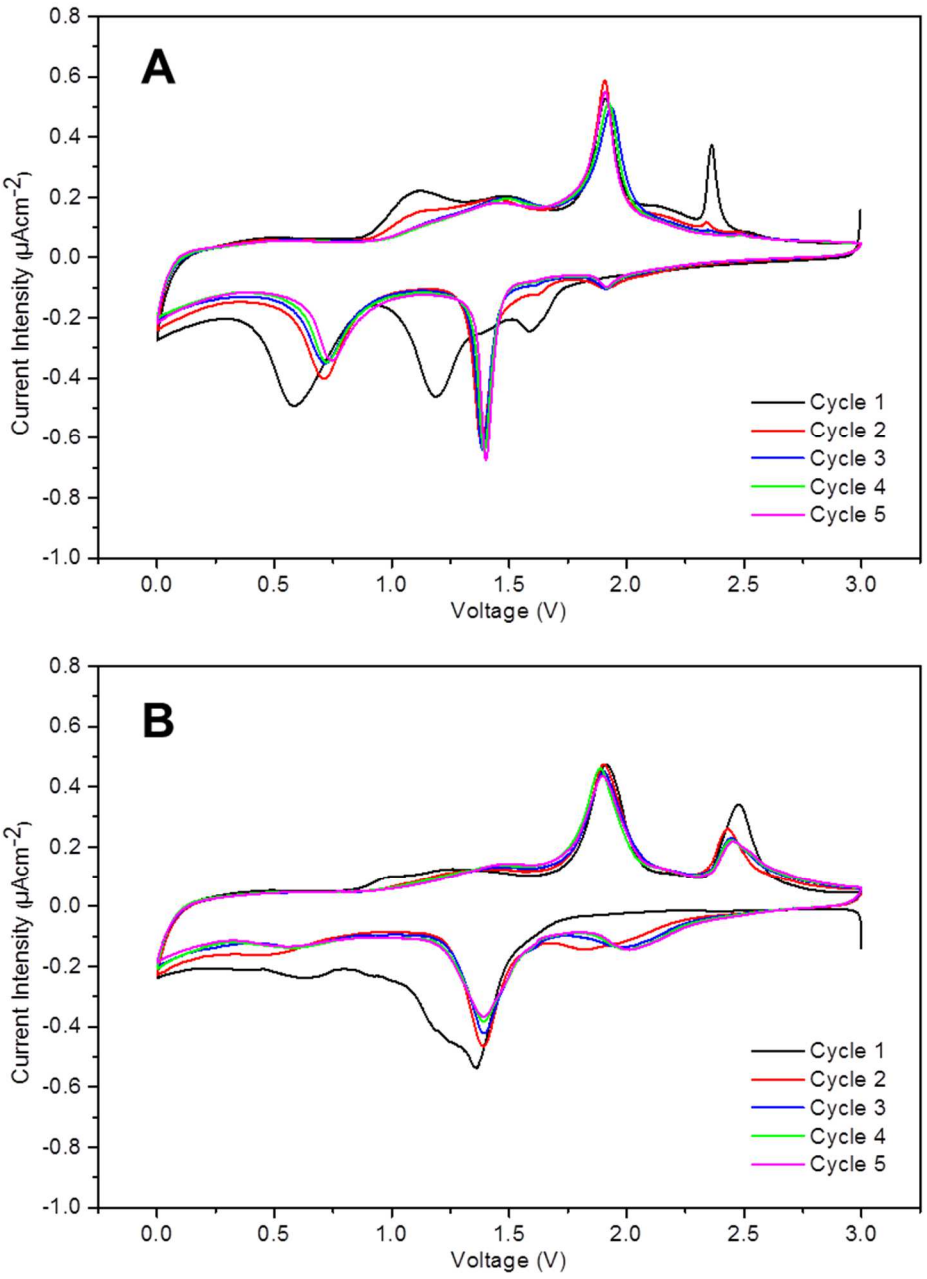

Figure 4.9: Cyclic voltammetry of (A) Fe-S_1 and (B) Fe-S_6 electrode recorded under ambient temperature in the voltage range of 0.001 – 3 V (*vs.* Li/Li^+) at a constant scan rate of 0.2 mV s^{-1}.

$$2\,Fe_{1-x}S + 2\,Li^+ + 2\,e^- \longrightarrow Li_2FeS_2 + (1-2x)\,Fe$$

Equation 4.1

$$Fe_{1-x}S + 2\,Li^{+} + 2\,e^{-} \longrightarrow Li_2S + (1-x)\,Fe$$

Equation 4.2

Figure 4.9 shows the CV curve for the first five cycles of the pyrrhotite $Fe_{1-x}S$ and pyrite FeS_2 electrodes performed under ambient temperature in a voltage window of 0.001 – 3 V (*vs.* Li/Li^+) and at a scan rate of 0.2 mV s^{-1}. From Figure 4.9A, it can be seen that there are three reduction peaks in the first cycle CV of the pyrrhotite $Fe_{1-x}S$ electrode. The peaks centred at 1.58 V and 1.18 V are attributed to the lithiation of pyrrhotite $Fe_{1-x}S$ according to the reactions stated in Equation 4.1 and Equation 4.2 respectively, while that at around 0.58 V is mainly ascribed to the formation of a polymeric solid/electrolyte interphase (SEI) layer on the surface of the electrode. [48-51] A sharp oxidation peak at around 1.91 V, which can be associated to the delithiation process to form $Li_{2-x}FeS_2$ where $0 \leq x < 0.8$ (Equation 4.3 and Equation 4.4) and another at 2.36 V which is attributed to the formation of FeS_y (Equation 4.5) were also observed in the first cycle CV of the pyrrhotite $Fe_{1-x}S$ electrode. [33, 47]

$$Fe + 2\,Li_2S \longrightarrow Li_2FeS_2 + 2\,Li^{+} + 2\,e^{-}$$

Equation 4.3

$$Li_2FeS_2 \longrightarrow Li_{2-x}FeS_2 + x\,Li^{+} + x\,e^{-} \qquad (0 < x < 0.8)$$

Equation 4.4

$$Li_{2-x}FeS_2 \longrightarrow FeS_y + (2-y)\,S + (2-x)\,Li^{+} + (2-x)e^{-}$$

Equation 4.5

From Figure 4.9B, a reduction peak at around 1.35 V can be observed in the first cycle CV for pyrite FeS_2 which corresponds to the lithiation of pyrite FeS_2 via an intercalation (Equation 4.6) and conversion (Equation 4.7) reaction. [52, 53] These initial lithiation reactions are similar to that for $Fe_{1-x}S$ and result in the same final products – Fe and Li_2S. The reduction peak at approximately 0.62 V in the first cycle CV for pyrite FeS_2, like that at 0.58 V in the initial CV for $Fe_{1-x}S$, is attributed to the formation of a polymeric SEI layer on the surface of the electrode. It was also observed that pyrite FeS_2 undergoes a similar oxidation reaction as pyrrhotite $Fe_{1-x}S$ in the first cycle CV, with the oxidation peak at 1.91 V corresponding to the electrode reactions in Equation 4.3 and Equation 4.4 to form $Li_{2-x}FeS_2$ where $0 \leq x < 0.8$, and that at 2.47 V attributed to the oxidation of $Li_{2-x}FeS_2$ to form FeS_y (Equation 4.5). [43, 45]

$$FeS_2 + 2\,Li^+ + 2\,e^- \longrightarrow Li_2FeS_2$$

Equation 4.6

$$Li_2FeS_2 + 2\,Li^+ + 2\,e^- \longrightarrow Fe + 2\,Li_2S$$

Equation 4.7

From the second cycle onwards, the subsequent CV curves for the pyrrhotite $Fe_{1-x}S$ and pyrite FeS_2 electrodes shared several similar peaks (Figure 4.9). Both electrodes have a reduction peak in the range of 1.8 – 2.0 V which can be assigned to the lithiation of FeS_y to form Li_2FeS_2 (Equation 4.8). [47] A reduction peak at around 1.4 V is also present from the second to the fifth CV cycle for both iron sulfide electrodes, where it is associated to the lithiation of $Li_{2-x}FeS_2$ and Li_2FeS_2 to Fe and Li_2S (Equation 4.9 and Equation 4.7). [30, 50, 52, 53] As with the first cycle CV, both pyrite FeS_2 and pyrrhotite $Fe_{1-x}S$ have a sharp and obvious oxidation peak at around 1.9 V corresponding to the electrode reactions in Equation 4.3 and Equation 4.4 in their second to fifth CV cycles.

$$FeS_y + (2-y)\,S + 2\,Li^+ + 2\,e^- \longrightarrow Li_2FeS_2$$

Equation 4.8

$$Li_{2-x}FeS_2 + x\,Li^+ + x\,e^- \longrightarrow Li_2FeS_2$$

Equation 4.9

Besides the similarities, there are several differences between the electrode reactions for these two iron sulfides during galvanostatic discharging and charging cycling. For pyrrhotite $Fe_{1-x}S$, there is a reduction peak present at around 0.7 V from its second to fifth CV cycles which is not observed in that for pyrite FeS_2. This peak, though slightly shifted (by ≈ 0.12 V) compared to the reduction peak in its first cycle, is also essentially ascribed to the formation of the SEI layer. Another major difference between the CV curves for these two electrodes lies in the oxidation peak at approximately 2.4 V. As observed in Figure 4.9, this oxidation peak, which is linked to the formation of FeS_y (Equation 4.5), is present in the first five CV cycles for the pyrite FeS_2 electrode. However, for the pyrrhotite $Fe_{1-x}S$ electrode, the intensity of this peak is found to decrease largely from the first CV cycle to the second CV cycle and, eventually, it disappeared from the CV curve for the pyrrhotite $Fe_{1-x}S$ electrode from the third cycle onwards. In fact, the intensity of the peak (1.8 – 2.0 V) corresponding to the reduction of FeS_y to form Li_2FeS_2 (Equation 4.8) is much smaller in the reduction scan for the pyrrhotite $Fe_{1-x}S$ electrode than for the pyrite FeS_2 electrode. This shows that, while the lithiation (Equation 4.8) and delithiation (Equation 4.5) of iron sulfide (FeS_y) is very reversible for the pyrite FeS_2 electrode, this reaction is only reversible for the first two cycles of the pyrrhotite $Fe_{1-x}S$ electrode.

From the galvanostatic cycling of the iron sulfide electrodes in Figure 4.5, Figure 4.6 and Figure 4.7, it was found that pyrite FeS_2 exhibits better lithium storage performance than pyrrhotite $Fe_{1-x}S$. Since the nitrogen adsorption/desorption measurement shows that the two iron sulfide samples have similar surface area, where the $Fe_{1-x}S$ sample

have a Brunauer−Emmett−Teller (BET) surface area of 13.4 $m^2 g^{-1}$ and the FeS_2 sample have a BET surface area of 14.2 $m^2 g^{-1}$ (Figure A.1), this difference in lithium storage performance should not be due to the difference in surface area between these two samples. From the analysis of the voltage profiles in Figure 4.8 and the CV curves in Figure 4.9, it can be seen that the two iron sulfide electrodes generally undergo similar electrode reactions during lithiation and delithiation. However, it can be seen from the CV curves that, while the lithiation and delithiation of FeS_y is reversible for the pyrite FeS_2 electrode, this reaction has limited reversibility in the pyrrhotite $Fe_{1-x}S$ electrode. Furthermore, the pyrite FeS_2 electrode is found to have a lower polarization than the pyrrhotite $Fe_{1-x}S$ electrode, as shown by the smaller voltage difference between the discharge and charge plateaus in its voltage profiles. Therefore, this higher capacity and superior cycling stability of pyrite FeS_2 compared to $Fe_{1-x}S$ can be attributed to two main reasons:

(1) The lower polarization and, therefore, better electron and Li^+ ion transport at the interface between the active material and electrolyte at the pyrite FeS_2 electrode than the pyrrhotite $Fe_{1-x}S$ electrode.

(2) The reversible lithiation and delithiation of iron sulfide (FeS_y) during the galvanostatic cycling of the pyrite FeS_2 electrode.

4.4 Conclusion

In summary, pyrrhotite $Fe_{1-x}S$ and pyrite FeS_2 with good purity have been successfully synthesized via a solution-based chemical synthesis method. Pure samples of these two iron sulfides were obtained simply by varying the mole ratio between the anhydrous $FeCl_2$ and elemental S that were used as the starting materials in the synthesis. From the experiments, it was found that iron sulfides such as $Fe_{1-x}S$, FeS, Fe_3S_4, FeS_2 or a mixture of them will be formed under sulfur-limiting conditions i.e an Fe:S precursor molar ratio of 1:1 or 1:2. Pure pyrite FeS_2 phase can only be formed when excess S is present in the reaction mixture i.e. an Fe:S precursor molar ratio of 1:4 or 1:6. A

possible reaction pathway for the formation of the pyrrhotite $Fe_{1-x}S$ and pyrite FeS_2 from $FeCl_2$ and elemental S precursors was proposed.

The electrochemical properties of the as-synthesized pyrrhotite $Fe_{1-x}S$ and pyrite FeS_2 were characterized and it was found that pyrite FeS_2 exhibits better lithium storage capability than pyrrhotite $Fe_{1-x}S$. For the first 50 cycles, pyrite FeS_2 achieved a discharge capacity of at least 773 mA h g^{-1}, 722 mA h g^{-1}, 712 mA h g^{-1} and 339 mA h g^{-1} when cycled at a current density of 0.1 A g^{-1}, 0.5 A g^{-1}, 1 A g^{-1} and 5 A g^{-1} respectively. On the other hand, pyrrhotite $Fe_{1-x}S$ attained a lower minimum discharge capacity of 627 mA h g^{-1}, 636 mA h g^{-1}, 598 mA h g^{-1} and 210 mA h g^{-1} for the first 50 cycles when cycled at a current density of 0.1 A g^{-1}, 0.5 A g^{-1}, 1 A g^{-1} and 5 A g^{-1} correspondingly. The superior lithium storage performance of pyrite FeS_2 compared to pyrrhotite $Fe_{1-x}S$ can be attributed to: (1) the lower polarization, better electron and Li^+ ion transport at the interface between the active material and electrolyte at the pyrite FeS_2 electrode than the pyrrhotite $Fe_{1-x}S$ electrode and (2) the reversible lithiation and delithiation of iron sulfide (FeS_y) during the galvanostatic cycling of the pyrite FeS_2 electrode.

This is a first attempt to study the effect of how the number of sulfide ion in the stoichiometry of an iron sulfide compound (a conversion-typed compound) i.e. Fe:S = 1:1 (FeS) or 1:2 (FeS_2) affects its lithium storage properties. It should be highlighted that care was taken to ensure that the two iron sulfide compounds were synthesized using the same precursors and surfactant to eliminate any possible effect due to the remaining surfactant on the as-synthesized particles. The fact that the synthesized $Fe_{1-x}S$ and FeS_2 particles do not have any fanciful morphologies eradicated the possible effect of particle morphology on the lithium storage performance of the two iron sulfide samples and made this a fairer comparison since the morphology and surface area of the iron sulfide particles have great impact on its lithium storage performance, as mentioned in Section 2.4.1.

References:

1. Sourisseau, C., Cavagnat, R., and Fouassier, M., *The vibrational properties and valence force-fields of FeS2, RuS2 pyrites and FeS2 marcasite.* Journal of Physics and Chemistry of Solids, 1991. **52**(3): p. 537.
2. Boughrict, A., Figueiredo, R.S., Laureyns, J., and Recourt, P., *Identification of newly generated iron phases in recent anoxic sediments: 57Fe Mossbauer and micro-Raman spectroscopic studies.* Journal of the Chemical Society - Faraday Transactions, 1997. **93**(17): p. 3209.
3. Breier, J.A., German, C.R., and White, S.N., *Mineral phase analysis of deep-sea hydrothermal particulates by a Raman spectroscopy expert algorithm: toward autonomous in situ experimentation and exploration.* Geochemistry Geophysics Geosystems, 2009. **10**.
4. Lutz, H.D. and Muller, B., *Lattice vibration spectra. LXVIII. single-crystal Raman spectra of marcasite-type iron chalcogenides and pnictides, FeX2 (X=S, Se, Te; P, As, Sb).* Physics and Chemistry of Minerals, 1991. **18**(4): p. 265.
5. Turcotte, S.B., Benner, R.E., Riley, A.M., Li, J., Wadsworth, M.E., and Bodily, D., *Application of Raman spectroscopy to metal-sulfide surface analysis.* Applied Optics, 1993. **32**(6): p. 935.
6. Kleppe, A.K. and Jephcoat, A.P., *High-pressure Raman spectroscopic studies of FeS2 pyrite.* Mineralogical Magazine, 2004. **68**(3): p. 433.
7. Bi, Y., Yuan, Y., Exstrom, C.L., Darveau, S.A., and Huang, J., *Air stable, photosensitive, phase pure iron pyrite nanocrystal thin films for photovoltaic application.* Nano Letters, 2011. **11**(11): p. 4953.
8. Vogt, H., Chattopadhyay, T., and Stolz, H.J., *Complete first-order Raman spectra of the pyrite structure compounds FeS2, MnS2 and SiP2.* Journal of Physics and Chemistry of Solids, 1983. **44**(9): p. 869.
9. Zhu, L., Richardson, B., Tanumihardja, J., and Yu, Q., *Controlling morphology and phase of pyrite FeS2 hierarchical particles via the combination of structure-direction and chelating agents.* CrystEngComm, 2012. **14**(12): p. 4188.

10. Mernagh, T.P. and Trudu, A.G., *A laser Raman microprobe study of some geologically important sulfide minerals.* Chemical Geology, 1993. **103**(1-4): p. 113.
11. Battaglia, T.M., Dunn, E.E., Lilley, M.D., Holloway, J., Dable, B.K., Marquardt, B.J., and Booksh, K.S., *Development of an in situ fiber optic Raman system to monitor hydrothermal vents.* Analyst, 2004. **129**(7): p. 602.
12. Gong, G.Q., Gupta, A., Xiao, G., Qian, W., and Dravid, V.P., *Magnetoresistance and magnetic properties of epitaxial magnetite thin films.* Physical Review B, 1997. **56**(9): p. 5096.
13. Liu, H.F., Huang, A., and Chi, D.Z., *Thermal annealing of nanocrystalline Fe3S4 films deposited on Si substrates by dc-magnetron sputtering at room temperature.* Journal of Physics D: Applied Physics, 2010. **43**(45): p. 455405.
14. Li, P., Xia, C., Zhang, Q., Guo, Z., Cui, W., Bai, H., Alshareef, H.N., and Zhang, X.X., *Fabrication and characterization of nanostructured Fe3S4, an isostructural compound of half-metallic Fe3O4.* Journal of Applied Physics, 2015. **117**(22): p. 223903.
15. Li, G., Zhang, B., Yu, F., Novakova, A.A., Krivenkov, M.S., Kiseleva, T.Y., Chang, L., Rao, J., Polyakov, A.O., Blake, G.R., De Groot, R.A., and Palstra, T.T.M., *High-purity Fe3S4 greigite microcrystals for magnetic and electrochemical performance.* Chemistry of Materials, 2014. **26**(20): p. 5821.
16. Pauling, L., *On the stability of the S(8) molecule and the structure of fibrous sulfur.* Proceedings of the National Academy of Sciences of the United States of America, 1949. **35**(9): p. 495.
17. Zumdahl, S.S., *Chemical principles*. 6th ed. 2009, Boston, Mass. : Abingdon : Houghton Mifflin.
18. Bartlett, P.D., Cox, E.F., and Davis, R.E., *Reactions of elemental sulfur. IV. Catalytic effects in the reaction of sulfur with triphenylphosphine.* Journal of the American Chemical Society, 1961. **83**(1): p. 103.
19. Cotton, F.A. and Wilkinson, G., *The Group VI elements: S, Se, Te, Po*, in *Advanced inorganic chemistry : a comprehensive text*. 1972, Interscience Publishers. p. 421-457.
20. Li, Z., Ji, Y.J., Xie, R.G., Grisham, S.Y., and Peng, X.G., *Correlation of CdS nanocrystal formation with elemental sulfur activation and its implication in*

synthetic development. Journal of the American Chemical Society, 2011. **133**(43): p. 17248.

21. Joo, J., Na, H.B., Yu, T., Yu, J.H., Kim, Y.W., Wu, F., Zhang, J.Z., and Hyeon, T., *Generalized and facile synthesis of semiconducting metal sulfide nanocrystals.* Journal of the American Chemical Society, 2003. **125**(36): p. 11100.
22. Cademartiri, L., Malakooti, R., O'Brien, P.G., Migliori, A., Petrov, S., Kherani, N.P., and Ozin, G.A., *Large-scale synthesis of ultrathin Bi2S3 necklace nanowires.* Angewandte Chemie-International Edition, 2008. **47**(20): p. 3814.
23. Lin, Y.Y., Wang, D.Y., Yen, H.C., Chen, H.L., Chen, C.C., Chen, C.M., Tang, C.Y., and Chen, C.W., *Extended red light harvesting in a poly(3-hexylthiophene)/iron disulfide nanocrystal hybrid solar cell.* Nanotechnology, 2009. **20**(40).
24. Kwon, S.G. and Hyeon, T., *Colloidal chemical synthesis and formation kinetics of uniformly sized nanocrystals of metals, oxides, and chalcogenides.* Accounts of Chemical Research, 2008. **41**(12): p. 1696.
25. Mourdikoudis, S. and Liz-Marzan, L.M., *Oleylamine in nanoparticle synthesis.* Chemistry of Materials, 2013. **25**(9): p. 1465.
26. Davis, R.E. and Nakshbendi, H.F., *Sulfur in amine solvents.* Journal of the American Chemical Society, 1962. **84**(11): p. 2085.
27. Thomson, J.W., Nagashima, K., Macdonald, P.M., and Ozin, G.A., *From sulfur-amine solutions to metal sulfide nanocrystals: peering into the oleylamine-sulfur black box.* Journal of the American Chemical Society, 2011. **133**(13): p. 5036.
28. Wilkin, R.T. and Barnes, H.L., *Pyrite formation by reactions of iron monosulfides with dissolved inorganic and organic sulfur species.* Geochimica et Cosmochimica Acta, 1996. **60**(21): p. 4167.
29. Hunger, S. and Benning, L.G., *Greigite: a true intermediate on the polysulfide pathway to pyrite.* Geochemical Transactions, 2007. **8**.
30. Liu, W.L., Rui, X.H., Tan, H.T., Xu, C., Yan, Q.Y., and Hng, H.H., *Solvothermal synthesis of pyrite FeS2 nanocubes and their superior high rate lithium storage properties.* RSC Advances, 2014. **4**(90): p. 48770.
31. Benning, L.G., Wilkin, R.T., and Barnes, H.L., *Reaction pathways in the Fe–S system below 100°C.* Chemical Geology, 2000. **167**(1–2): p. 25.

32. Kar, S., Mandal, S.K., Das, D., and Chaudhuri, S., *Wet chemical synthesis of iron pyrite and characterization by Mossbauer spectroscopy.* Materials Letters, 2004. **58**(22-23): p. 2886.

33. Wu, B., Song, H., Zhou, J., and Chen, X., *Iron sulfide-embedded carbon microsphere anode material with high-rate performance for lithium-ion batteries.* Chemical Communications, 2011. **47**(30): p. 8653.

34. Choi, D., Wang, W., and Yang, Z., *Material challenges and perspectives*, in *Lithium-ion batteries*. 2011, CRC Press. p. 1-50.

35. Fan, S.F., Sun, T., Rui, X.H., Yan, Q.Y., and Hng, H.H., *Cooperative enhancement of capacities in nanostructured SnSb/carbon nanotube network nanocomposite as anode for lithium ion batteries.* Journal of Power Sources, 2012. **201**: p. 288.

36. Li, H., Richter, G., and Maier, J., *Reversible formation and decomposition of LiF clusters using transition metal fluorides as precursors and their application in rechargeable Li batteries.* Advanced Materials, 2003. **15**(9): p. 736.

37. Laruelle, S., Grugeon, S., Poizot, P., Dolle, M., Dupont, L., and Tarascon, J.M., *On the origin of the extra electrochemical capacity displayed by MO/Li cells at low potential.* Journal of the Electrochemical Society, 2002. **149**(5): p. A627.

38. Zhu, J.X., Zhu, T., Zhou, X.Z., Zhang, Y.Y., Lou, X.W., Chen, X.D., Zhang, H., Hng, H.H., and Yan, Q.Y., *Facile synthesis of metal oxide/reduced graphene oxide hybrids with high lithium storage capacity and stable cyclability.* Nanoscale, 2011. **3**(3): p. 1084.

39. Yang, X., Chan, C.Y., Xue, H.T., Xu, J., Tang, Y.B., Wang, Q., Wong, T.L., and Lee, C.S., *One-pot synthesis of graphene/In2S3 nanoparticle composites for stable rechargeable lithium ion battery.* CrystEngComm, 2013. **15**(33): p. 6578.

40. Zhu, J., Yin, Z., Yang, D., Sun, T., Yu, H., Hoster, H.E., Hng, H.H., Zhang, H., and Yan, Q., *Hierarchical hollow spheres composed of ultrathin Fe2O3 nanosheets for lithium storage and photocatalytic water oxidation.* Energy & Environmental Science, 2013. **6**(3): p. 987.

41. Chen, M., Liu, J., Chao, D., Wang, J., Yin, J., Lin, J., Hong, J.F., and Ze, X.S., *Porous α-Fe2O3 nanorods supported on carbon nanotubes-graphene foam as superior anode for lithium ion batteries.* Nano Energy, 2014. **9**(0): p. 364.

42. Zheng, J., Cao, Y., Cheng, C., Chen, C., Yan, R.W., Huai, H.X., Dong, Q.F., Zheng, M.S., and Wang, C.C., *Facile synthesis of Fe3S4 hollow spheres with high-performance for lithium-ion batteries and water treatment.* Journal of Materials Chemistry A, 2014. **2**(46): p. 19882.

43. Fong, R., Dahn, J.R., and Jones, C.H.W., *Electrochemistry of pyrite‐based cathodes for ambient temperature lithium batteries.* Journal of The Electrochemical Society, 1989. **136**(11): p. 3206.

44. Zhang, D., Wang, X.L., Mai, Y.J., Xia, X.H., Gu, C.D., and Tu, J.P., *Enhanced electrochemical performance of FeS2 synthesized by hydrothermal method for lithium ion batteries.* Journal of Applied Electrochemistry, 2012. **42**(4): p. 263.

45. Liu, J., Wen, Y., Wang, Y., Van Aken, P.A., Maier, J., and Yu, Y., *Carbon-encapsulated pyrite as stable and earth-abundant high energy cathode material for rechargeable lithium batteries.* Advanced Materials, 2014. **26**(34): p. 6025.

46. Wang, C., Lan, M., Zhang, Y., Bian, H., Yuen, M.F., Ostrikov, K., Jiang, J., Zhang, W., Li, Y.Y., and Lu, J., *Fe1-xS/C nanocomposites from sugarcane waste-derived microporous carbon for high-performance lithium ion batteries.* Green Chemistry, 2016.

47. Xue, H., Yu, D.Y.W., Qing, J., Yang, X., Xu, J., Li, Z., Sun, M., Kang, W., Tang, Y., and Lee, C.S., *Pyrite FeS2 microspheres wrapped by reduced graphene oxide as high-performance lithium-ion battery anodes.* Journal of Materials Chemistry A, 2015. **3**(15): p. 7945.

48. Xing, C., Zhang, D., Cao, K., Zhao, S., Wang, X., Qin, H., Liu, J., Jiang, Y., and Meng, L., *In situ growth of FeS microsheet networks with enhanced electrochemical performance for lithium-ion batteries.* Journal of Materials Chemistry A, 2015. **3**(16): p. 8742.

49. Kim, Y. and Goodenough, J.B., *Delete.* The Journal of Physical Chemistry C, 2008. **112**(38): p. 15060.

50. Xu, C., Zeng, Y., Rui, X., Xiao, N., Zhu, J., Zhang, W., Chen, J., Liu, W., Tan, H., Hng, H.H., and Yan, Q., *Controlled soft-template synthesis of ultrathin C@FeS nanosheets with high-Li-storage performance.* Acs Nano, 2012. **6**(6): p. 4713.

51. Wang, X., Xiang, Q., Liu, B., Wang, L., Luo, T., Chen, D., and Shen, G., *TiO2 modified FeS nanostructures with enhanced electrochemical performance for lithium-ion batteries.* Scientific Reports, 2013. **3**: p. 2007.

52. Zhang, D., Wang, X.L., Mai, Y.J., Xia, X.H., Gu, C.D., and Tu, J.P., *Enhanced electrochemical performance of FeS 2 synthesized by hydrothermal method for lithium ion batteries.* Journal of Applied Electrochemistry, 2012. **42**(4): p. 263.

53. Huang, S., Liu, X., Li, Q., and Chen, J., *Pyrite film synthesized for lithium-ion batteries.* Journal of Alloys and Compounds, 2009. **472**(1-2): p. L9.

Chapter 5

Tin Sulfides and Their Lithium Storage Properties

This chapter presents the results on the synthesis of tin sulfides via a solution-based chemical synthesis method (procedures detailed in Section 3.1.2). The as-synthesized powders were characterized using X-ray diffraction and field emission scanning electron microscopy to determine their phase, purity, and morphology and particle size. Time-dependent reaction was carried out to understand the formation mechanism of the two tin sulfide phases. The effect of the tin to sulfur stoichiometric ratio of the as-synthesized tin sulfides on their lithium storage properties is also investigated and presented in this chapter. It was found that SnS_2 displayed a higher capacity and better cycling stability than SnS after prolonged cycling particularly at higher current densities and this is attributed to its chemical and structural properties. As evidenced by the higher discharge capacity attained from the intercalation and conversion reaction throughout the 100 cycles, more Li_2S is formed during the lithiation of SnS_2, thus providing a thicker layer to buffer the large volume change during the lithiation and delithiation of Sn. This can result in a reduction in the pulverization and better capacity retention of the electrode after prolonged cycling, as verified by the slower alloying capacity fading rate observed in the SnS_2 electrode compared to the SnS electrode.

5.1 Synthesis and Characterization of Tin Sulfide Particles and Their Formation Mechanism

To obtain pure phases of the different tin sulfides, four different pots of reaction were carried out with all parameters kept constant except for the reaction time. The experimental parameters and procedures were detailed in Section 3.1.2, where the powder synthesized after a reaction time of 30 min, 60 min, 120 min and more than 12 hours are labelled as Sn-S_30, Sn-S_60, Sn-S_120 and Sn-S_Onight respectively. Thereafter, the as-synthesized powders were characterized using various techniques.

To determine the phase, crystal structure and purity of the as-synthesized powders, XRD was carried out for Sn-S_30, Sn-S_60, Sn-S_120 and Sn-S_Onight, and the patterns obtained are presented in Figure 5.1. From this figure, it can be seen that the diffraction pattern for all four samples have sharp and distinct peaks, suggesting their good crystallinity even without any post-annealing process. The XRD pattern for Sn-S_60 (Figure 5.1) can be matched to that for hexagonal tin disulfide (SnS_2) phase with lattice parameters, a = 3.6486 Å and c = 5.8992 Å (JCPDS 023-0677), while that for Sn-S_Onight can be matched to that for orthorhombic tin monosulfide (SnS) phase with lattice parameters, a = 4.3291 Å, b = 11.1923 Å and c = 3.9838 Å (JCPDS 039-0354). No impurity peak was observed in both XRD patterns, demonstrating the good purity of the as-synthesized SnS_2 and SnS powders. It can be seen from Figure 5.1 that Sn-S_30 displayed a similar XRD pattern as that for Sn-S_60, indicating that these two samples have the same phase and that the powder obtained after reacting for 30 min contain SnS_2 (JCPDS 023-0677) particles. However, presence of diffraction peaks which can be matched to an orthorhombic Sn_2S_3 phase with lattice parameters, a = 8.864 Å, b = 14.02 Å and c = 3.747 Å (JCPDS 014-0619) is also spotted in the XRD pattern of Sn-S_30, indicating that the sample that is reacted for 30 min consists of a mixture of two tin sulfide phases – a hexagonal SnS_2 and an orthorhombic Sn_2S_3 phase. From the XRD pattern of Sn-S_120, it can be seen that the powder obtained after a 2-h reaction comprises of a mixture of particles with hexagonal SnS_2 and orthorhombic SnS (JCPDS 039-0354) phase.

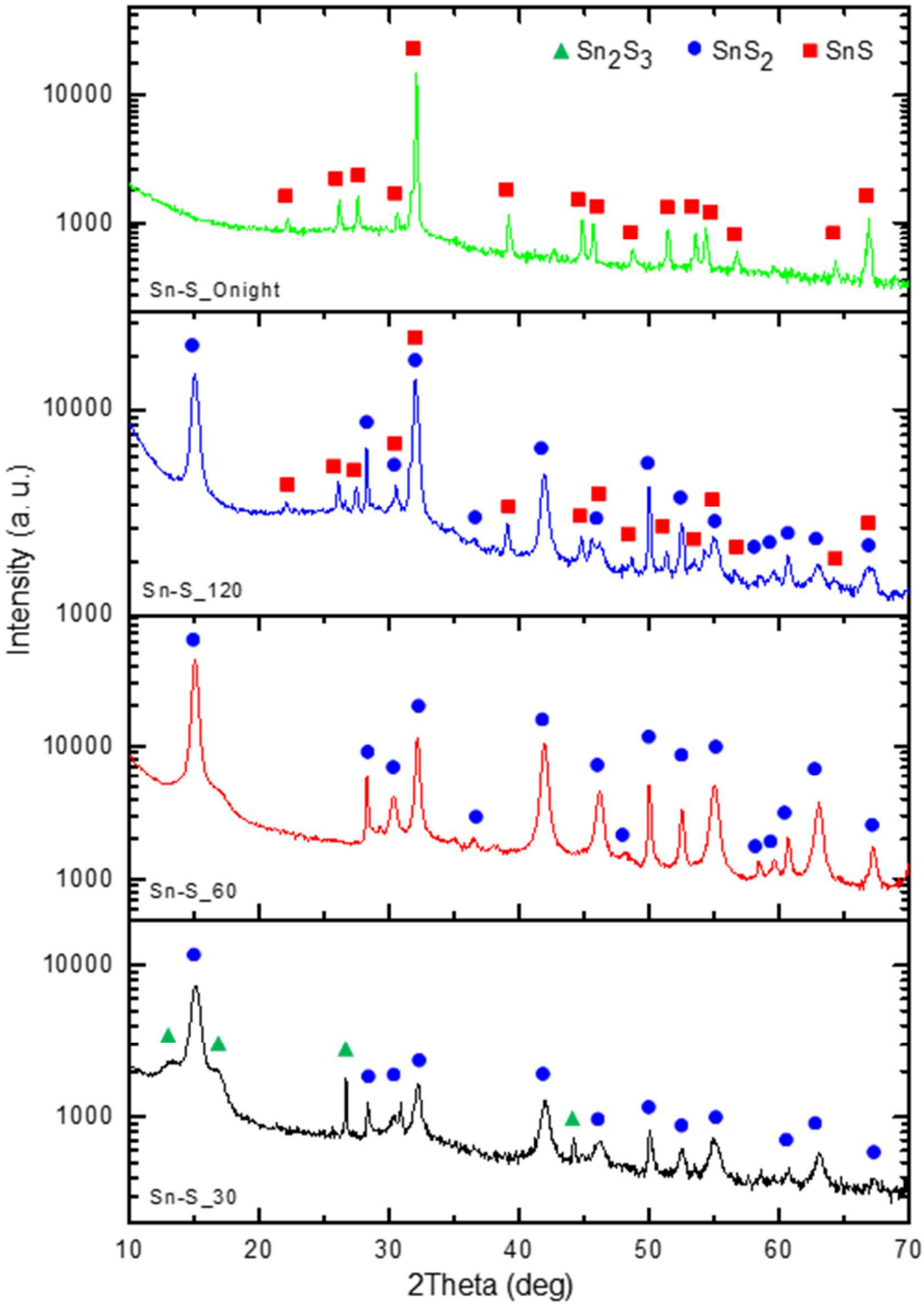

Figure 5.1: XRD patterns of Sn-S_30, Sn-S_60, Sn-S_120 and Sn-S_Onight.

FESEM was used to study the particle size and morphology of the samples and how they change when the reaction duration is varied. Figure 5.2 shows the FESEM images of the samples that have been reacted for 30 min (Sn-S_30), 60 min (Sn-S_60), 120 min (Sn-S_120) and overnight (Sn-S_Onight). From the FESEM image of Sn-S_30, it can be seen that the sample reacted for 30 min consists mainly of nanoplates with a width of around 250 nm and thickness of about 25 nm and some granular particles. Upon increasing the reaction duration to 60 min (Sn-S_60), hexagonal nanoplates that are approximately 20 nm thick and 180 – 560 nm wide were obtained. The particles formed after reacting for 120 min also comprises mostly of hexagonal nanoplates that are around 20 nm thick, but with a smaller width of about 150 – 375 nm. After reacting for more than 12 hours (Sn-S_Onight), granular particles with diameter in the range of 60 – 400 nm were obtained.

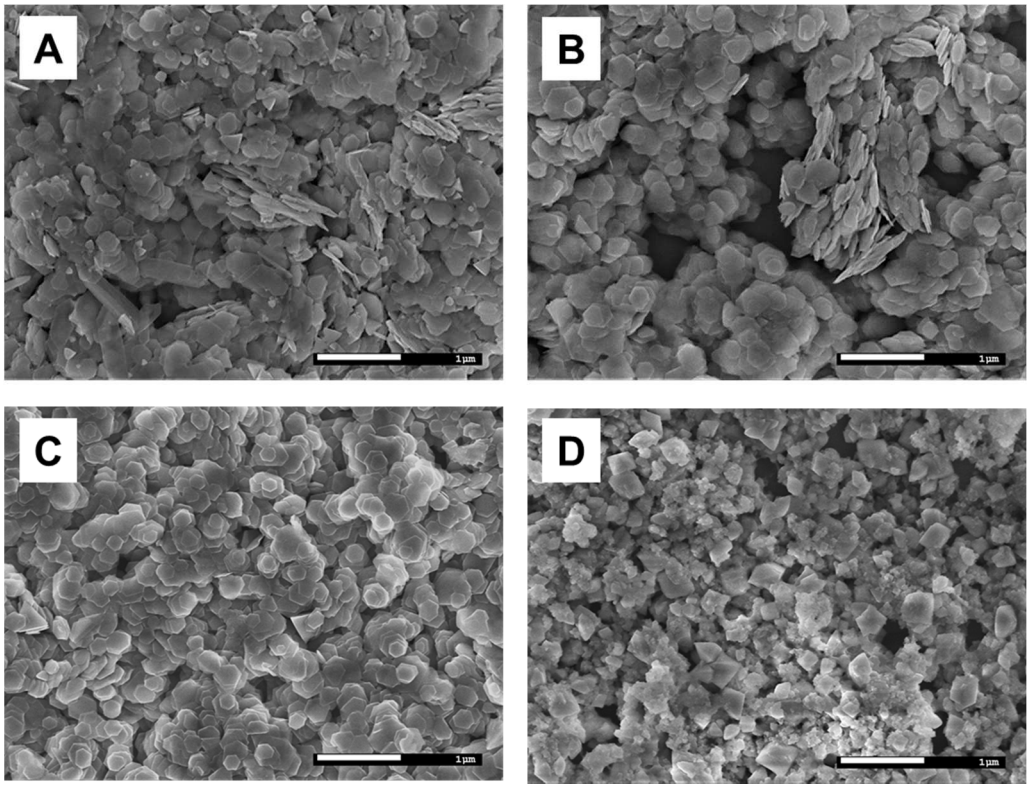

Figure 5.2: FESEM images of (A) Sn-S_30, (B) Sn-S_60, (C) Sn-S_120 and (D) Sn-S_Onight.

As explained in Section 4.2, sulfur exists as cycloocta-S (S_8) rings in its normal state and is unable to react directly with metal chlorides to form metal sulfide. [1, 2] Hence, oleylamine is being used to activate the elemental sulfur, thereby increasing its reactivity and enabling it to react with the metal ions. [3-5] In this reaction, as with the synthesis of iron sulfides in Chapter 4, oleyamine functioned as a solvent, a surfactant and, at the same time, a reducing agent. [6, 7] At low temperatures such as room temperature, sulfur exists mainly as alkylammonium polysulfides in oleylamine solution. [8, 9] Upon heating to high temperatures i.e. 240 °C, the hydrogen sulfide (H_2S), produced by the reaction of these polysulfide ions with the excess amine in the solution, can react with the Sn^{2+} ions from the $SnCl_2$ to form tin sulfides. [9]

From the XRD results in Figure 5.1, it can be seen that, after 30 min of reaction, a mixture of SnS_2 and Sn_2S_3 is obtained. Further increase of the reaction time to 60 min yields pure SnS_2 phase. This observation matches the speculation reported by Zhong et al. when he prepared SnS_2 via a hydrothermal reaction using Sn foil as the Sn precursor and cysteine ($HO_2CCH(NH_2)CH_2SH$) as the S precursor. [10] In his report, he proposed that SnS (where Sn has an oxidation state of +2), which is first formed through the reaction between Sn^{2+} and S^{2-}, undergoes further oxidation to yield Sn_2S_3 (where Sn has a mixed oxidation state of +2 and +4) and then SnS_2 (where Sn has an oxidation state of +4). Upon further reaction, the SnS_2 is found to slowly decompose to form SnS, yielding a mixture of these two phases after 2 hours of reaction. Such a decomposition of metal sulfide and sublimation of sulfur have been reported in the literatures [11, 12] and it should be highlighted that, although this reaction is carried out in inert i.e. argon environment, the reaction setup is not fully enclosed and escape of some gaseous products like sulfur can occur through the condenser, as evident in the experimental setup in Figure 3.1. After an overnight reaction, SnS with good purity is obtained.

5.2 Electrochemical Properties

A series of electrochemical characterization was carried out according to the half-cell configuration described in Section 3.3.1 to examine the lithium storage properties of

the as-synthesized SnS (Sn-S_Onight) and SnS_2 (Sn-S_60). These two samples were chosen for the study because of their good purity which allows better comparison on the effect of how the number of sulfide ion in the stoichiometry of a tin sulfide compound affects its lithium storage properties. It should be mentioned that care was taken to ensure that the two tin sulfide compounds were synthesized using the same precursors and surfactant to eliminate any possible effect due to the remaining surfactant on the as-synthesized particles. The fact that the synthesized SnS and SnS_2 particles do not have any fanciful morphologies eradicated the possible effect of particle morphology on the lithium storage performance of the two tin sulfide samples. To study the cycling performance of the as-synthesized tin sulfides, the assembled cells were cycled galvanostatically between 0.001 and 3 V (*vs.* Li/Li^+) at various current densities. Plots of the capacity of the working electrode against the cycle number for the cells cycled at a current density of 0.1 A g^{-1} and 1 A g^{-1} are depicted in Figure 5.3.

Based on the assumption that SnS, during its initial lithiation, will first undergo an irreversible conversion reaction to form Sn and Li_2S followed by a reversible alloying reaction between Sn with Li to form $Li_{4.4}Sn$, SnS is calculated to have a maximum theoretical initial capacity of 1140 mA h g^{-1} and a reversible theoretical capacity of 781 mA h g^{-1}. From Figure 5.3, it can be observed that Sn-S_Onight exhibits initial discharge capacities of 1443 mA h g^{-1} and 1165 mA h g^{-1} when cycled at a current density of 0.1 A g^{-1} and 1 A g^{-1} respectively, which are higher than its maximum theoretical initial capacity. The reason for this observation is mainly ascribed to the formation of a gel-like solid/electrolyte interphase (SEI) layer on the surface of an electrode in a lithium ion battery made with alkyl carbonate-based electrolyte, as mentioned in Section 4.3. [13] Another possible reason for this observation could be due to the intercalation reaction between SnS with lithium ions. [14, 15] It is known that SnS has a layered structure where the layers are connected to each other along the c-axis by weak van der Waal's forces. This structure, which is analogous to that of graphite, allows lithium ions to get inserted into the void spaces between the SnS layers without causing any phase decomposition, hence providing another possible lithium

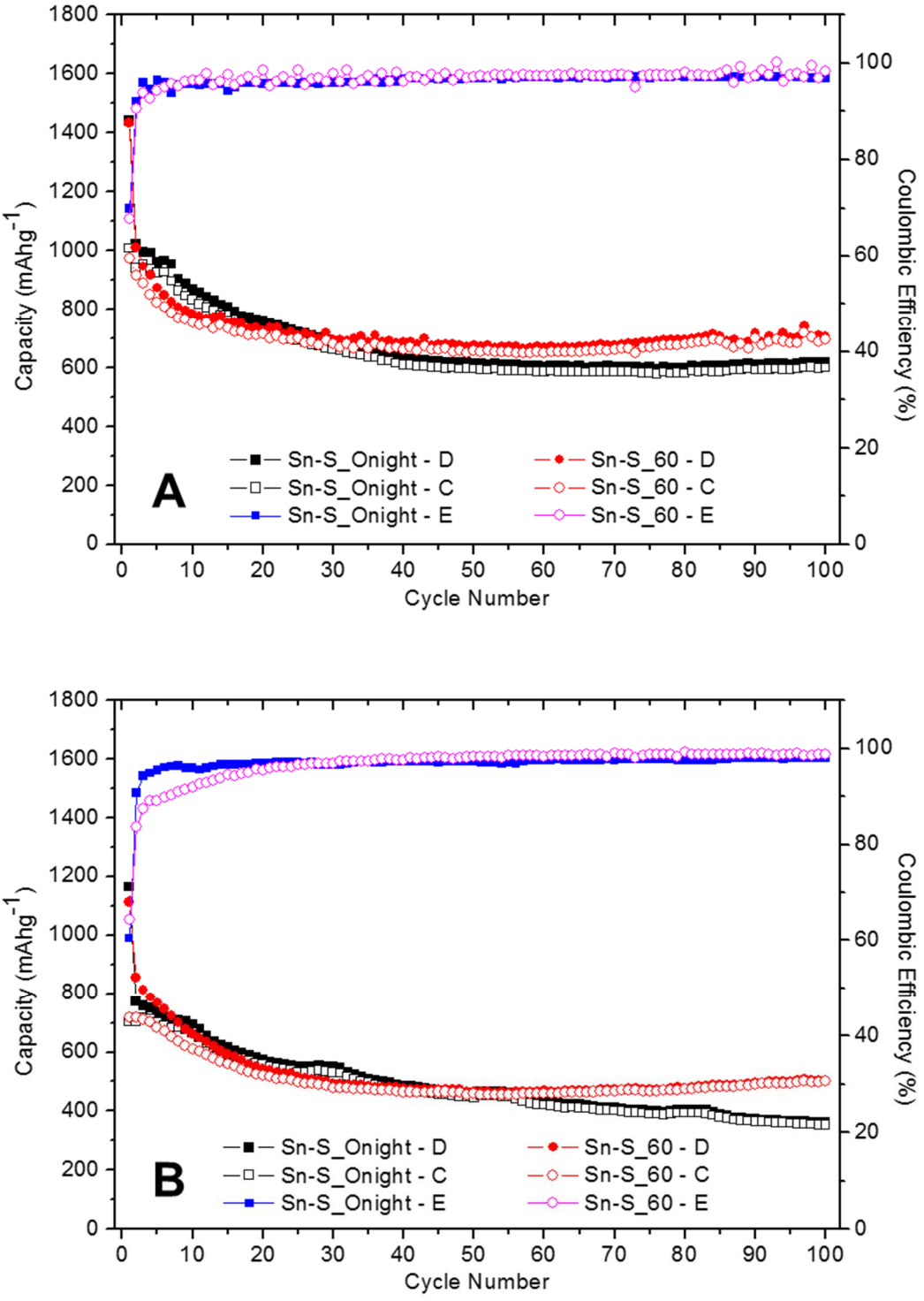

Figure 5.3: Cycling performance of the Sn-S_Onight and Sn-S_60 electrodes at a current density of (A) 0.1 A g^{-1} and (B) 1 A g^{-1} between 0.001 and 3 V (*vs.* Li/Li^+). Sn-S_Onight – D, Sn-S_Onight – C and Sn-S_Onight – E refers to the discharge and charge capacities and coulombic efficiency of Sn-S_Onight respectively, while Sn-S_60 – D, Sn-S_60 – C and Sn-S_60 – E refers to the discharge and charge capacities and coulombic efficiency of Sn-S_60 correspondingly.

storage route which was not accounted for during the calculation of the theoretical capacity of SnS. As observed from Figure 5.3, a high initial discharge capacity of 1434 mA h g^{-1}, which is also higher than the maximum theoretical initial capacity of SnS_2 (1230 mA h g^{-1}), was achieved by Sn-S_60 when cycled at a current density of 0.1 A g^{-1} due to the same reasons as for the Sn-S_Onight electrode. It should be noted that SnS_2, like SnS, also has a layered structure and, hence, has a possibility for lithium storage via intercalation reaction. When cycled at 1 A g^{-1}, Sn-S_60 delivered an initial discharge capacity of 1112 mA h g^{-1}.

From Figure 5.3A, it can be seen that, when cycled at a current density of 0.1 A g^{-1}, both Sn-S_Onight and Sn-S_60 experienced a huge drop from their initial discharge capacities of 1443 mA h g^{-1} and 1434 mA h g^{-1} to reach a discharge capacity of 1024 mA h g^{-1} and 1011 mA h g^{-1} at their second cycle respectively. Similar observation was also made for the two tin sulfide electrodes cycling at 1 A g^{-1}. This large decrease in discharge capacity from the first to the second cycle is attributed mostly to the irreversible conversion reaction between tin sulfides and lithium to form Sn and Li_2S which only took place during the first discharge cycle and not during subsequent cycling. Another reason for the much lower discharge capacity in the second cycle compared to the first would be the absence of the SEI formation reaction which typically only takes place during the first cycle.

The discharge capacity of Sn-S_Onight is observed to decrease slowly from its initial reversible discharge capacity of 1024 mA h g^{-1} (2^{nd} cycle) to 630 mA h g^{-1} at the 40^{th} cycle when cycled at a current density of 0.1 A g^{-1} (Figure 5.3A). From the 40^{th} to 100^{th} cycle, the discharge capacity of Sn-S_Onight remains fairly constant with a difference of not more than 6% between the maximum and minimum discharge capacity attained in this cycle range. At the 100^{th} cycle, Sn-S_Onight delivered a discharge capacity of 620 mA h g^{-1} when cycled at 0.1 A g^{-1} from 0.001 – 3 V, retaining about 60% of its initial reversible discharge capacity. Figure 5.3A shows that Sn-S_60 also exhibits good cycling performance, achieving an initial reversible discharge capacity of 1011 mA h g^{-1} at the 2^{nd} cycle, which gradually decreases to 728 mA h g^{-1} at the 20^{th} cycle. From the 20^{th} to 100^{th} cycle, the discharge capacities of Sn-S_60 stay quite constant with a

difference of less than 10% between the maximum and minimum discharge capacity attained in this cycle range. After subjecting to 100 galvanostatic discharging and charging cycles, Sn-S_60 retained about 70% of its initial reversible discharge capacity, delivering a discharge capacity of 708 mA h g^{-1}.

To study the cycling capability of SnS (Sn-S_Onight) and SnS_2 (Sn-S_60) at fast rates, the battery cells were subjected to galvanostatic charging and discharging at a higher current density of 1 A g^{-1} and the results are presented in Figure 5.3B. From this figure, it can be seen that Sn-S_Onight delivered an initial discharge capacity of 1165 mA h g^{-1} and a discharge capacity of 774 mA h g^{-1} at the 2^{nd} cycle, exhibiting an irreversible capacity of 391 mA h g^{-1}. The discharge capacity of this sample slowly decreases from the 2^{nd} cycle to the 100^{th} cycle. Eventually, Sn-S_Onight displayed a discharge capacity of 361 mA h g^{-1} at the 100^{th} cycle, retaining only 47% of its initial reversible discharge capacity. As shown in Figure 5.3B, Sn-S_60 also demonstrated good cycling performance, with an initial discharge capacity of 1112 mA h g^{-1} and an initial reversible discharge capacity of 856 mA h g^{-1}, corresponding to an irreversible capacity of 256 mA h g^{-1}. The discharge capacity of Sn-S_60 gradually decreases from the 2^{nd} to the 30^{th} cycle (495 mA h g^{-1}), thereafter it remains fairly constant from the 30^{th} to the 100^{th} cycle, with a difference of less than 10% between the maximum and minimum discharge capacity value achieved in this cycle range. After undergoing 100 charging-discharging cycling, Sn-S_60 delivered a discharge capacity of 506 mA h g^{-1}, keeping 60% of its initial discharge capacity.

From Figure 5.3, it can be observed that SnS_2 (Sn-S_60) and SnS (Sn-S_Onight) exhibits similar cycling performance for the first 50 cycles when cycled at a current density of 0.1 A g^{-1} and 1 A g^{-1}. After prolonged cycling i.e. > 50 cycles at low current densities, SnS_2 is found to display slightly better cycling stability than SnS. At a low current density of 0.1 A g^{-1}, SnS_2 managed to retain 70% of its initial reversible discharge capacity at the 100^{th} cycle while SnS only retained 60%. When the current density is increased, SnS_2 is found to demonstrate an even better cycling stability than SnS after prolonged cycling. At a high current density of 1 A g^{-1}, SnS_2 preserved 60% of its initial reversible discharge capacity at the 100^{th} cycle while SnS only managed to keep 47%, as shown in Figure 5.3B. It can also be observed from the plots in Figure 5.3 that SnS_2 not only retained a higher percentage of its initial reversible capacity after

100 galvanostatic charging-discharging cycles, it also delivered a higher discharge capacity of 708 mA h g^{-1} and 506 mA h g^{-1} compared to 620 mA h g^{-1} and 361 mA h g^{-1} attained by SnS when cycled at a current density of 0.1 A g^{-1} and 1 A g^{-1} correspondingly.

To make lithium ion batteries that have high power and can undergo fast charging, it is essential for the electrode to have good rate capability. Hence, the cycling performance of the two tin sulfide electrodes at numerous current densities were examined and the results are presented in Figure 5.4. From this figure, it can be seen that the SnS (Sn-S_Onight**)** electrode exhibits similar cycling performance as the SnS_2 electrode (Sn-S_60) when cycled at low current densities of 0.1 A g^{-1}, 0.2 A g^{-1} and 0.5 A g^{-1} in a voltage window of 0.001 – 3 V. Upon subjecting the two tin sulfide electrodes to cycling at higher current densities of 1 A g^{-1}, 2 A g^{-1} and 5 A g^{-1}, it became very obvious that SnS_2 has more superior lithium storage and cycling performance than SnS. This observation is in consistent with that mentioned earlier in this section. When subjected to galvanostatic cycling at a current density 0.1 A g^{-1}, 0.2 A g^{-1}, 0.5 A g^{-1}, 1 A g^{-1}, 2 A g^{-1}, and 5 A g^{-1}, the SnS electrode obtained a discharge capacity of around 851 mA h g^{-1}, 701 mA h g^{-1}, 620 mA h g^{-1}, 341 mA h g^{-1}, 148 mA h g^{-1} and 61 mA h g^{-1} respectively. SnS_2, on the other hand, demonstrated a better cycling performance than the SnS electrode, where it attained a discharge capacity of approximately 875 mA h g^{-1}, 689 mA h g^{-1}, 575 mA h g^{-1}, 491 mA h g^{-1}, 413 mA h g^{-1} and 235 mA h g^{-1} when charged and discharged at a current density 0.1 A g^{-1}, 0.2 A g^{-1}, 0.5 A g^{-1}, 1 A g^{-1}, 0.2 A g^{-1}, and 5 A g^{-1} correspondingly.

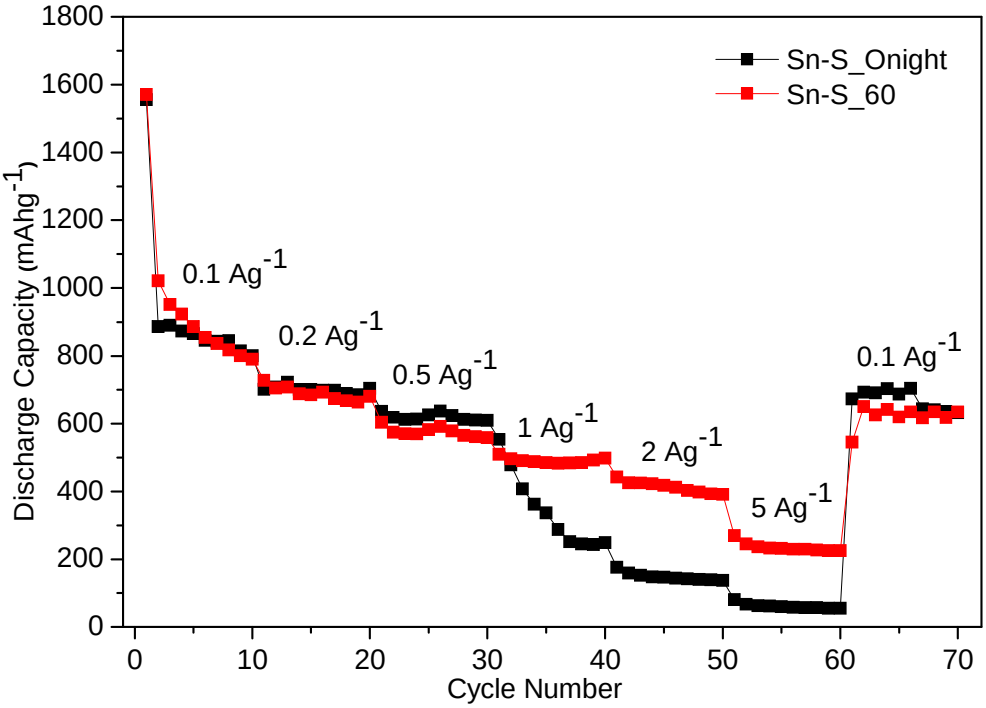

Figure 5.4: Cycling performance of the Sn-S_Onight and Sn-S_60 electrodes at various current densities between 0.001 and 3 V (vs. Li/Li^+).

To gain an insight into why SnS_2 exhibits better lithium storage performance i.e. higher capacity and superior cycling stability than SnS after prolonged cycling particularly at higher current densities, it is essential to understand the reaction between lithium ions and these two tin sulfide compounds during cycling. Hence, cyclic voltammetry (CV) of the SnS and SnS_2 electrodes (Figure 5.5) were performed under ambient temperature in a voltage window of 0.001 – 3 V (*vs.* Li/Li^+) and at a scan rate of 0.2 mV s^{-1} to comprehend the reaction between the Li^+ ions and the tin sulfide electrodes during cycling. The galvanostatic discharge (Li ion insertion) and charge (Li ion extraction) voltage profiles for both electrodes when cycled between 0.001 and 3 V (*vs.* Li/Li^+) at a low current density of 0.1 A g^{-1} and a high current density of 1 A g^{-1} are also plotted and depicted in Figure 5.6 and Figure 5.7.

Figure 5.5 shows the first five cycle CV for the SnS (Sn-S_Onight) and SnS_2 (Sn-S_60) electrode recorded under ambient temperature in the voltage range of 0.001 – 3 V (*vs.* Li/Li^+) at a constant scan rate of 0.2 mV s^{-1}. From Figure 5.5A, it can be seen that there

is only one obvious reduction peak at 0.85 V in the first cycle CV for the SnS electrode. This peak is related to the reaction between SnS and Li^+ to form Sn and Li_2S (Equation 5.1). [16] The alloying reaction between Sn and Li^+ (forward reaction in Equation 5.3) is represented by the broad reduction band from 0.67 – 0 V in the first cycle CV in Figure 5.5A. [17-19] As suggested by the higher-than-theoretical initial discharge capacity of Sn-S_Onight when cycled at 0.1 A g^{-1} and 1 A g^{-1} (Figure 5.3), SEI layer is formed during the initial discharge of the Sn-S_Onight electrode. Since the formation of this layer typically occurs at a potential of < 1.2 V, the reduction peak resulting from this reaction is deemed to be overlapped by those from the conversion and alloying of SnS with Li^+. [16, 17] Two oxidation peaks were observed in the first cycle CV for the SnS electrode where the peak at 0.67 V is ascribed to the de-alloying reaction to form Sn and Li^+ (reverse reaction in Equation 5.3), and that at 1.87 V is attributed to the formation of SnS from Sn (Equation 5.4). [19] Although the conversion reaction between tin sulfides like SnS and SnS_2 with lithium were typically assumed to be irreversible in the determination of their theoretical capacity, a close examination through the literature shows that the partial reversibility of this reaction has been observed by several research groups when the battery cells were cycled from 0 V to ≥ 2 V. In fact, an oxidation peak at around 1.9 V has been noticed by both Tao et al. and Tripathi et al. in the first cycle CV of their SnS electrode where they also attributed this peak to the partial reformation of SnS. [19, 20]

It is noteworthy to mention that the reaction between Li^+ and tin sulfides i.e. SnS or SnS_2 to form Sn and Li_2S (Equation 5.1 and Equation 5.2) have been shown to occur via several steps, resulting in multiple reduction peaks in the CV curves for some tin sulfide electrodes, like that reported by Kim et al. [14], Sathish et al. [21] and Liu and coworkers. [22] However, only one reduction peak relating to the decomposition of SnS into Sn and Li_2S is observed in the first cycle CV curve in Figure 5.5A, suggesting that these reactions could have occurred simultaneously during the first lithiation

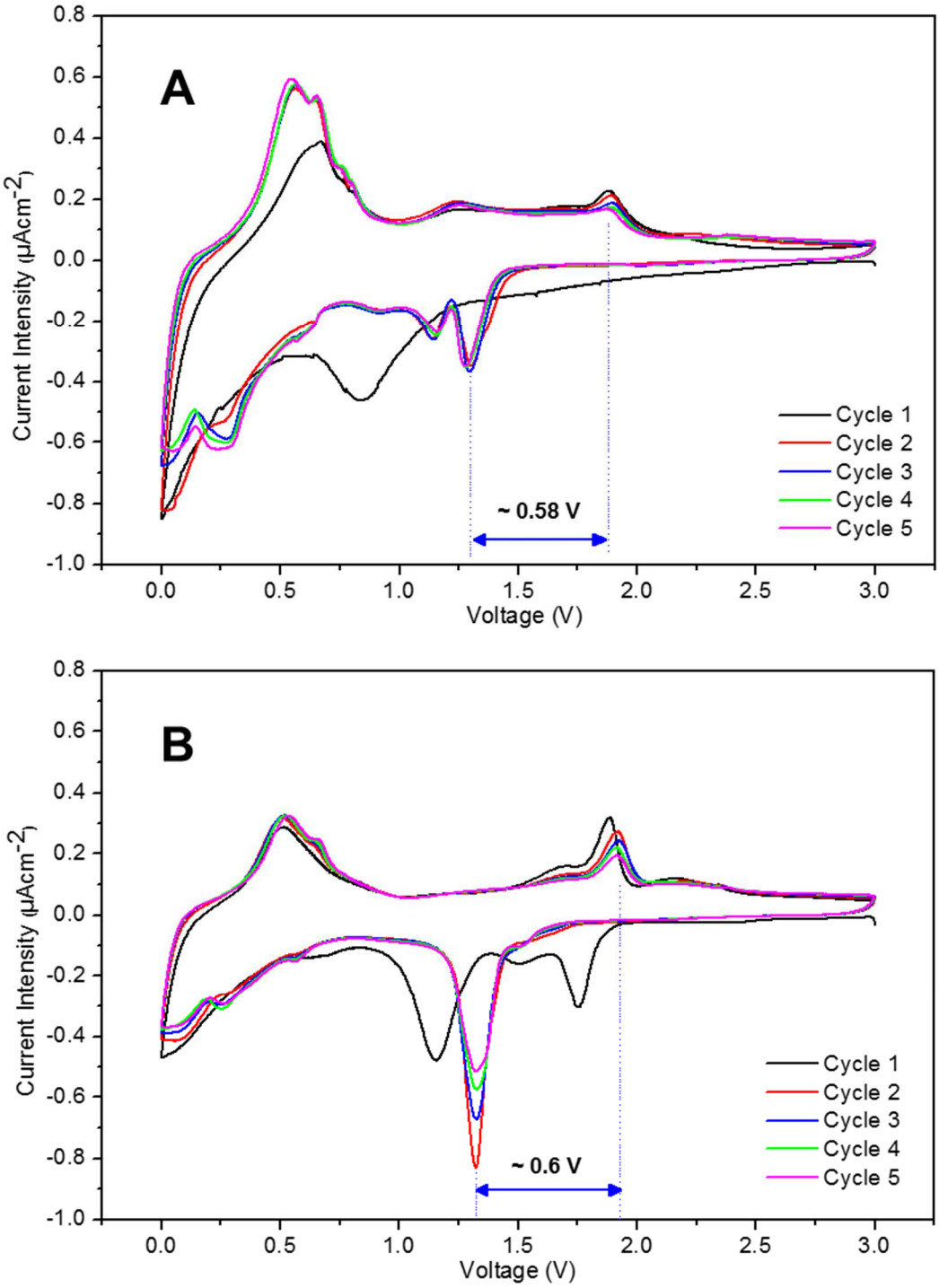

Figure 5.5: Cyclic voltammetry of (A) Sn-S_Onight and (B) Sn-S_60 electrode recorded under ambient temperature in the voltage range of 0.001 – 3 V (*vs.* Li/Li^+) at a constant scan rate of 0.2 mV s^{-1}.

process due to the slow diffusion of Li^+ into the SnS electrode at ambient temperature. Likewise, although the formation of $Li_{4.4}Sn$ from Li^+ and Sn has been found to actually take place progressively through a series of reactions where the lithiated Sn (Li_xSn) with different amounts of lithium content ($0 < x \leq 4.4$) are formed at different potential [18], only one broad reduction band relating to the alloying of Sn with Li^+ is observed in the first cycle CV in Figure 5.5A. This could also be due to the slow diffusion of Li^+ into the electrode at ambient temperature, thereby causing the formation of Li_xSn with different amounts of lithium content to occur concurrently, hence resulting in one broad reduction band in the CV of the SnS electrode instead of a series of reduction peaks.

$$SnS + 2\,Li^+ + 2\,e^- \longrightarrow Sn + Li_2S$$

Equation 5.1

$$SnS_2 + 4\,Li^+ + 4\,e^- \longrightarrow Sn + 2\,Li_2S$$

Equation 5.2

$$Sn + x\,Li^+ + x\,e^- \longleftrightarrow Li_xSn \qquad (0 < x \leq 4.4)$$

Equation 5.3

The single reduction peak (0.85 V) that denotes the reaction in Equation 5.1 in the first cycle CV for the SnS electrode is split into two peaks (1.31 V and 1.14 V) in the second cycle (Figure 5.5A), suggesting a faster diffusion of Li^+ into the electrode which allows the series of reactions leading to the decomposition of SnS to take place via a stepwise manner. In the voltage range of 0.75 – 0 V, a number of humps and peaks (0.65 V, 0.27 V and ≈ 0 V) relating to the formation of Li_xSn from Sn and Li^+ (forward reaction in

Equation 5.3) are observed in the second cycle reduction scan for the SnS electrode. The de-alloying process of Li_xSn (reverse reaction in Equation 5.3) is represented by numerous peaks (0.56 V, 0.65 V, 0.75 V, 0.81 V and 1.23 V), showing its discrete nature. [19] The oxidation peak at 1.89 V in the second cycle CV of the SnS electrode, like the peak at 1.87 V in the first cycle, is also attributed to the formation of SnS from Sn (Equation 5.4). The CV curves for the subsequent cycles are similar to that for the second cycle, indicating that the SnS undergo similar electrode reactions from the second lithiation-delithiation cycle onwards.

$$Sn + Li_2S \longrightarrow SnS + 2\,Li^+ + 2\,e^-$$

Equation 5.4

$$Sn + 2\,Li_2S \longrightarrow SnS_2 + 4\,Li^+ + 4\,e^-$$

Equation 5.5

When the Sn-S_60 electrode undergoes its first lithiation, reduction peaks corresponding to the decomposition of SnS_2 into Sn and Li_2S can be spotted at 1.75 V, 1.51 V and 1.15 V (Figure 5.5B). From the discussion two paragraphs ago, this reaction (Equation 5.2) have been reported in the literature to occur via several steps which, according to Kim et al., involves the following reactions: (1) $SnS_2 + y\ Li^+ + y\ e^- \rightarrow Li_ySnS_2$, (2) $Li_ySnS_2 + (x\text{-}y)\ Li^+ + (x\text{-}y)\ e^- \rightarrow Li_xSnS_2$, and (3) $Li_xSnS_2 + (4\text{-}x)\ Li^+ + (4\text{-}x)\ e^- \rightarrow Sn + 2\ Li_2S$ where $0 < y < x \leq 2$. [14] It should be highlighted again that both SnS and SnS_2 has a layered structure and, hence, can allow partial intercalation of Li^+ into and out of the void spaces between the SnS or SnS_2 layers, forming Li_xSnS_2 ($0 < x \leq 2$) without resulting in any phase decomposition. The alloying reaction between Sn and Li^+ (forward reaction in Equation 5.3) is represented by the broad reduction band from 0.8 – 0 V in the first cycle CV in Figure 5.5B. [23, 24] As discussed previously,

SEI layer is formed during the initial discharge of the Sn-S_60 electrodes when cycled at 0.1 A g^{-1} and, like for the SnS electrode, the reduction peak resulting from this reaction is deemed to be overlapped by those from the conversion and alloying of SnS_2 with Li^+. [17, 25] Similar to the SnS electrode, two oxidation peaks were observed in the first cycle CV for the SnS_2 electrode where the peak at 0.51 V is attributed to the de-alloying of Li_xSn (reverse reaction in Equation 5.3), and that at 1.89 V is related to the reaction between Sn and Li_2S (Equation 5.5). [15, 19, 26, 27]

In the second cycle CV for the SnS_2 electrode (Figure 5.5B), the three reduction peaks corresponding to the electrode reaction in Equation 5.2 is depicted as one peak centred at 1.32 V, suggesting that these discrete reactions could have taken place simultaneously during the second lithiation. In the voltage range of 0.8 – 0 V, a number of bumps (0.58 V, 0.28 V and ≈ 0.1 V) relating to the formation of lithiated Sn (Li_xSn) (forward reaction in Equation 5.3) are observed in the second cycle reduction scan for the SnS_2 electrode. In the second cycle oxidation scan, the delithiation of Li_xSn is represented by two peaks that are centred at 0.52 V and 0.66 V, instead of only one peak in the first cycle. The oxidation peak at 1.92 V in the second cycle CV of the SnS_2 electrode is attributed to the formation of SnS_2 from Sn (Equation 5.5). It can be seen from Figure 5.5B that the CV curves for the third, fourth and fifth cycles are similar to that for the second cycle, indicating that the SnS_2 undergo similar electrode reactions from the second lithiation-delithiation cycle onwards.

From the CV curves for both SnS and SnS_2 electrodes (Figure 5.5), it can be seen that the peak at around 1.9 V in the oxidation scan and those in the range of 1.1 – 1.32 V in the reduction scan exists for all the five cycles, showing that the conversion reaction for both tin sulfide electrodes is reversible when cycled from 0.001 – 3 V. However, the reversibility of this conversion reaction is observed to decrease with increasing cycle numbers as indicated by the drop the peak intensities for the oxidation peak at about 1.9 V and the reduction peaks in the range of 1.1 – 1.32 V as cycling proceeds. It is also noted that, although both tin sulfides undergo similar electrode reactions during lithiation and delithiation, more peaks are observed in the CV curves for the SnS electrode than the SnS_2 electrode from the second to the fifth cycle. This suggests that the SnS electrode could have better conductivity and, hence, faster lithium diffusion into it, enabling the series of electrode reactions to take place via a stepwise manner. In

fact, the polarization in the SnS electrode, as determined by the voltage difference between the oxidation and reduction peaks corresponding to the conversion reaction, is found to be slightly lower than that for the SnS_2 electrode, further suggesting a better electron and Li^+ transport at the active material/electrolyte interface for the SnS electrode. It should also be mentioned that SnS is known to have a higher intrinsic electrical conductivity (193 – 8.3 mS cm^{-1}) than SnS_2. [22, 28]

The galvanostatic charge/discharge voltage profiles for both tin sulfide electrodes when cycled at a current density of 0.1 A g^{-1} and 1 A g^{-1} between 0.001 and 3 V (*vs.* Li/Li^+) are plotted and presented in Figure 5.6 and Figure 5.7 respectively. From Figure 5.6A, it can be seen that, when cycled at 0.1 A g^{-1} in the voltage window of 0.001 – 3 V, there is only one plateau (1.21V) in the first cycle galvanostatic discharge curve for SnS which is associated to the reaction between SnS and Li^+ as stated in Equation 5.1. [19] According to the first cycle CV for the SnS electrode in Figure 5.5A, the gentle slope from about 0.7 – 0 V in the first cycle discharge profile for the SnS electrode can be associated to the alloying reaction between Sn and Li^+ (Equation 5.3). In its first cycle, SnS attained a discharge capacity of 1443 mA h g^{-1}, a charge capacity of 1008 mA h g^{-1} and, therefore, a coulombic efficiency of 69.9% when cycled at 0.1 A g^{-1}. This low coulombic efficiency is largely attributed to the "lost" of lithium ions for future lithiation and delithiation process due to the irreversible formation of the SEI layer. In the second cycle, the SnS electrode exhibited a discharge capacity of 1024 mA h g^{-1}, a charge capacity of 941 mA h g^{-1} and a high coulombic efficiency of 92.0%. From the second to the 100^{th} cycle, the SnS electrode achieved an average coulombic efficiency of about 96.5% when cycled at a current density of 0.1 A g^{-1} (Figure 5.3A).

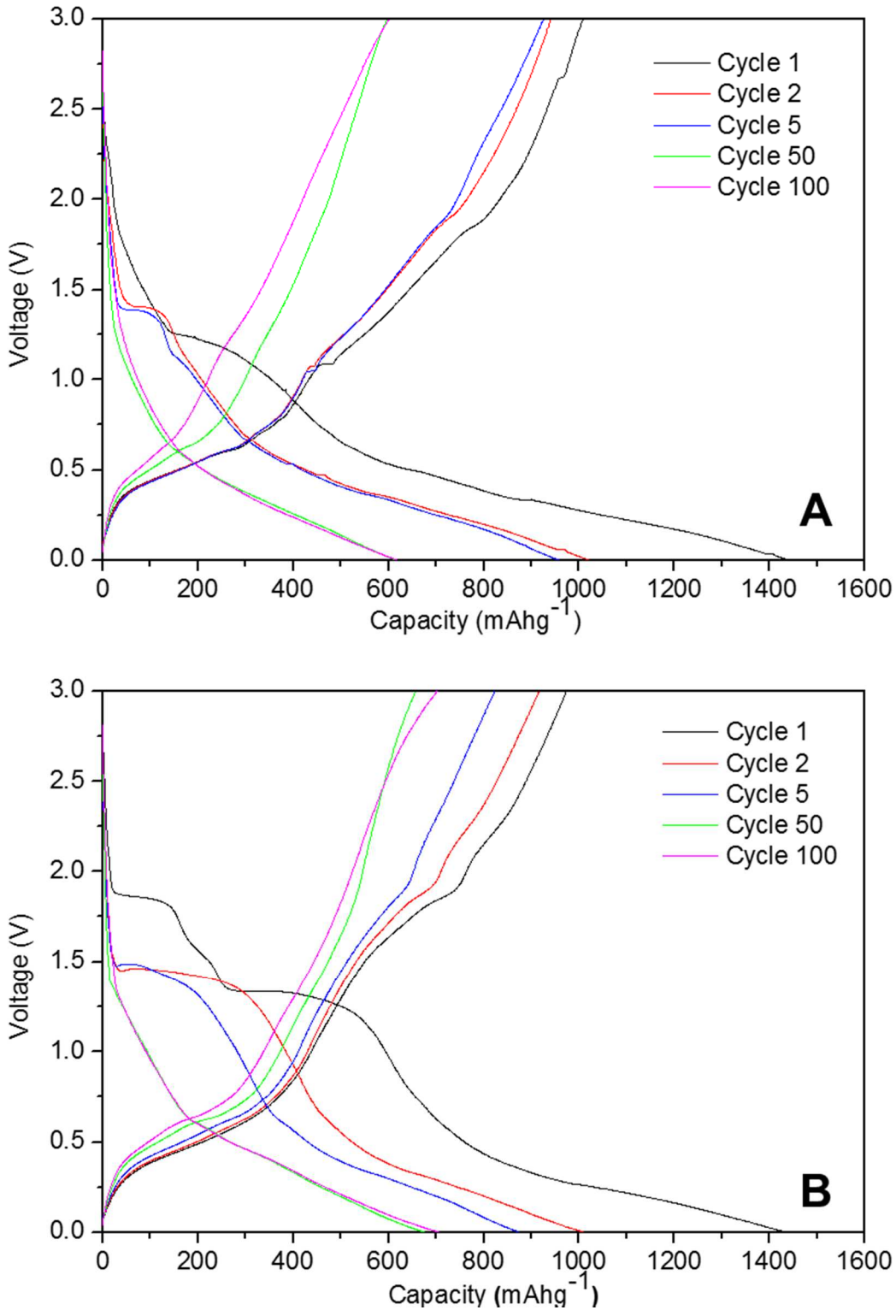

Figure 5.6: Galvanostatic charge/discharge voltage profiles of the (A) Sn-S_Onight and (B) Sn-S_60 electrodes when cycled at a current density of 0.1 A g^{-1} between 0.001 and 3 V (*vs.* Li/Li^{+}).

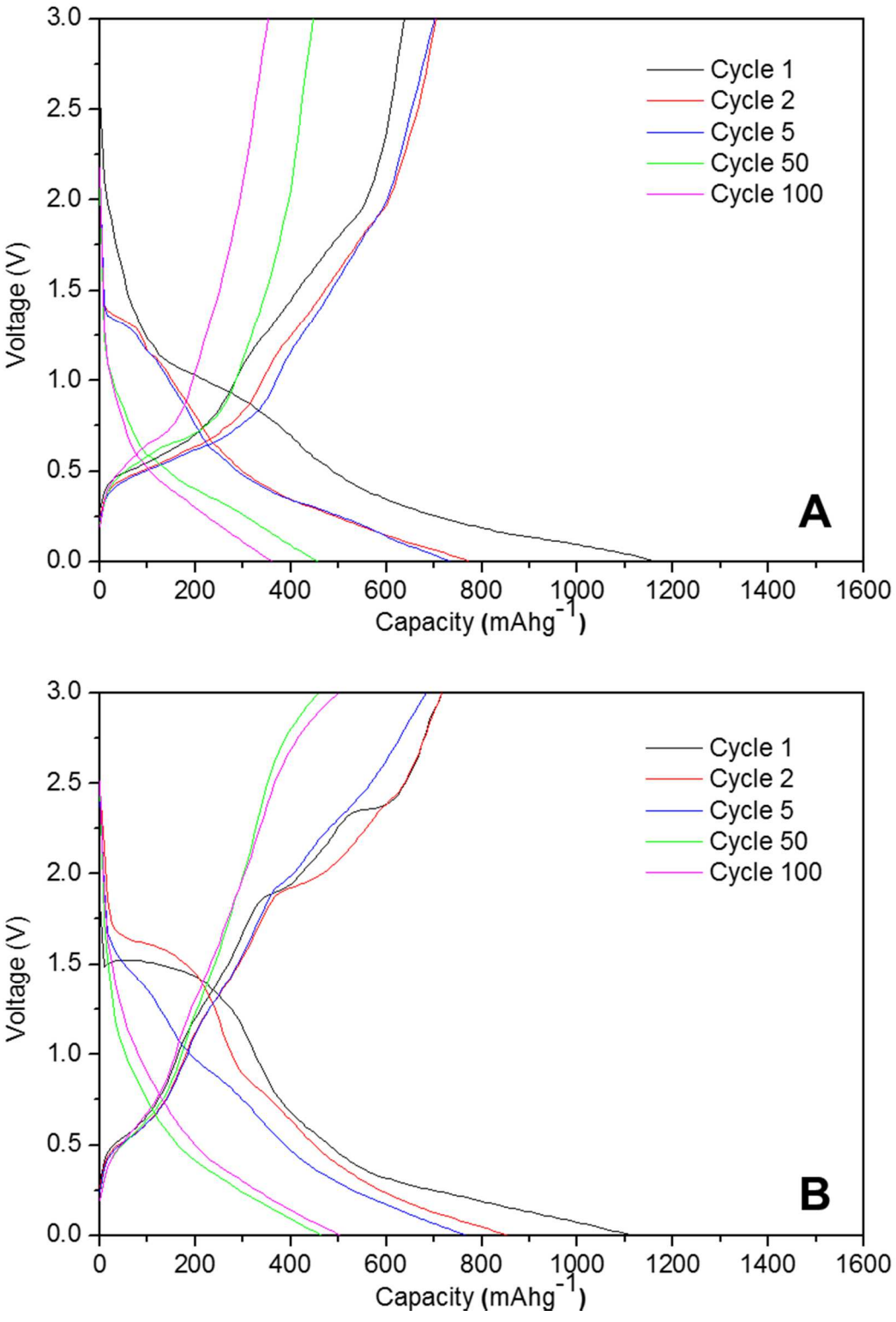

Figure 5.7 Galvanostatic charge/discharge voltage profiles of the (A) Sn-S_Onight and (B) Sn-S_60 electrodes when cycled at a current density of 1 A g^{-1} between 0.001 and 3 V (*vs.* Li/Li^+).

Analysis of the discharge profile for the SnS_2 electrode (Figure 5.6B) shows the presence of two obvious plateaus (≈ 1.86 V and ≈ 1.33 V) in its first cycle, which are associated to the decomposition of SnS_2 into Sn and Li_2S (Equation 5.2). Similar to the SnS electrode, a gentle slope from about 0.7 – 0 V is observed in the first cycle discharge profile for the SnS_2 electrode which can be related to the formation of Li_xSn from Sn and Li^+ (Equation 5.3). From Figure 5.6, it can be seen that the voltage profiles for the two tin sulfide electrodes have similar shape from the second cycle onwards, suggesting that these two electrodes undergo similar electrode reactions from the second to the 100th cycle which is in consistent with the CV results. In its first cycle when cycled at 0.1 A g^{-1}, SnS_2 attained a discharge capacity of 1434 mA h g^{-1}, a charge capacity of 973 mA h g^{-1} and, hence, a coulombic efficiency of 67.8%. As with the SnS electrode, this low initial coulombic efficiency of 67.8% is a result of the irreversible formation of an SEI layer. At the second cycle, the SnS_2 electrode exhibited a discharge capacity of 1011 mA h g^{-1}, a charge capacity of 916 mA h g^{-1} and a high coulombic efficiency of 90.6 %. From the second to the 100th cycle, the SnS_2 electrode achieved an average coulombic efficiency of about 97.0% when cycled at a current density of 0.1 A g^{-1} (Figure 5.3A).

When the current density is increased to 1 A g^{-1}, it can be seen that the shape of the voltage profiles for the SnS and SnS_2 electrodes (Figure 5.7) are somewhat analogous to their respective voltage profiles when cycled at 0.1 A g^{-1} (Figure 5.6) except for the first cycle galvanostatic charge profile for the SnS_2 electrode. During its initial charge at 1 A g^{-1}, a short plateau, which could be related to the formation of polysulfides from Li_2S, is observed at around 2.4 V for the SnS_2 electrode. [29-31] It should be mentioned that this oxidation reaction (at ≈ 2.4 V) is only observed in the first cycle galvanostatic charge profile for the SnS_2 electrode when cycled at a current density of 1 A g^{-1} and are not present in the other voltage profiles (Figure 5.6 and Figure 5.7) and CV (Figure 5.5) for the tin sulfide electrodes. From Figure 5.7A, it can be seen that, when cycled at 1 A g^{-1}, the SnS electrode exhibited a discharge capacity of 1165 mA h g^{-1}, a charge capacity of 704 mA h g^{-1} and a coulombic efficiency of 60.4 %. At the second cycle, the SnS electrode displayed a discharge capacity of 774 mA h g^{-1}, a charge capacity of 703 mA h g^{-1} and a high coulombic efficiency of 90.8%. From the second to the 100th cycle, the SnS electrode achieved an average coulombic efficiency of about 97.1%

when cycled at a current density of 1 A g^{-1} (Figure 5.3B). For the SnS_2 electrode, an initial discharge capacity of 1112 mA h g^{-1}, charge capacity of 717 mA h g^{-1} and coulombic efficiency of 64.4% are attained when cycled at a current density of 1 A g^{-1}. A discharge capacity of 856 mA h g^{-1}, charge capacity of 717 mA h g^{-1} and coulombic efficiency of 83.7% are achieved in its second cycle. On the average, a coulombic efficiency of 97.0% is attained by the SnS_2 electrode from the second to 100th cycle (Figure 5.3B).

From the CV curves in Figure 5.5, it can be observed that the electrode reaction for both tin sulfides can be generally divided into two sections: (1) the decomposition of SnS_y (y = 1 or 2) into Sn and Li_2S and (2) the alloying of Sn with Li^+ to form Li_xSn where the former reaction takes place at a voltage of $\geq$ 0.8 V and the latter at a voltage of < 0.8 V. Hence, the discharge capacity attained by these two tin sulfide electrodes can, in broad, also be divided into two main portions with the discharge capacity obtained in the voltage range of 3 – 0.8 V attributed to the intercalation and conversion reaction, and that in a voltage range of 0.8 – 0 V accredited to the alloying reaction. A summary of the discharge capacity obtained by the two tin sulfide electrodes in the second, 5th, 50th and 100th cycle due to the two main reactions are tabulated and presented in Table 5.1. It should be mentioned that the initial discharge capacity for both tin sulfide electrodes were not tabulated in this table because of the occurrence of SEI formation during their first lithiation, as indicated by their low initial coulombic efficiency of < 70 %, which will contribute to additional discharge capacity in the voltage range of < 1.2 V and provide inaccurate distribution of discharge capacity to the two main reactions. It is assumed that from the second cycle onwards, all the discharge capacities attained are due to either the reversible intercalation and conversion reaction or the reversible alloying reaction since both electrodes displayed high coulombic efficiencies from the second to the 100th cycle, indicating the negligible presence of irreversible reaction during these cycles.

Table 5.1: Tabulation of discharge capacities contributed by different reactions for the SnS (Sn-S_Onight) and SnS_2 (Sn-S_60) electrodes at various cycles and current densities.

Current Density	Cycle Number	Discharge Capacity (mA h g^{-1}) for SnS Electrode Due to			Discharge Capacity (mA h g^{-1}) for SnS_2 Electrode Due to		
		Intercalation + Conversion (3 - 0.8 V)	Alloying (> 0.8 - 0 V)	Total (3 - 0 V)	Intercalation + Conversion (3 - 0.8 V)	Alloying (> 0.8 - 0 V)	Total (3 - 0 V)
0.1 A g^{-1}	2	264	760	1024	424	587	1011
	5	254	706	960	322	552	874
	50	99	517	616	133	546	679
	100	111	510	620	135	572	707
1 A g^{-1}	2	208	566	774	342	514	856
	5	192	543	734	283	484	768
	50	58	401	459	92	374	466
	100	50	311	361	117	381	498

As shown in Table 5.1, most of the discharge capacity attained by both electrodes are due to the alloying reaction between Sn and Li^+, especially as the cycling proceeds. When cycled at 0.1 A g^{-1}, the alloying reaction contributed to 74.2%, 73.6%, 83.9% and 82.2% of the total discharge capacity delivered by the SnS electrode at the 2nd, 5th, 50th and 100th cycle respectively. For the SnS_2 electrode cycled at 0.1 A g^{-1}, 58.0%, 63.1%, 80.4% and 80.9% of the total discharge capacity achieved at the 2nd, 5th, 50th and 100th cycle was attributed to the storage of lithium ions via alloying reaction. From Table 5.1, it can also be seen that, the combination of intercalation and conversion reaction yielded a discharge capacity of 208 mA h g^{-1} and 50 mA h g^{-1} at the second and 100th cycle respectively for the SnS electrode cycled at 1 A g^{-1}. A discharge capacity of 566 mA h g^{-1} and 311 mA h g^{-1} were obtained by the alloying reaction at the second and 100th cycle correspondingly when the SnS electrode was cycled at 1 A g^{-1}. Similar decrease in the capacity attained by the alloying reaction and a combination of intercalation and conversion reaction can be observed in both electrodes as the cycling proceeds via a current density of 0.1 A g^{-1} and 1 A g^{-1}. This matches the observation from Figure 5.5 where the peak intensities for the oxidation peak at about

1.9 V and the reduction peaks in the range of 1.1 – 1.32 V decreased as cycling proceeds, indicating a decline in the reversibility of the conversion reaction for the two electrodes. It can also be seen that, for both tin sulfide electrodes, the discharge capacity achieved by the combination of both intercalation and conversion reaction decreases at a faster rate than that by the alloying reaction, showing the better reversibility of the alloying reaction as the electrodes are cycled from the second to 100th cycle. In fact, taking a look at the SnS electrode cycled at 1 A g^{-1}, it can be seen that, at the 100th cycle, a discharge capacity of 50 mA h g^{-1} and 311 mA h g^{-1} were contributed by the combination of intercalation and conversion reaction and by the alloying reaction respectively, which corresponds to 24.0% and 54.9% of the discharge capacities of these reactions delivered at the second cycle.

From Table 5.1, it can be observed that the discharge capacity attained by intercalation and conversion reaction is higher for the SnS_2 electrode compared to the SnS electrode. During the second cycle at a current density of 1 A g^{-1}, the intercalation and conversion reaction yielded a discharge capacity of 342 mA h g^{-1} for the SnS_2 electrode, but only achieved a discharge capacity of 208 mA h g^{-1} for the SnS electrode. This is in consistent with the calculation made based on the reaction stated in Equation 5.1 and Equation 5.2, where SnS is determined to have the capability of achieving a theoretical capacity of 355 mA h g^{-1} while SnS_2 can attained a higher theoretical capacity of 585 mA h g^{-1} via conversion reaction. As predicted by the lower theoretical alloying reaction (Equation 5.3) capacity of SnS_2 (645 mA h g^{-1}) compared to SnS (781 mA h g^{-1}), SnS_2 is observed to obtain a lower discharge capacity via alloying reaction initially (581 mA h g^{-1} at the second cycle at a current density of 0.1 A g^{-1}) compared to the SnS electrode (760 mA h g^{-1} at the second cycle at a current density of 0.1 A g^{-1}). However, as cycling proceeds, it can be seen from Table 5.1 that the alloying discharge capacity achieved by the SnS_2 electrode fades at a much slower rate than the SnS electrode. When cycled at 0.1 A g^{-1}, the SnS_2 electrode retained 97.5% of its second cycle alloying discharge capacity of 587 mA h g^{-1} at the 100th cycle, while the SnS electrode only kept 67.0% (of 760 mA h g^{-1}). At a higher current density of 1 A g^{-1}, the SnS_2 electrode still retained a 74.2% of its second cycle alloying discharge capacity (514 mA h g^{-1}) compared to the 54.9% retained by the SnS electrode (566 mA h g^{-1}). Eventually, the SnS_2 electrode (572 mA h g^{-1} at 0.1 A g^{-1} and 381 mA h g^{-1} at 1 A g^{-1}) exhibits a higher

alloying discharge capacity than the SnS electrode (510 mA h g^{-1} at 0.1 A g^{-1} and 311 mA h g^{-1} at 1 A g^{-1}) at the 100th cycle.

As observed from the galvanostatic cycling of the tin sulfide electrodes (Figure 5.3 and Figure 5.4), SnS_2 displayed a higher capacity and better cycling stability than SnS after prolonged cycling particularly at higher current densities. It can be seen from the CV curves (Figure 5.5) that both tin sulfide electrodes undergo similar electrode reactions during the lithiation and delithiation process. Nitrogen adsorption/desorption measurement shows that the two tin sulfide samples have similar surface area, where the SnS sample have a Brunauer−Emmett−Teller (BET) surface area of 10.0 m^2 g^{-1} and the SnS_2 sample have a BET surface area of 13.0 m^2 g^{-1} (Figure A.2). In fact, the presence of more redox peaks in the CV curves for the SnS electrode (relating to the same conversion and alloying reaction as that for the SnS_2 electrode), together with its slightly lower polarization, suggests that SnS has a better electron and Li^+ transport at the active material/electrolyte interface than SnS_2. Therefore, the superior lithium storage performance of the SnS_2 electrode is likely a result from its chemical and structural properties and should not be due to its electronic and ionic conductivity.

From Table 5.1, it was found that the discharge capacity attained by the intercalation and conversion reaction is higher for the SnS_2 electrode compared to the SnS electrode and, although a lower alloying discharge capacity was initially observed in the SnS_2 electrode, it was found that this capacity will eventually be higher than that attained by the SnS electrode as cycling proceeds due to a slower alloying capacity fading rate in the SnS_2 electrode. Hence, the higher discharge capacity displayed by SnS_2 after prolonged cycling can be attributed to its higher capacity attained by both the alloying reaction and a combination of the intercalation and conversion reaction. It has been proposed in many literatures that the Li_2S formed from the reaction between the tin sulfides and lithium ions can act as a matrix to buffer the large volume change during the lithiation and delithiation of Sn, thus reducing the pulverization of the electrode. [15, 32-36] As evidenced by the higher discharge capacity attained from the intercalation and conversion reaction throughout the 100 cycles, more Li_2S is formed during the lithiation of SnS_2, thus providing a thicker layer to buffer the large volume change during the lithiation and delithiation of Sn. This can result in a reduction in the pulverization and better capacity retention of the electrode after prolonged cycling, as

verified by the slower alloying capacity fading rate observed in the SnS_2 electrode compared to the SnS electrode.

5.3 Conclusion

In summary, SnS and SnS_2 with good purity have been successfully synthesized via a solution-based chemical synthesis method. Pure samples of these two tin sulfides were obtained by simply varying reaction time. From the experiments, it was found that Sn_2S_3 (where Sn has a mixed oxidation state of +2 and +4), which is first formed through the reaction between Sn^{2+} and S^{2-}, undergoes further oxidation to yield SnS_2 (where Sn has an oxidation state of +4). Upon further reaction, the SnS_2 is found to slowly decompose to form SnS, yielding a mixture of these two phases after 2 hours of reaction and pure SnS phase after an overnight reaction.

The electrochemical properties of the as-synthesized SnS and SnS_2 were characterized and it was found that SnS_2 displayed a higher capacity and better cycling stability than SnS after prolonged cycling particularly at higher current densities. When cycled at a current density of 0.1 A g^{-1}, SnS exhibited an initial discharge capacity of 1443 mA h g^{-1} and a discharge capacity of 1024 mA h g^{-1} and 620 mA h g^{-1} at the 2^{nd} and 100^{th} cycle. When the current density is increased to 1 A g^{-1}, a discharge capacity of 1165 mA h g^{-1}, 774 mA h g^{-1} and 361 mA h g^{-1} was attained at the first, second and 100^{th} cycle correspondingly. For the SnS_2 electrode, an initial discharge capacity of 1434 mA h g^{-1} and discharge capacities of 1011 mA h g^{-1} (2^{nd} cycle) and 708 mA h g^{-1} (100^{th} cycle) were delivered when cycled at a current density of 0.1 A g^{-1}. When cycled at 1 A g^{-1}, SnS_2 achieved an initial discharge capacity of 1112 mA h g^{-1} and discharge capacities of 856 mA h g^{-1} and 506 mA h g^{-1} at the second and 100^{th} cycle respectively.

Since the SnS_2 electrode has poorer electronic and ionic conductivity than the SnS electrode, its superior lithium storage performance is attributed to its chemical and structural properties. As evidenced by the higher discharge capacity attained from the intercalation and conversion reaction throughout the 100 cycles, more Li_2S is formed during the lithiation of SnS_2, thus providing a thicker layer to buffer the large volume

change during the lithiation and delithiation of Sn. This can result in a reduction in the pulverization and better capacity retention of the electrode after prolonged cycling, as verified by the slower alloying capacity fading rate observed in the SnS_2 electrode compared to the SnS electrode.

This is a first attempt to study the effect of how the number of sulfide ion in the stoichiometry of a tin sulfide compound (a conversion and alloying-typed compound) i.e. Sn:S = 1:1 (SnS) or 1:2 (SnS_2) affects its lithium storage properties. It should be highlighted that care was taken to ensure that the two tin sulfide compounds were synthesized using the same precursors and surfactant to eliminate any possible effect due to the remaining surfactant on the as-synthesized particles. The fact that the synthesized SnS and SnS_2 particles do not have any fanciful morphologies eradicated the possible effect of particle morphology on the lithium storage performance of the two tin sulfide samples and made this a fairer comparison since the morphology and surface area of the tin sulfide particles have great impact on its lithium storage performance, as mentioned in Section 2.4.2.

References:

1. Pauling, L., *On the stability of the S(8) molecule and the structure of fibrous sulfur.* Proceedings of the National Academy of Sciences of the United States of America, 1949. **35**(9): p. 495.
2. Zumdahl, S.S., *Chemical principles*. 6th ed. 2009, Boston, Mass. : Abingdon : Houghton Mifflin.
3. Bartlett, P.D., Cox, E.F., and Davis, R.E., *Reactions of elemental sulfur. IV. Catalytic effects in the reaction of sulfur with triphenylphosphine.* Journal of the American Chemical Society, 1961. **83**(1): p. 103.
4. Cotton, F.A. and Wilkinson, G., *The Group VI elements: S, Se, Te, Po*, in *Advanced inorganic chemistry : a comprehensive text*. 1972, Interscience Publishers. p. 421-457.
5. Li, Z., Ji, Y.J., Xie, R.G., Grisham, S.Y., and Peng, X.G., *Correlation of CdS nanocrystal formation with elemental sulfur activation and its implication in*

synthetic development. Journal of the American Chemical Society, 2011. **133**(43): p. 17248.

6. Kwon, S.G. and Hyeon, T., *Colloidal chemical synthesis and formation kinetics of uniformly sized nanocrystals of metals, oxides, and chalcogenides.* Accounts of Chemical Research, 2008. **41**(12): p. 1696.
7. Mourdikoudis, S. and Liz-Marzan, L.M., *Oleylamine in nanoparticle synthesis.* Chemistry of Materials, 2013. **25**(9): p. 1465.
8. Davis, R.E. and Nakshbendi, H.F., *Sulfur in amine solvents.* Journal of the American Chemical Society, 1962. **84**(11): p. 2085.
9. Thomson, J.W., Nagashima, K., Macdonald, P.M., and Ozin, G.A., *From sulfur-amine solutions to metal sulfide nanocrystals: peering into the oleylamine-sulfur black box.* Journal of the American Chemical Society, 2011. **133**(13): p. 5036.
10. Zhong, H., Yang, G., Song, H., Liao, Q., Cui, H., Shen, P., and Wang, C.X., *Vertically aligned graphene-like SnS2 ultrathin nanosheet arrays: excellent energy storage, catalysis, photoconduction, and field-emitting performances.* The Journal of Physical Chemistry C, 2012. **116**(16): p. 9319.
11. Ji, L., Xin, H.L., Kuykendall, T.R., Wu, S.L., Zheng, H., Rao, M., Cairns, E.J., Battaglia, V., and Zhang, Y., *SnS2 nanoparticle loaded graphene nanocomposites for superior energy storage.* Physical Chemistry Chemical Physics, 2012. **14**(19): p. 6981.
12. Wang, Y., Wu, J., Tang, Y., Lü, X., Yang, C., Qin, M., Huang, F., Li, X., and Zhang, X., *Phase-controlled synthesis of cobalt sulfides for lithium ion batteries.* ACS Applied Materials & Interfaces, 2012. **4**(8): p. 4246.
13. Laruelle, S., Grugeon, S., Poizot, P., Dolle, M., Dupont, L., and Tarascon, J.M., *On the origin of the extra electrochemical capacity displayed by MO/Li cells at low potential.* Journal of the Electrochemical Society, 2002. **149**(5): p. A627.
14. Kim, T.J., Kim, C., Son, D., Choi, M., and Park, B., *Novel SnS2-nanosheet anodes for lithium-ion batteries.* Journal of Power Sources, 2007. **167**(2): p. 529.
15. Bhaskar, A., Deepa, M., and Rao, T.N., *Tin disulfide nanoflowers versus nanosheets as anodes in lithium-ion batteries: how the nanostructure controls performance.* Electrochimica Acta, 2015. **184**: p. 239.
16. Tripathi, A.M. and Mitra, S., *Tin sulfide (SnS) nanorods: structural, optical and lithium storage property study.* RSC Advances, 2014. **4**(20): p. 10358.

17. Liu, S., Yin, X., Chen, L., Li, Q., and Wang, T., *Synthesis of self-assembled 3D flowerlike SnS2 nanostructures with enhanced lithium ion storage property.* Solid State Sciences, 2010. **12**(5): p. 712.
18. Zhang, W.J., *Lithium insertion/extraction mechanism in alloy anodes for lithium-ion batteries.* Journal of Power Sources, 2011. **196**: p. 877
19. Tao, H.C., Yang, X.L., Zhang, L.L., and Ni, S.B., *One-step in situ synthesis of SnS/graphene nanocomposite with enhanced electrochemical performance for lithium ion batteries.* Journal of Electroanalytical Chemistry, 2014. **728**: p. 134.
20. Tripathi, A.M. and Mitra, S., *The influence of electrode structure on the performance of an SnS anode in Li-ion batteries: effect of the electrode particle, conductive support shape and additive.* RSC Advances, 2015. **5**(30): p. 23671.
21. Sathish, M., Mitani, S., Tomai, T., and Honma, I., *Ultrathin SnS2 nanoparticles on graphene nanosheets: synthesis, characterization, and Li-ion storage* The Journal of Physical Chemistry C, 2012. **116**(23): p. 12475.
22. Liu, J., Gu, M., Ouyang, L., Wang, H., Yang, L., and Zhu, M., *Sandwich-like SnS/polypyrrole ultrathin nanosheets as high-performance anode materials for Li-ion batteries.* ACS Applied Materials & Interfaces, 2016. **8**(13): p. 8502.
23. Li, J., Wu, P., Lou, F., Zhang, P., Tang, Y., Zhou, Y., and Lu, T., *Mesoporous carbon anchored with SnS2 nanosheets as an advanced anode for lithium-ion batteries.* Electrochimica Acta, 2013. **111**: p. 862.
24. Zhuo, L., Wu, Y., Wang, L., Yu, Y., Zhang, X., and Zhao, F., *One-step hydrothermal synthesis of SnS2/graphene composites as anode material for highly efficient rechargeable lithium ion batteries.* RSC Advances, 2012. **2**(12): p. 5084.
25. Wu, Q., Jiao, L., Du, J., Yang, J., Guo, L., Liu, Y., Wang, Y., and Yuan, H., *One-pot synthesis of three-dimensional SnS2 hierarchitectures as anode material for lithium-ion batteries.* Journal of Power Sources, 2013. **239**: p. 89.
26. Brousse, T., Lee, S.M., Pasquereau, L., Defives, D., and Schleich, D.M., *Composite negative electrodes for lithium ion cells.* Solid State Ionics, 1998. **113–115**: p. 51.
27. Zai, J., Qian, X., Wang, K., Yu, C., Tao, L., Xiao, Y., and Chen, J., *3D-hierarchical SnS2 micro/nano-structures: controlled synthesis, formation mechanism and lithium ion storage performances.* CrystEngComm, 2012. **14**(4): p. 1364.

28. Nassary, M.M., *Temperature dependence of the electrical conductivity, Hall effect and thermoelectric power of SnS single crystals.* Journal of Alloys and Compounds, 2005. **398**(1–2): p. 21.

29. Wang, J., Yang, J., Wan, C., Du, K., Xie, J., and Xu, N., *Sulfur composite cathode materials for rechargeable lithium batteries.* Advanced Functional Materials, 2003. **13**(6): p. 487.

30. Ji, L., Rao, M., Zheng, H., Zhang, L., Li, Y., Duan, W., Guo, J., Cairns, E.J., and Zhang, Y., *Graphene oxide as a sulfur immobilizer in high performance lithium/sulfur cells.* Journal of the American Chemical Society, 2011. **133**(46): p. 18522.

31. Zhang, M., Lei, D., Yu, X., Chen, L., Li, Q., Wang, Y., Wang, T., and Cao, G., *Graphene oxide oxidizes stannous ions to synthesize tin sulfide-graphene nanocomposites with small crystal size for high performance lithium ion batteries.* Journal of Materials Chemistry, 2012. **22**(43): p. 23091.

32. Mukaibo, H., Yoshizawa, A., Momma, T., and Osaka, T., *Particle size and performance of SnS2 anodes for rechargeable lithium batteries.* Journal of Power Sources, 2003. **119-121**: p. 60.

33. Li, Y., Tu, J.P., Huang, X.H., Wu, H.M., and Yuan, Y.F., *Nanoscale SnS with and without carbon-coatings as an anode material for lithium ion batteries.* Electrochimica Acta, 2006. **52**(3): p. 1383.

34. Kim, H.S., Chung, Y.H., Kang, S.H., and Sung, Y.E., *Electrochemical behavior of carbon-coated SnS2 for use as the anode in lithium-ion batteries.* Electrochimica Acta, 2009. **54**(13): p. 3606.

35. Lee, Y., Bae, S.R., Park, B.J., Shin, D.W., Chung, W.J., and Kang, Y.M., *Sn-based chalcogenide composite as a high-capacity anode material for lithium rechargeable batteries.* Journal of the American Ceramic Society, 2012. **95**(7): p. 2272.

36. Kang, J.G., Park, J.G., and Kim, D.W., *Superior rate capabilities of SnS nanosheet electrodes for Li ion batteries.* Electrochemistry Communications, 2010. **12**(2): p. 307.

Chapter 6

Conclusion and Recommendation for Future Work

This chapter summarizes the main findings of this dissertation and highlighted the conclusions obtained. It is found in this dissertation that for both iron and tin sulfides, despite storing lithium ions via slightly different mechanisms, the compound with a higher sulfide ion content in its stoichiometry i.e. FeS_2 and SnS_2 exhibits better lithium storage performance than its counterpart with lower sulfide ion content i.e. $Fe_{1-x}S$ and SnS when prepared in a half-cell configuration and cycled in a voltage window of 0.001 – 3 V. For the pyrite FeS_2 electrode, which undergoes intercalation and conversion reaction during cycling, the superior lithium storage performance is attributed to its better conductivity and reversibility of the lithiation and delithiation of FeS_y. On the other hand, the SnS_2 electrode, which undergoes conversion and alloying reaction during cycling, displayed a better lithium storage performance due to its ability to form a thicker Li_2S layer which provides better buffering for the large volume change in the Sn particles during their alloying reaction, thus maintaining structural integrity of the electrode and result in slower capacity fading. Based on these findings and conclusions, possible future work has been recommended.

6.1 Conclusion

In view of the poor capacity retention and cycling performance resulting from the dissolution of polysulfides into the organic electrolyte, more study needs to be carried out to find approaches that can be undertaken to improve the lithium storage performance of metal sulfide electrodes. Therefore, this thesis aims to gain an insight into how the amount of sulfide ion in the stoichiometry of a metal sulfide compound affects its lithium storage properties, with the focus placed on two metal sulfide systems, namely, iron sulfides (intercalation-conversion anodic material) and tin sulfides (conversion-alloying anodic material).

To investigate the effect of how the amount of sulfide ion in the stoichiometry of an iron sulfide compound affects its lithium storage properties, pyrrhotite $Fe_{1-x}S$ and pyrite FeS_2 with good purity have been successfully synthesized via a solution-based chemical synthesis method. Pure samples of these two iron sulfides were obtained simply by varying the mole ratio between the anhydrous $FeCl_2$ and elemental S that were used as the starting materials in the synthesis. From the experiments, it was found that iron sulfides such as $Fe_{1-x}S$, FeS, Fe_3S_4, FeS_2 or a mixture of them will be formed under sulfur-limiting conditions i.e an Fe:S precursor molar ratio of 1:1 or 1:2. Pure pyrite FeS_2 phase can only be formed when excess S is present in the reaction mixture i.e. an Fe:S precursor molar ratio of 1:4 or 1:6. A possible reaction pathway for the formation of the pyrrhotite $Fe_{1-x}S$ and pyrite FeS_2 from $FeCl_2$ and elemental S precursors was proposed.

The electrochemical properties of the as-synthesized pyrrhotite $Fe_{1-x}S$ and pyrite FeS_2 were characterized and it was found that pyrite FeS_2 exhibits better lithium storage capability than pyrrhotite $Fe_{1-x}S$. For the first 50 cycles, pyrite FeS_2 achieved a discharge capacity of at least 773 mA h g^{-1}, 722 mA h g^{-1}, 712 mA h g^{-1} and 339 mA h g^{-1} when cycled at a current density of 0.1 A g^{-1}, 0.5 A g^{-1}, 1 A g^{-1} and 5 A g^{-1} respectively. On the other hand, pyrrhotite $Fe_{1-x}S$ attained a lower minimum discharge capacity of 627 mA h g^{-1}, 636 mA h g^{-1}, 598 mA h g^{-1} and 210 mA h g^{-1} for the first 50 cycles when cycled at a current density of 0.1 A g^{-1}, 0.5 A g^{-1}, 1 A g^{-1} and 5 A g^{-1} correspondingly. The superior lithium storage performance of pyrite FeS_2 compared to

pyrrhotite $Fe_{1-x}S$ can be attributed to: (1) the lower polarization, better electron and Li^+ ion transport at the interface between the active material and electrolyte at the pyrite FeS_2 electrode than the pyrrhotite $Fe_{1-x}S$ electrode and (2) the reversible lithiation and delithiation of iron sulfide (FeS_y) during the galvanostatic cycling of the pyrite FeS_2 electrode.

SnS and SnS_2 with good purity have been successfully synthesized via a solution-based chemical synthesis method to investigate the effect of how the amount of sulfide ion in the stoichiometry of a tin sulfide compound affects its lithium storage properties. Pure samples of these two tin sulfides were obtained by simply varying reaction time. From the experiments, it was found that Sn_2S_3 (where Sn has a mixed oxidation state of +2 and +4), which is first formed through the reaction between Sn^{2+} and S^{2-}, undergoes further oxidation to yield SnS_2 (where Sn has an oxidation state of +4). Upon further reaction, the SnS_2 is found to slowly decompose to form SnS, yielding a mixture of these two phases after 2 hours of reaction and pure SnS phase after an overnight reaction.

The electrochemical properties of the as-synthesized SnS and SnS_2 were characterized and it was found that SnS_2 displayed a higher capacity and better cycling stability than SnS after prolonged cycling particularly at higher current densities. When cycled at a current density of 0.1 A g^{-1}, SnS exhibited an initial discharge capacity of 1443 mA h g^{-1} and a discharge capacity of 1024 mA h g^{-1} and 620 mA h g^{-1} at the 2^{nd} and 100^{th} cycle. When the current density is increased to 1 A g^{-1}, a discharge capacity of 1165 mA h g^{-1}, 774 mA h g^{-1} and 361 mA h g^{-1} was attained at the first, second and 100^{th} cycle correspondingly. For the SnS_2 electrode, an initial discharge capacity of 1434 mA h g^{-1} and discharge capacities of 1011 mA h g^{-1} (2^{nd} cycle) and 708 mA h g^{-1} (100^{th} cycle) were delivered when cycled at a current density of 0.1 A g^{-1}. When cycled at 1 A g^{-1}, SnS_2 achieved an initial discharge capacity of 1112 mA h g^{-1} and discharge capacities of 856 mA h g^{-1} and 506 mA h g^{-1} at the second and 100^{th} cycle respectively.

Since the SnS_2 electrode has poorer electronic and ionic conductivity than the SnS electrode, its superior lithium storage performance is attributed to its chemical and structural properties. As evidenced by the higher discharge capacity attained from the intercalation and conversion reaction throughout the 100 cycles, more Li_2S is formed during the lithiation of SnS_2, thus providing a thicker layer to buffer the large volume

change during the lithiation and delithiation of Sn. This can result in a reduction in the pulverization and better capacity retention of the electrode after prolonged cycling, as verified by the slower alloying capacity fading rate observed in the SnS_2 electrode compared to the SnS electrode.

It is found in this dissertation that for both iron sulfides (intercalation-conversion anodic material) and tin sulfides (conversion-alloying anodic material), the compound with a higher sulfide ion content in its stoichiometry i.e. FeS_2 and SnS_2 exhibits better lithium storage performance than its counterpart with lower sulfide ion content i.e. $Fe_{1-x}S$ and SnS when cycled in a voltage window of 0.001 – 3 V. For the pyrite FeS_2 electrode, which undergoes intercalation and conversion reaction during charge-discharge cycling, the superior lithium storage performance is attributed to its better conductivity and reversibility of the lithiation and delithiation of FeS_y. On the other hand, the SnS_2 electrode, which undergoes conversion and alloying reaction during charge-discharge cycling, displayed a better lithium storage performance due to its ability to form a thicker Li_2S layer which provides better buffering for the large volume change in the Sn particles during their alloying reaction with lithium ions, thus maintaining structural integrity of the electrode and result in slower capacity fading.

6.2 Recommendations for Future Work

6.2.1 Evaluation of Lithium Storage Performance in Full Cell Configuration

The electrochemical properties of the as-synthesized iron and tin sulfides reported in Chapter 4 and Chapter 5 were evaluated based on a half-cell configuration. It should be pointed out that, in such configuration, lithium foil is used as the counter electrode. In other words, lithium is added in huge excess compared to the metal sulfide active materials and, hence, during the cycling of these cells, the supply of lithium ions is assumed to be unlimited. As a result of this infinite supply of lithium ion in a battery half-cell, the occurrence of irreversible electrode reactions such as the formation of the solid/electrolyte interphase (SEI) layer, which will reduce the amount of lithium ions

available for other electrode reaction in the cell, does not have much adverse effects on the lithium storage performance of the electrodes under evaluation.

However, in a commercial lithium ion battery, the supply of lithium ions is limited and will depend on the amount of lithiated compounds i.e. $LiCoO_2$ used at the counter electrode. Due to this finite supply of lithium ions in a full battery cell, the presence or absence of irreversible electrode reactions will have great impact on the overall capacity and cycling stability of the battery cells. From the galvanostatic cycling of the iron sulfide and tin sulfide electrodes (Figure 4.5, Figure 4.6 and Figure 5.3), it can be seen that a layer of SEI is formed in almost all their initial discharge. Therefore, it is anticipated that the lithium storage performance will be different in a battery with full-cell configuration compared to that with a half-cell configuration. Since commercial lithium ion battery employs a full-cell configuration and the study of these metal sulfide materials are for potential application as anode materials in commercial lithium ion battery, there is a need to investigate the lithium storage performance of the iron and tin sulfides in a battery with full-cell configuration.

6.2.2 Study on Other Binary Metal Sulfide Systems

This thesis focuses on the study of two metal sulfide systems: (1) iron sulfide ($Fe_{1-x}S$ and FeS_2) and tin sulfide (SnS and SnS_2), where the former system will undergo an intercalation followed by conversion reaction and the latter will undergo a conversion followed by alloying reaction with lithium ions. Through the analysis of their electrochemical properties, it was found that for both iron and tin sulfides, the compound with a higher sulfide ion content in its stoichiometry i.e. FeS_2 and SnS_2 exhibits better lithium storage performance than its counterpart with lower sulfide ion content i.e. $Fe_{1-x}S$ and SnS when cycled in a voltage window of 0.001 – 3 V. However, this superior lithium storage performance of FeS_2 and SnS_2 were attributed to different reasons due to their different lithium storage mechanism. For the pyrite FeS_2 electrode, which undergoes intercalation and conversion reaction during charge-discharge cycling, the superior lithium storage performance is attributed to the reversibility of the lithiation and delithiation of FeS_y. On the other hand, the SnS_2 electrode, which

undergoes conversion and alloying reaction during charge-discharge cycling, displayed a better lithium storage performance due to its ability to form a thicker Li_2S layer which provides better buffering for the large volume change in the Sn particles during their alloying reaction with lithium ions.

To obtain a more general trend on the effect of the number of sulfide ions in the stoichiometry of a metal sulfide compound on its lithium storage properties, it will be necessary to investigate the electrochemical properties of other metal sulfide systems. Hence, it is proposed to extend the study to metal sulfide systems like cobalt sulfides and copper sulfides which are analogous to the iron sulfide (intercalation-conversion) system, and also to germanium sulfides which is analogous to the tin sulfide (conversion-alloying) system. This will enable researchers to gain more understanding on the effect of sulfide content on the lithium storage properties of metal sulfide electrode and the science behind these differences. In recent years, a lot of research effort has also been placed on sodium ion batteries. There have been literatures reporting on the sodium storage properties of metal sulfides and it will also be interesting to study on the effect of the number of sulfide ions in the stoichiometry of a metal sulfide compound on its sodium storage properties.

6.2.3 Study on Structural Changes During Cycling

It is found in this dissertation that, for tin sulfides (conversion-alloying anodic material), SnS_2 exhibits better lithium storage performance than SnS when cycled in a voltage window of 0.001 – 3 V. This is attributed to its ability to form more Li_2S during lithiation which provides better buffering for the large volume change in the Sn particles during their alloying reaction with lithium ions, thus maintaining structural integrity of the electrode and result in slower capacity fading. As Li_2S is highly hydroscopic and unstable in air, it will be very difficult to observe the structural changes of the electrode during lithiation and delithiation via ex-situ techniques. Henceforth, it is suggested to carry out in-situ studies i.e. in-situ SEM and/or TEM to observe how the structure of the materials and electrode changes during lithiation and delithiation.

APPENDIX

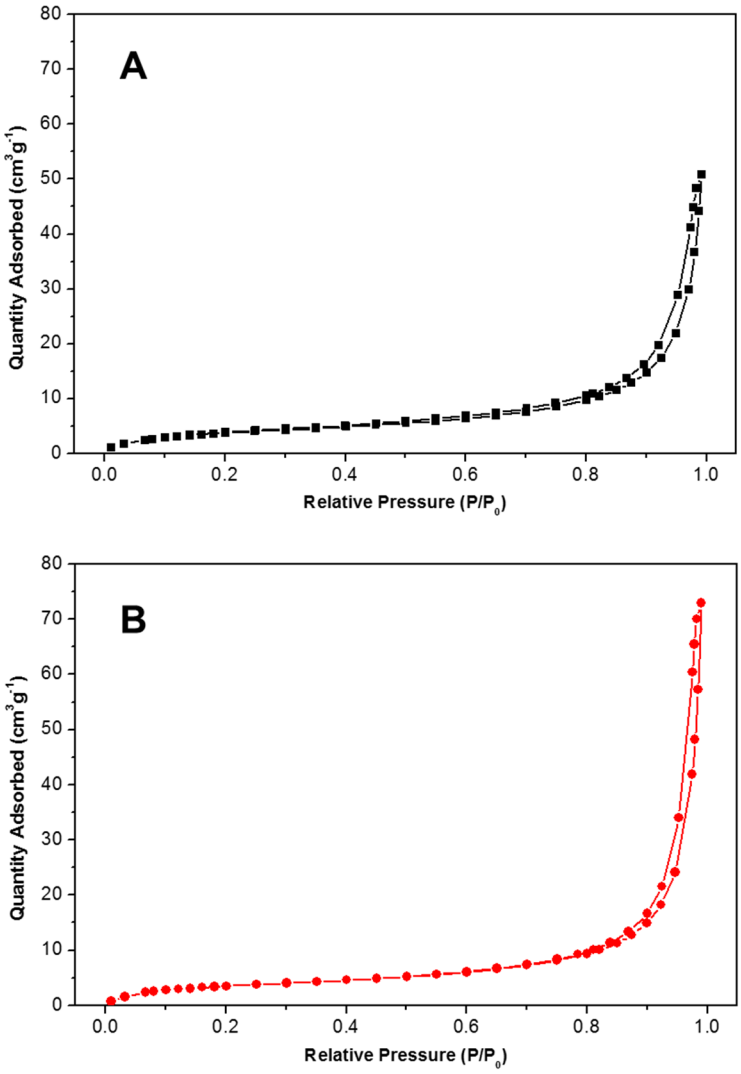

Figure A.1: Nitrogen adsorption/desorption isotherm for (A) Fe-S_1 and (B) Fe-S_6.

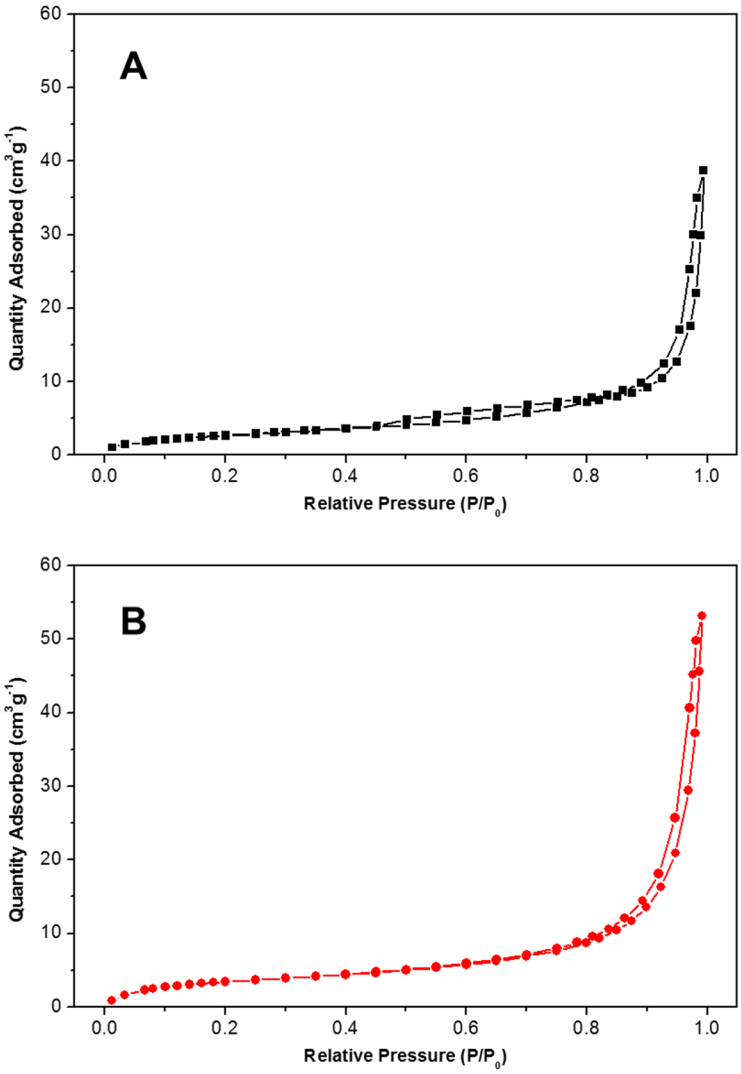

Figure A.2: Nitrogen adsorption/desorption isotherm for (A) Sn-S_Onight and (B) Sn-S_60.